PRODUCTION OF MUON PAIRS AND TAU PAIRS AT ENERGIES ABOVE THE Z^0 MASS USING THE OPAL DETECTOR AT LEP

Scott David Talbot

Thesis submitted for the degree of
Doctor of Philosophy

School of Physics and Astronomy
Faculty of Science
University of Birmingham

September 1998

Synopsis

The production cross-sections, angular distributions and asymmetries of the processes $e^+e^- \to \mu^+\mu^-$ and $e^+e^- \to \tau^+\tau^-$ at energies between 130 and 189 GeV have been measured with data taken between 1995 and 1998 using the OPAL detector at LEP.

For each process two selections have been made. The first selection consists of only the full energy events. The second also includes events in which an initial-state photon has been emitted, thus reducing the collision energy. Monte Carlo data have been used to optimise the selection efficiency and backgrounds for these two processes. The measurements have been compared with similar results from other experiments and the Standard Model.

Additionally, the measurements using the full energy events have been used, together with other OPAL measurements at the same energies, to measure the running of the electromagnetic coupling constant.

Events from both processes which have undergone initial-state radiation and have a collision energy in the region of the Z^0 resonance peak have been fitted to a Breit-Wigner function. The results of this fit are compared to the precisely known shape of the Z^0 resonance and thus the LEP beam energy has been determined.

Contribution

The work presented in this thesis was carried out within the OPAL collaboration. This collaboration consists of several hundred physicists and technicians. The large number of people needed to maintain the experiment and analyse the data mean it is often difficult to distinguish an individuals work. In this section I wish to highlight my contribution to OPAL during the last three years.

The Birmingham University OPAL group is responsible for the maintenance and smooth running of the Muon Endcap subdetector, which it built in conjunction with the Rutherford Appleton Laboratory. While resident at CERN for almost two years I acted as the Birmingham representative for the subdetector. This involved general maintenance, daily monitoring checks of the gas and high voltage systems, attending twice weekly OPAL status meetings and responding to any problems with the subdetector at any time of the day or night.

During the first three months of my PhD I started working on the measurement of the τ pair production cross-section for the 130-136 GeV data, this work was performed in collaboration with the LEP2 Standard Model working group. My contribution was to determine the selection used to identify the τ pair events and measuring the production cross-section. The rest of my first year involved re-optimising the selection for the data taken at 161 GeV and, in addition, measuring the asymmetry of the process. At the beginning of my second year I re-optimised the selection for the 172 GeV data and started working on the measurement of the production cross-section and asymmetry of the μ pair events.

In conjunction with others I began studying the effect on the measurements due to the interference between initial- and final-state radiation, and refined the μ and τ

analyses to give further improvements. When these studies were complete, the new analyses were applied to all the 130 to 172 GeV data.

For the 184 GeV data the analyses were studied once again and further improvements made. These are the analyses presented in this thesis and has been applied to all the LEP2 data sets.

During my third year I also began looking into the LEP beam energy measurement and modified the analysis of the running of α_{em} to include other measurements.

Acknowledgements

I'd like to thank everyone who helped make this thesis a reality. For all his help over the years I would like to thank my supervisor Peter Watkins. Thanks to Michael Kobel and Pat Ward for putting up with all my mistakes; Julie Kirk, as it'd have been a lot harder having to do this from scratch; John Wilson, Dave Charlton and Nigel Watson for various bits of help.

Thanks also go to everyone at CERN who made life in Geneva enjoyable. In particular to: Simon, for that day on the number 9 bus when he made the mistake of talking to me; Matt, for dragging me up various mountains (walking, snowboarding, and rock-climbing) as well as showing me what a PhD could have been like; Helen, for brilliantly organising so many skiing trips, even though I did get really cold one day sitting in the snow waiting for you to catch up; Chris, for making me grateful that I had the 'flu on the way back from Prague; Jon, for taking me to certain Geneva squat bars which I didn't really want to know but will never forget; Kate, Elspeth, Nick, Jon, Paul, Alun, Shaun, Andy, Dave, Dave, Dave and the rest.

Of course, most thanks go to my family.

Scott, September 1998

Contents

List of Figures

List of Tables

Chapter 1

The Standard Model

Today we believe that the universe is made of indivisible particles. This belief is founded upon years of research, in many diverse fields, during which the atom was first discovered and then found to comprise of a shell of electrons orbiting a dense nucleus, which in turn was found to be made of protons and neutrons, and these in turn found to consist of quarks.

Following discoveries such as these, each at smaller distance scales, or higher energies, we continue to probe deeper and deeper in an attempt to discover what lies at the heart of all matter, and to develop the theory which describes how the ultimate particle(s) interact with each other to make what we see.

Modern particle physics has identified a set of apparently indivisible particles, and has formed a theory that explains all the current experimental data. Although this theory is not the complete description, it is the focus of research all over the world.

This theory is called "The Standard Model".

1.1 The Standard Model

It is currently thought that there are four fundamental forces and a small number of elementary particles which are influenced by these. The Standard Model successfully describes the interaction of three of these forces - the electromagnetic, weak and strong forces. At the energies current accelerators can attain, the fourth force, gravitation, is very weak in comparison to the others and so is omitted.

The elementary particles come in two species:

- BOSONS - particles with spin $0\hbar$, $1\hbar$, $2\hbar$, etc.
- FERMIONS - particles with spin $\frac{1}{2}\hbar$, $\frac{3}{2}\hbar$, etc.

1.1.1 Gauge Bosons and Forces

Bosons are the mediating particles of the fundamental forces.

Gravity is thought to be mediated by the graviton, a massless particle of spin-2. Although gravity is a weak force, it acts on all matter and is always attractive, hence its effects are cumulative. However at current energies the effect of gravity on particle interactions is immeasurably small; also the graviton has not been observed yet.

Electromagnetism is the force acting on electric charges and it is mediated by a massless spin-1 boson of zero charge called the photon. The photon couples to all charged particles. As the photon is electrically uncharged it does not self interact; hence as the photon is massless this force has infinite range. Electromagnetism is described with a very high level of accuracy by the theory of Quantum ElectroDynamics - QED (see section 1.1.6).

The strong force couples to particles carrying colour charge, eg. quarks, and is the strongest force known in nature. However, although the mediating boson, the gluon, is massless, it does carry colour charge, and so is able to interact with other gluons. This self-interaction limits the range of the force. The theory describing this force is Quantum ChromoDynamics - QCD (see section 1.1.7).

The weak force couples to all particles. It is mediated by the $W^{\pm}$ and the Z^0. These are heavy bosons and so this force has a finite range[1]. At an energy scale where these particles are produced, the weak force becomes as strong as the electromagnetic force, and these two forces have been successfully unified in the electroweak theory (see section 1.1.6).

[1] This can be seen from the uncertainty principle, $\Delta E \Delta t \leq \hbar$. So, particles with non-zero mass which are spontaneously created from the vacuum can only last a short time.

1.1.2 Fermions

Fermions are divided into two categories

- Quarks - which experience the strong force
- Leptons - which do not experience the strong force

In addition all fermions experience the weak force and charged fermions experience the electromagnetic force.

There are 6 flavours of quarks - down, up, strange, charm, bottom and top - and 6 types of leptons - electron, muon, tau, each with an associated neutrino. These can be grouped together to produce three generations where each generation contains a quark doublet and lepton doublet as shown in table 1.1. The generations appear to be almost identical in all aspects except for quantum numbers that describe the particles, eg. lepton number or flavour, also the mass of the particles increases and the lifetime decreases.

In addition there are partner anti-matter particles which are identical to those in table 1.1 but with their internal quantum numbers, such as charge or colour charge, reversed. Anti-particles are denoted either by a bar above the particle name (eg. $\bar{b}$ is the anti-particle to the b quark) or by the charge (eg. τ^+ is the anti-particle to the τ^-).

The quarks also occur with three different colour charges - red, green and blue. Due to the nature of the strong interaction, a 'free' quark is strongly attracted to other 'free' quarks, producing a colourless particle (either by joining with an anti-quark with the anti-colour, producing a meson, or by joining with two other quarks each with a different colour, which produces a baryon). This is called colour confinement and means that a free quark is never observed.

1.1.3 Generation Mixing

Quarks

The weak force does not couple to the quark generations shown in table 1.1 but rather to those given in table 1.2.

	Generation			Electric	Colour
	I	II	III	Charge	Charge
quarks	$\begin{pmatrix} u \\ d \end{pmatrix}$	$\begin{pmatrix} c \\ s \end{pmatrix}$	$\begin{pmatrix} t \\ b \end{pmatrix}$	$+\frac{2}{3}$ $-\frac{1}{3}$	R, G, B R, G, B
leptons	$\begin{pmatrix} \nu_e \\ e \end{pmatrix}$	$\begin{pmatrix} \nu_\mu \\ \mu \end{pmatrix}$	$\begin{pmatrix} \nu_\tau \\ \tau \end{pmatrix}$	0 -1	0 0

Increasing mass $\rightarrow$

$\leftarrow$ Increasing lifetime

Table 1.1: The fermion generations.

Generation		
I	II	III
$\begin{pmatrix} u \\ d' \end{pmatrix}$	$\begin{pmatrix} c \\ s' \end{pmatrix}$	$\begin{pmatrix} t \\ b' \end{pmatrix}$

Table 1.2: The Weak Quark Generations.

The quark states d', s' and b' are linear combinations of the physically observed states given by the Kobayashi–Maskawa matrix (equation 1.1).

$$\begin{pmatrix} d' \\ s' \\ b' \end{pmatrix} = \begin{pmatrix} V_{ud} & V_{us} & V_{ub} \\ V_{cd} & V_{cs} & V_{cb} \\ V_{td} & V_{ts} & V_{tb} \end{pmatrix} \begin{pmatrix} d \\ s \\ b \end{pmatrix} \tag{1.1}$$

This matrix is almost diagonal so the majority of the weak decays are $t \rightarrow b \rightarrow c \rightarrow ...$, however the small off-diagonal entries allow some coupling between the generations. The individual matrix elements are determined from weak decays of the relevant quarks and the 90% confidence limits for the magnitude of these, assuming only three generations, are:

$$\begin{pmatrix} 0.9745 - 0.9757 & 0.219 - 0.224 & 0.002 - 0.005 \\ 0.218 - 0.224 & 0.9736 - 0.9750 & 0.036 - 0.046 \\ 0.004 - 0.014 & 0.034 - 0.046 & 0.9989 - 0.9993 \end{pmatrix} \tag{1.2}$$

Details of the decays used to measure the matrix elements are given in [1].

Leptons

The Standard Model predicts that there is no mixing between the lepton generations. This leads to the conservation of lepton family number in all Standard Model processes.

1.1.4 Gauge invariance

In Quantum Field Theory all fermions are described in terms of complex fields in the Lagrangian of the system with a physically unobservable phase. It is required that the Lagrangian is invariant under an arbitrary local phase transformations which is called a gauge transformation.

Quantum Field theory specifies the form of the fermion Lagrangian, and it is seen that under some gauge transformations the Lagrangian is not invariant. To fix this problem new fields are added that transform differently from the fermion fields and in such a way as to restore the invariance. These new fields are seen to correspond to the gauge bosons.

All the interactions described in the Standard Model can be described in this way, the electromagnetic force described by QED is described using the simplest transformation, U(1) [2], which introduces a single gauge field corresponding to the photon. The other forces are described using more complicated transformations.

1.1.5 Renormalisability

All models have to make predictions that can be observed and tested. The predictions of a quantum field theory are obtained using perturbation theory, but this may introduce divergent integrals into the calculation. In order to calculate anything these infinities have to cancel out in the prediction of any observable quantity, and this is know as "renormalisation". All the theories in the Standard Model can be renormalised.

QED renormalisation can be illustrated with e^+e^- annihilation into a photon. The zeroth order diagram is shown in figure 1.1(a) and the well behaved first order perturbation is shown in figure 1.1(b). The contributions from each diagram can be calculated and their effects are seen in precision experiments.

Figures 1.1(c) and (d) also contribute to the process. However the creation (and subsequent annihilation) of the fermion pair by the photon, and the emission and reabsorption of a photon by the incoming electron are both purely internal to one line of the original Feynman diagram. In these cases the momenta of the internal lines are free, and hence have to be integrated over an infinite range. Such integrals are divergent.

The solution to this problem is to mathematically combine all such diagrams into the definition of the fermion or boson lines of Feynman diagrams. In the case of figure 1.1(c) the infinity is absorbed by saying the "bare" charge of the electron is infinite, and the observed finite charge is explained as the shielding effect of all the virtual activity which surrounds the electron. This shielding arises from electrons emitting virtual photons, which convert into virtual $f\bar{f}$ pairs, the charge of the

[2] See Appendix A.

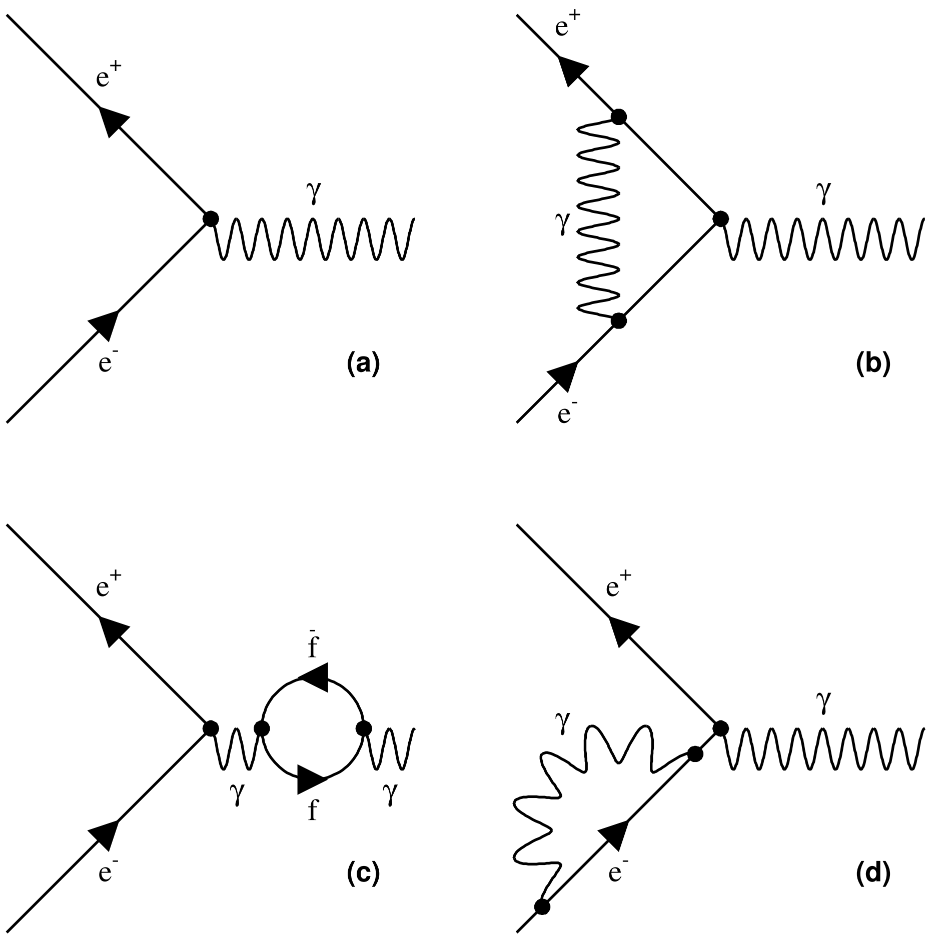

Figure 1.1: Feynman diagrams of e^+e^- annihilation vertex showing

(a) the zeroth order diagram

(b) a first order perturbation

(c) a divergent process with internal fermion pair production

(d) a divergent process with an internal photon.

electron polarises the surrounding sea of virtual pairs. It is this that corresponds to the higher order internal Feynman diagrams for the single electron line.

As a consequence of this, the more penetrating the probe into the electron structure (eg. the higher the collision energy), more of the surrounding shielding is passed, and so the charge of the electron appears larger, which in turn is accounted for in the theory by a running electromagnetic coupling constant, α_{em}, which increases with increasing momentum transfer.

The running of α_{em} is measured in Chapter 7.

1.1.6 Electroweak Theory

The unification of the electromagnetic and weak forces was proposed by Glashow-Salam-Weinberg. The theory contains three (positive, negative and neutral) massive vector fields, which are responsible for the weak interaction, and a single neutral massless vector field that describes the electromagnetic interaction (see below).

The weak interaction is parity violating, so the left- and right-handed fermions have to be treated differently. To do this the left-handed fermions are grouped into weak isospin doublets and the right-handed into isospin singlets as shown in table 1.3 for the first generation.

$$\begin{pmatrix} \nu_e \\ e \end{pmatrix}_L \quad \begin{pmatrix} u \\ d' \end{pmatrix}_L \quad e_R \quad u_R \quad d_R$$

Table 1.3: The weak isospin doublets and singlet for the first generation. d' is the weak interacting fermion state given in section 1.1.3.

The ν was thought to be massless and so there was no right-handed neutrino, however recent results [2] from the Super-Kamiokande experiment indicate that a neutrino of one species slowly transforms (oscillates) into that of another species as it moves. Theories of neutrino mass predict that each physically observed neutrino is a linear combination of several mass eigenstates (in a similar way to the d, s, and b quarks), and the oscillation is caused by the time dependent changes to the relative phases of these states, and hence the oscillation is a direct result of the neutrino mass.

The doublets transform under the gauge group for the weak force, $\mathrm{SU(2)_L}$, and all the fermions transform under the weak hypercharge group, $\mathrm{U(1)_Y}$, where the hypercharge, Y, is defined by

$$Q = T^3 + \frac{Y}{2} \tag{1.3}$$

Q is the electric charge and T^3 is the third component of weak isospin; $T^3 = 0$ for the isospin singlets and $T^3 = \pm\frac{1}{2}$ for the doublets.

The electroweak transformation is $\mathrm{SU(2)_L} \times \mathrm{U(1)_Y}$, mathematically this is:

$$E_L \rightarrow E'_L = e^{ig'\frac{1}{2}\Lambda - ig\frac{1}{2}\vec{\sigma}.\vec{\Lambda}} E_L \tag{1.4}$$

$$e_R \rightarrow e'_R = e^{ig'\frac{1}{2}\Lambda} e_R \tag{1.5}$$

where e_R represents a right-handed singlet, E_L a left-handed doublet, g and g' are the weak isospin and hypercharge coupling constants, $\vec{\sigma}$ is the vector of three matrices[3] representing the SU(2) group and Λ and $\vec{\Lambda}$ are arbitrary variables defining the transformation.

Invariance of the fermion Lagrangian requires four new fields to be introduced, W^1, W^2 and W^3 coupling to the weak isospin and B coupling to the weak hypercharge. The correct parity violating properties of the $W^\pm$ are obtained by a linear combination of the W^1 and W^2 fields, and the correct properties of the Z^0 and γ are obtained from linear combinations of the W^3 and B fields as shown below

$$W^\pm = W^1 \mp iW^2 \tag{1.6}$$

$$\gamma = B\cos\theta_W + W^3\sin\theta_W \tag{1.7}$$

$$Z^0 = -B\sin\theta_W + W^3\cos\theta_W \tag{1.8}$$

[3] These are usually chosen to be the Pauli spin matrices

where θ_W is the weak mixing angle, also called the Weinberg angle, which governs the relative strengths of the electromagnetic and weak forces through

$$g \sin\theta_W = e = g' \cos\theta_W \tag{1.9}$$

The relationship between the masses of the $W^\pm$ and the Z^0 is

$$M_W = M_Z \cos\theta_W \tag{1.10}$$

1.1.7 Quantum ChromoDynamics

Quantum ChromoDynamics (QCD) is the field theory describing the strong interaction between the colour charges of quarks and gluons. It is based to the SU(3) group. The theory has an octet of coloured gauge bosons, the gluons.

Unlike QED, the strong coupling constant, α_s increases with distance and is very small at small distances. This is know as asymptotic freedom. This feature is also seen in interactions at various momentum transfers. For low energy interactions, $\alpha_s \approx 1$ and hence is too large to allow perturbative calculations to be performed. However at high momentum transfer predictions can be made using perturbation theory.

The behaviour of the strong coupling constant means that although it is possible to calculate interactions at small distances[4], such as gluon radiation in the process $e^+e^- \to q\bar{q}$, when the quarks in this process separate and fragment into observable particles forming a jet of baryons and meson, the composition of this jet can only be modelled empirically[5].

1.1.8 The Higgs Mechanism

The final aspect of the standard model is the Higgs mechanism. The electroweak theory loses its gauge invariance when masses are added into the Lagrangian and so the predictive value is lost. This problem is solved by introducing the Higgs field,

[4] When the energy is large α_s is small, hence the perturbation calculation converges.
[5] The energy is small so α_s is large and the perturbation expansion does not work.

which allows the spontaneous breaking of the symmetry. Although the Lagrangian is symmetrical, the vacuum state symmetry is broken and this allows particles to have mass. However the underlying symmetry allows the theory to be renormalisable.

To illustrate this take the case of the Gauge group U(1). One of the possible forms for the potential, V, of the Higgs field, ϕ is

$$V(\phi^*\phi) = -\mu^2\phi^*\phi + \lambda(\phi^*\phi)^2 \tag{1.11}$$

where μ and ρ are arbitrary constants.

When ϕ is of the form $\frac{1}{\sqrt{2}}\rho e^{ix}$, this potential takes the form

$$V(\rho) = -\frac{1}{2}\mu^2\rho^2 + \frac{\lambda}{4}\rho^4 \tag{1.12}$$

The form of this potential in the two cases $\mu^2 > 0$ and $\mu^2 < 0$ are illustrated in figure 1.2. As required both are symmetrical about the origin, but when $\mu^2 < 0$ (figure 1.2(b) the origin is a local maximum, with an infinite set of minima, connected by U(1) transformations at $\nu = \frac{2\mu^2}{\lambda}$. When one of these minima is chosen as the vacuum state, the symmetry is broken.

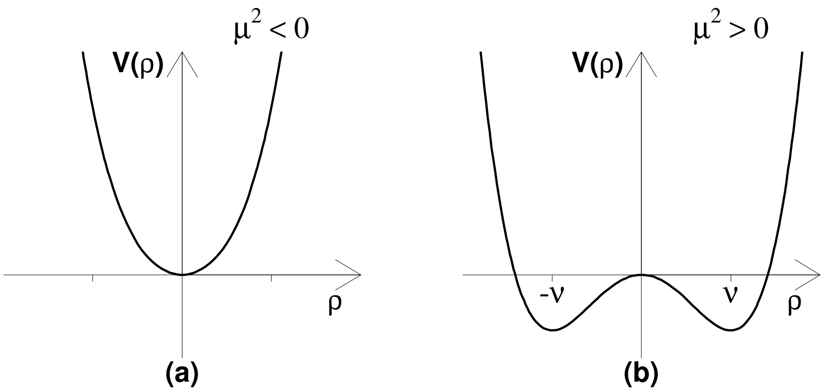

Figure 1.2: Possible Higgs field potentials.

In the Standard Model, four Higgs fields are introduced, in the form of weak isospin doublets of complex scalar fields, with couplings such that the vacuum has weak isospin and hypercharge to which the particles can couple, generating mass terms. When three of the Higgs fields are combined with the weak bosons the particles become massive as required, and only one observable Higgs field remains, the neutral Higgs boson.

The Higgs mechanism therefore allows particles to have mass, although it makes no predictions as to what these masses are. The coupling strength of the Higgs to the fermions is proportional to the fermions mass.

The Higgs boson has yet to be discovered although, at a 95% confidence level, its mass is currently constrained to be greater than around 77.5 GeV [3] by all four LEP experiments. In addition, a fit to all measured Standard Model parameters [4] not only insists that the Higgs mass is less than 1 TeV, the measurements prefer a light Higgs.

1.2 Beyond the Standard Model

Although the Standard Model is currently very good at predicting all the current experimental results it is not considered to be a final theory. In a similar way to Newtonian mechanics being a low energy approximation to relativistic mechanics, the Standard Model may be part of something bigger. Precisely what the larger theory includes is still unknown.

Firstly, and most obviously, the Standard Model is missing gravity from its framework and to fully describe the universe this has to be included. There are many "Grand Unification Theories" but, as yet, none of them have predictions that are testable at the energies that will be reached by accelerators in the near future. In addition the Standard Model does not explain why the visible universe does not consist of matter and anti-matter in equal quantities, nor why there are three generations of constituents, nor does it predict the masses of the particles.

A possible extension to the Standard Model is the existence of a 4^{th} generation of particles, or of a heavy Z-like boson, the Z′. Precision LEP measurements on the invisible decay width of the Z^0 have constrained the number of ν species with masses less than $\frac{M_Z}{2}$ (and hence the number of generations) to be 2.989 ± 0.012 [5].

It is also possible that the leptons and quarks are themselves composite particles (and hence would exist in excited states), or combine to form a particle called a leptoquark. As yet there is no evidence that either of these scenarios exist and the 95% confidence limit on the mass of an excited lepton, of any type, from pair production is greater than 80 GeV [6].

Supersymmetry is currently the most favoured extension of the Standard Model, but as yet there is no experimental evidence of its existence. It predicts that every fermion (boson) has a supersymmetric partner boson (fermion)[6]

There are many different Supersymmetry theories of which the simplest is the Minimal Supersymmetric Standard Model (MSSM); in addition to the supersymmetric partners mentioned above, it also includes two Higgs doublets with hypercharge, Y= ± 1, which help generate the masses of both the up and down type quarks and also of the charged leptons. In this theory the lightest supersymmetric particle (LSP) is stable. For consistency with cosmological measurements this LSP has to be electrically and colour neutral, hence it is normally called the 'neutralino', $\tilde{\chi}^0$.

A further extension to Supersymmetry is Superstring theory, where the superstring is the single fundamental "particle" in the universe, and each lepton, quark, and boson is a different mode of oscillation of the superstring.

Also, the visible mass in the galaxies is around an order of magnitude too small to explain the measured velocity at large distances from the galactic centre. To account for this the mass of the galaxies is increased by postulating the existence of unseen mass, known as "Dark Matter".

So, in spite of the success of the Standard Model, there is still a lot left to investigate.

[6] This partner is denoted with the same symbol as its Standard model counterpart but with a tilde, $\tilde{}$, above it. The name given to the supersymmetric partner is the name of the Standard model counterpart but with an 's' added in front for the fermions, or ending with 'ino' for the bosons. So, the muon, μ, which is a fermion has a supersymmetric partner smuon boson, $\tilde{\mu}$, and the photon, γ, which is a boson has a partner photino fermion, $\tilde{\gamma}$.

Chapter 2

LEP and the OPAL detector

To test the Standard Model predictions and to search for new phenomena large machines are used to accelerate particles to high energies before colliding them, either into a fixed target (as with experiments on the Super Proton Synchrotron (SPS) at CERN), or a particle of different type (as performed at the Hadron-Electron Ring Accelerator (HERA) at DESY), or with the antimatter partner (as at the Large Electron Positron (LEP) accelerator at CERN).

To observe the particles produced in these collisions, large detectors are built which, where possible, identify and measure the momentum and energy of the particles.

This chapter gives an overview of the LEP accelerator and the OPAL detector.

2.1 The LEP Collider

The Large Electron Positron (LEP) accelerator [7] is a synchrotron collider which annihilates electrons with positrons at centre-of-mass energies between 80 and 200 GeV. The accelerator is the largest in the world with a circumference of 26.7 km. The tunnel housing the machine varies in depth from 51 m to 143 m and is located close the Swiss - French border near Geneva.

Inside the storage ring bunches of electrons and positrons circulate in opposite directions and are made to collide at the four interaction points where the detectors are located. (See section 2.2)

2.1.1 Pre-acceleration and Injection

The injection system used to introduce the electrons and positrons into LEP is shown in figure 2.1. It begins with electrons stripped from a heated filament and accelerated in the LEP Injector Linac (LIL) to 200 MeV. These are directed onto a tungsten target where e^+e^- pairs are produced by bremsstrahlung photons emitted during the rapid deceleration of the electrons. The positrons are separated by a magnetic field and both the electrons and positrons are accelerated to 600 MeV in the second part of LIL and stored in the Electron Positron Accumulator (EPA) ring. This machine has a circumference of 126 m and stores the particles until there are enough to warrant transfer to the Proton Synchrotron (PS) which is one of the older CERN accelerators with a 200 m circumference. In the PS the particles are accelerated to 3.5 GeV and are then injected into the 2.2 km circumference Super Proton Synchrotron (SPS). In the SPS the particles are accelerated to 22 GeV and injected into LEP. Although the SPS is used for fixed target experiments, using it as part of the LEP injection system does not affect this program due to the dead-time of the pulsed proton cycle.

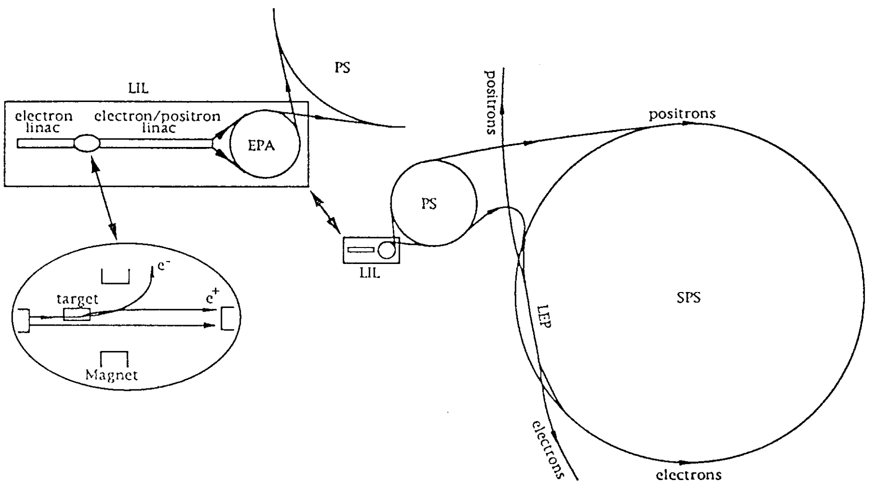

Figure 2.1: The LEP injection system.

2.1.2 LEP Circulation and Acceleration

The beams in LEP circulate for periods up to 12 hours and to achieve this the particles have to be transported in an evacuated beam pipe, the pressure of which is less than 3×10^{-9} torr. This prevents losses due to beam-gas collisions. To keep the particles travelling in a circular orbit there are over 3300 dipole bending magnets and nearly 2000 focusing magnets (quadrupole, sextupole and octupole). The dipole magnets have a field of approximately 0.1 T, and are aligned to a relative precision of better than 0.1mm over a distance of several kilometres. These magnets fill almost 75% of the circumference of LEP.

As the orbit of the electrons and positrons is almost circular, they are continually accelerated and so emit synchrotron radiation. The energy loss, δE per revolution is given by:

$$\delta E = \frac{4\pi}{3} \frac{e^2 \beta^2 \gamma^4}{R} \tag{2.1}$$

where R is the radius of the ring, β is the particle velocity as a fraction of the speed of light, $\gamma = (1 - \beta^2)^{-1/2}$, and e is the charge of the electron

For high energy electrons or positrons this becomes

$$\delta E \approx 0.0885 \frac{E^4}{R} \tag{2.2}$$

where δE is in MeV, E (in GeV) is the energy of the particle and R is in metres.

To replace this energy loss on each revolution (which is 128 MeV per particle at 45 GeV increasing by a factor of over 20 for 100 GeV beams), and to accelerate the particles to high energy LEP required 128 copper radio frequency accelerating cavities, powered by sixteen 1 MW klystrons for the Z^0 running. These are steadily replaced by superconducting niobium coated cavities for the high energy running (see section 2.4).

As there are four bunches of both electrons and positrons, with the order of 10^{11} particles per bunch, the synchrotron radiation energy loss dominates the large power requirements of the LEP accelerator.

2.2 The LEP detectors

There are four detector at LEP which have been operating since the commissioning of the collider in August 1989. The detectors ALEPH [8], DELPHI [9], L3 [10] and OPAL [11] have generally the same aims and so there are some similarities in design. Each detector has a tracking chamber in a magnetic field for the identification of charged tracks, calorimeters for measuring the energy of electromagnetic and hadronic showers, and outer tracking layers for muon identification. In detail the experiments are considerably different. OPAL was designed with conventional technology at the time of proposal, while ALEPH was design using more advanced technology such as superconducting magnets and a Time Projection Chamber. DELPHI is an even more advanced detector including a Ring Imaging Cerenkov counter for particle identification. L3 was designed for very precise lepton identification and measurement.

As all four experiments are different, independent results are obtained, often with different systematic errors, which can be combined to give a more precise measurement than can be obtained from a single detector. Also as the detectors have different capabilities the collaborations can concentrate on particular reactions for which their detector is the most competitive.

This thesis describes the analysis of data recorded by the OPAL detector which is described in more detail below.

2.3 The OPAL detector

The Omni Purpose Apparatus for LEP (OPAL) is designed to reconstruct all types of e^+e^- collision events (except for those that produce only undetectable neutrinos). The detector consists of a set of concentric cylindrical subdetectors centred on the interaction point and a set of endcap subdetectors, covering the ends of the cylinders, which maximises the angular acceptance giving almost 4π coverage. A schematic view of the detector is shown in figure 2.2

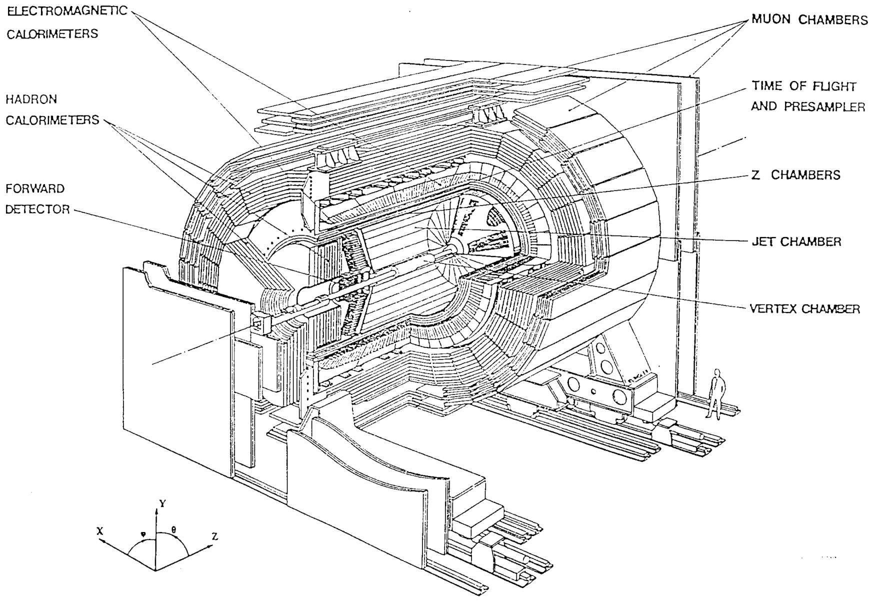

Figure 2.2: The OPAL detector.

2.3.1 The OPAL Co-ordinate System

The OPAL co-ordinate system is a right-handed Cartesian system originating at the centre of the jet chamber. The z axis is in the direction of electrons in LEP, the x axis is towards the centre of LEP and the y axis is slightly away from the vertical as the LEP ring is slightly inclined. The angle θ is the polar angle measured from the positive z axis, and ϕ is the azimuthal angle measured clockwise from the x axis looking along the positive z axis.

2.3.2 The Central Detector

In the centre of OPAL is the beryllium beam pipe which is 0.11 cm thick and has an outer radius of 5.35 cm. The central detector is located inside the OPAL solenoid which supplies a uniform axial magnetic field of 0.435 T. This detector consists of four subdetectors, which (in order of increasing radius) are a Silicon Microvertex detector (SI), and three drift chambers located inside a pressure vessel where the pressure is maintained at 4 bar. The three drift chambers are the vertex detector (CV), the jet chamber (CJ) and z-chambers (CZ).

SI

The SI detector [12] was originally installed in 1991, but has been upgraded in 1993, 1995 and 1996. It now consists of two barrels of single sided Silicon Microstrip Detectors located at radii of 6 and 7.5 cm from the centre of the detector. The inner layer consists of 12 ladders and the outer of 15 ladders. The ladders are tilted to avoid gaps in ϕ and each ladder consists of 5 silicon wafers. There are 629 strips per detector at 25 μm pitch, but only every other strip is read out giving effectively a 50 μm pitch. The detector has $r-\phi$ and $r-z$ wafers glued back to back.

It is particularly useful for precision measurements of short lived particles as it gives a spatial resolution of 5 - 10 μm in both planes.

CV

The CV detector [13] is a high precision cylindrical jet drift chamber, with an inner radius at a distance of 10.3 cm from the beam pipe. It is 1 m long and has a radius of 23.5 cm, and is divided into 2 layers of 36 sectors. The inner layer sectors each contain a plane of 12 wires running parallel (axially) to the beam pipe. Measurement of the drift time on to these wires allows high precision (55 μm) measurements in $r-\phi$. The outer layer sectors each consist of a plane of six stereo wires inclined at 4° to the beam pipe giving a coarse (700 μm) measurement in $r-z$.

CJ

The CJ detector [14] is a 4 m long cylindrical drift chamber covering a radial distance of 25 - 185 cm. It is made of 24 identical sectors each with 159 wires parallel to the beam pipe. As for CV, measurement of the drift time allows a measurement in $r-\phi$, and charge measurement at each end of the wires allows a measurement in z. Summation of the charge received at each end of the wires also allows calculation of the energy loss, dE/dx, which can be used for particle identification. Tracks can be reconstructed in the region $|\cos\theta| < 0.98$, although the reconstruction becomes progressively poorer in the region $|\cos\theta| > 0.73$ as the number of wires being hit is reduced.

CZ

The CZ detector [15] gives a precise measurement of the z co-ordinate of tracks as they leave the jet chamber; it covers the region $|\cos\theta| < 0.72$. There are twenty-four 4 m long drift chambers which are divided into eight 50 cm by 50 cm cells each of which are 5.9 cm thick. Each cell contains six wires which are perpendicular to the z direction. This allows the z co-ordinate to be resolved to around 300 μm, and charge separation gives an $r-\phi$ measurement with a resolution of 15 mm.

Track Parameters

The measurement of tracks leads to another two useful parameters, d_0 and z_0. The distance of closest approach, d_0, of the track extrapolated to the interaction point in the $r-\phi$ plane is defined to be positive if the curvature of the track encloses the interaction point, and z_0 being the z co-ordinate at the point of closest approach in the $r-\phi$ plane.

2.3.3 The Electromagnetic Calorimeter (ECAL)

The electromagnetic calorimeter is used to detect, identify and measure the energy of electrons and photons. It is made of a lead glass total absorption calorimeter split into a barrel detector (EB) and two end cap arrays (EE) and covers almost 99% of the solid angle. In front of the calorimeter there are approximately 2 radiation lengths of material (mainly due to the solenoid and pressure vessel), which results in most electromagnetic showers being initiated before reaching the lead glass. Hence presampling devices are installed in front of the lead glass in the barrel (PB) and endcap (PE) regions. These measure the position and energy of showers which start before the lead glass and improve the spatial and energy resolution as well as giving additional γ/π^0 and electron/hadron discrimination. In front of the barrel presampler is the barrel Time of Flight (TOF) Detector (TB). During the 1995/96 winter shutdown the Tile Endcap (TE) system was installed between the presampling endcap and the electromagnetic endcap. These two detectors provide precise timing information over almost the full angular coverage of OPAL.

TB

This subdetector is almost 6.84 m long with a mean radius of 236 cm and surrounds the OPAL coil. It consists of 160 scintillation counters and covers the region $|\cos\theta| < 0.82$. It provides low momentum (0.6 to 2.5 GeV) charged particle identification, fast triggering information and an effective rejection of cosmic rays (see section on Cosmic ray rejection).

PB

The PB detector [16] consists of 16 chambers forming a cylinder of radius 239 cm and length 662 cm, with polar angle coverage of $|\cos\theta| < 0.81$. Each chamber is a double layer of streamer drift tubes, with the anode wires running parallel to the beam direction and 1 cm wide cathode strips lying at $45°$. Spatial positions, with a resolution of 2 mm, are determined by reading out the strips and measuring the charge at each end of the wires. As the presampler hit multiplicity is roughly proportional to the energy deposited in the material in front of the presampler, the calorimeter shower energy can be corrected giving a corresponding improvement in resolution.

PE

The PE detector [17] consists of a number of thin multiwire proportional counters located between the pressure bell and the endcap lead glass detector, covering the region $0.83 < |\cos\theta| < 0.95$. There are 32 chambers arranged in 16 sectors, with wires lying perpendicular to the beam axis and strips running radially on one side of the chamber. This gives a position resolution of 4 mm.

EB

The EB detector consists of a cylindrical array of 9440 lead glass blocks at a radius of 246 cm and covers $|\cos\theta| < 0.82$. Each block is 24.6 radiation lengths in depth, 37 cm long with a cross-sectional area of 10×10 cm^2. The longitudinal axis of each block is angled to point near the interaction region but the focus is slightly offset from the collision point to reduce losses from particles passing through the gaps between the blocks. Cerenkov light from relativistic charged particles passing through the lead glass is detected by 3 inch diameter phototubes at the base of each block. There is almost complete absorption of electron and photon energy, with an energy resolution of $\frac{\sigma_E}{E} \approx \frac{15\%}{\sqrt{E}}$, and the use of shower profiling gives a spatial resolution of around 11 mm.

The energy deposited in the EB subdetector is grouped into clusters containing one or more neighbouring blocks; the cluster is considered good if there is a minimum energy of 100 MeV deposited in it.

EE

The EE detector [18] consists of two arrays of 1132 lead glass blocks[1] with lengths of 38, 42 and 52 cm, forming a dome shaped structure at each end of the detector. They are located between the pressure bell and the pole tip hadron calorimeter, and covers the region $0.81 < |\cos\theta| < 0.98$. The blocks are all aligned parallel to the beam axis, and typically consist of 22 radiation lengths of material. As the blocks lie in the full OPAL magnetic field they are read out by Vacuum Photo Triodes. The energy resolution is $\frac{\sigma_E}{E} \approx \frac{20\%}{\sqrt{E}}$, and the spatial resolution is similar to that achieved in the barrel region. This position resolution has to be calibrated with energy and particle type because the shower development is different due to the non-pointing geometry of the lead glass blocks.

As with the EB subdetector, the energy deposited in the EE subdetector is grouped into clusters. However, in this subdetector, the cluster has to contain two or more neighbouring blocks with a minimum energy deposit in the cluster of 200 MeV to be considered good.

TE

This subdetector, located between the PE and EE subdetectors, is a layer of scintillating tiles, which complement the existing barrel scintillators. It enhances the triggering information for the forward regions. The scintillation layer is 10 mm thick and is read out using fibres which carry the light to phototubes situated outside the

[1] The lead glass is slightly different to that used in the EB subdetector

solenoidal field.

2.3.4 The Hadron Calorimeter (HCAL)

The hadron calorimeter is built in three sections: the barrel region (HB) covers $|\cos\theta| < 0.81$, the endcaps (HE) $0.81 < |\cos\theta| < 0.91$ and the pole-tips (HP), extending the coverage to $|\cos\theta| < 0.99$. These subdetectors are positioned between the iron layers of the magnet return yoke so that a sampling calorimeter is formed, covering a solid angle of 97% of 4π. It offers at least 4 interaction lengths of iron absorber to particles emerging from the electromagnetic calorimeter, which consists of approximately 2.2 interaction lengths of material. Most hadrons are absorbed by the two calorimeters so that predominantly only muons pass on into the surrounding muon chambers.

HB and HE

The HB subdetector contains 9 layers of chambers alternating with 8 layers of 10 cm thick iron, and the HE subdetector contains 8 layers of chambers alternating with 7 layers of iron and they are built along similar lines [19].

Each chamber is a limited streamer tube device with anode wires 1 cm apart, whose the signals are only used for monitoring purposes. Typically the outer surface of the chambers are made up of 8 pads, which are grouped together to divide the detector into 48 ϕ-bins and 21 θ-bins. The induced charge collected on the pads in each chamber are summed to give an estimate of the energy of the hadronic shower in that region.

Running the full length of the inner surface of the chamber are 0.4 cm wide aluminium strips, which are centred above the anode wires and run parallel to the beam direction in the barrel and in the plane perpendicular to this in the endcap. Hits on the strips provide additional tracking information for muons.

HP

The HP subdetectors [20] consist of 10 layers of thin multiwire proportional chambers (thickness 0.7 cm) with anode wires separated by 0.2 cm. As for HB and HE the chambers have pads on one side and strips on the other, which are used for hadronic energy estimation and muon tracking.

2.3.5 The Muon Chambers

The muon chambers form the outermost layer of the detector in the barrel region (MB) and endcap region (ME). The charged particles that reach these detectors are predominantly muons.

MB

The MB detector [21] consists of 110 drift chambers arranged in 4 layers, covering the region $|\cos\theta| < 0.72$. The chambers vary in length between 6 and 10.4 m in order to fit round the magnet support leg, and each has a cross-sectional area of 120 $\times$ 9 cm.

Each chamber is split into two cells, each containing an anode signal wire running parallel to the beamline for the full length of the cell. The inner surfaces of the cells have 0.75 cm wide cathode strips etched on them which define the drift field. Directly opposite the anode wires are diamond shaped cathode pads with a repeated pattern every 17.1 cm and 171 cm respectively. Spatial position in ϕ is derived using the drift time onto the anode wire, with an accuracy for track reconstruction of better than 0.15 cm. A coarse z coordinate is obtained by using the difference in time and pulse height of the signals arriving at both ends of the anode wire. A more precise z coordinate, accurate to 0.2 cm (modulo 17.1 cm) or 3 cm (modulo 171 cm) is obtained from the induced signals on the two sets of diamond shaped pads.

ME

The ME detector [22] is composed of quadrant chambers each 6 m $\times$ 6 m and patch chambers each 3 m $\times$ 2.5 m. At both ends of the OPAL detector there are two quadrant chambers (an upper and lower) on each side of the beam pipe, and a patch chamber above and below the pipe with a slight overlap between the chambers to avoid acceptance gaps. This gives an angular coverage between $0.67 < |cos\theta| < 0.985$. The detector consists of two separated double layers of limited streamer tubes in the plane perpendicular to the beam line. Two of these layers have horizontal wires and the other two are vertical. The streamer tube profile has a cross section of 0.9 cm $\times$ 0.9 cm and the inner wall is coated with a carbon-suspension paint so that it acts as the cathode. On each side of the tubes, there are rows of 0.8 cm wide aluminium strips, which run parallel to the wires on one side and perpendicular on the other. The streamer tubes contain a gas mixture comprising 75% argon and 25% isobutane. The passing of the charged particle ionises the argon, which is then accelerated towards the strips by the high electric field. The passage of these charged particles causes an avalanche of further ionization. The isobutane is used keep the amplification to a manageable level by absorbing the photons produced in the avalanche, and it also prevents the chambers shorting by limiting the charge spread towards the cathode. The streamer position can be located with a precision of around 3 mm with the parallel strips. For the perpendicular strips this precision can be improved to around 1 mm by using an weighted average of the recorded pulse heights on adjacent strips.

2.3.6 The Forward Detector (FD)

The FD detector [23] is used to detect particles at very small angles (60 - 150 mrad) to the beam. This is particularly important as the low angle Bhabha scattering events detected can be used to determine the beam luminosity. In the region between 47 and 120 mrad the only obstruction comes from the beam pipe and 2 mm of aluminium from the central detector pressure vessel, which gives a very clean acceptance for this angular range. The detectors lie ± 2.6 m from the interaction point and consist of 35 sampling layers of a lead-scintillator sandwich forming a 20 radiation length electromagnetic calorimeter preceded by a 4 radiation length presampler and containing three layers of proportional tube chambers [24]. In addition a 7 radiation length ring of lead-scintillator sandwich (gamma catcher) plugs the acceptance gap between the inner edge of EE and the outer edge of the forward calorimeter. Finally there is a Far Forward monitor consisting of 20 radiation length lead scintillator calorimeters mounted either side of the beampipe, 7.85 m from the intersection region, this is used to detect electrons which have been deflected by the focusing quadrupoles.

2.3.7 The Silicon Tungsten detector (SW)

The SW detector [25] is also used for detecting the low angle Bhabha scattering events used for luminosity measurements. It was installed in 1993. There are two calorimeters (one at each end) each comprising 19 layers of silicon detectors and 18 layers of tungsten, located ≈ 2.4 m from the interaction point in the angular region $25 < |\cos\theta| < 59$ mrad.

The first layer of the silicon is used for detecting preshowering, the next fourteen layers are each located behind 1 radiation length of tungsten, and the final four layers are each behind 2 radiation lengths of tungsten.

2.3.8 The Minimum Ionising Particle (MIP) plug

This subdetector was installed for the start of the 1997 data taking and consists of 4 layers of 1 cm scintillator tiles located at each end of the detector. The two innermost layers are located just behind the gamma catcher and separated from each other by 5 mm of lead which reduces the background from synchrotron radiation. They cover the polar angular range of 126-220 mrad. The next layer is located just behind these and covers the angular region from 45 to 160 mrad. In ϕ these three layers are divided into quadrants. The outermost layer is situated between the SW and FD subdetectors and covers a polar angular range of 43-130 mrad, in ϕ it is divided into octants.

The subdetector is designed to provide good time resolution and detection efficiency for single minimum ionising particles such as muons.

2.3.9 The OPAL Trigger System

When LEP is running in 4×4 bunch mode there is a beam crossing rate of 45 kHz. Hence a possible event can occur every 22 μs and so the decision whether to record an event has to be processed quickly. As it takes 20 ms to read out each event, the OPAL trigger [26] is a piece of hardware designed to significantly reduce the recording of non-physics events such as detector noise, and collisions of the beams with the remaining gas in the beam pipe, or with the beam pipe itself. The trigger decision is made well within the 22 μs between bunch crossings.

The trigger uses information about the total energy sum and track counts from all subdetectors (except SI and PE) for 'stand-alone' triggering. In addition, the full solid angle is divided into 6 θ- and 24 ϕ-regions, and all subdetectors send out information about what they detect in these bins and the correlation between these signals is used as a second type of trigger. The two triggers are analysed in parallel to provide fast evidence for physics events. If an event is not triggered the whole detector is reset in time for the next bunch collision.

When LEP runs in other modes the beam crossing rate is increased so a set of pre-triggers [27] is used where the solid angle is divided up into only 6 ϕ segments for faster processing.

2.3.10 The Data Acquisition System

When an event is triggered a signal with an event number is sent to each sub-detector. Each sub-detector then reads out its data and processes it locally to reformat it and reduce the data size. This information is then sent to the OPAL event builder [28] which combines all the available information from each subdetector.

This is then passed to the filter [29]; this piece of software is the final selective stage. The filter checks and analyses the event, classifying it according to type (eg. multihadron, dilepton) and makes detailed checks to reject background events that passed the trigger. The data are then further compressed, written to disk and backed up onto tape.

Finally the events are passed to ROPE (Reconstruction of OPAL Events) [30], which uses OPCAL [31], a calibration database containing information from each subdetector which is used to correct for known problems, such as noisy channels, timing discrepancies or misaligned positioning of the subdetector. ROPE is a package that reconstructs either raw data or simulated data from GOPAL [32] (see section 2.3.11). The output from ROPE contains all the useful information about the tracks and clusters in the event such as the energy, momentum or particle identity, which is stored on the Data Summary Tape (DST) for use in the analysis.

2.3.11 The OPAL Detector simulation

All the characteristics of the OPAL detector, including its dimensions and the material used in its construction, are used as inputs to the modelling package GEANT [33]. Event generators such as KORALZ [34], GRACE4F [35] or FERMISV [36], are used to create various types of processes in the proportions predicted by theoretical models. The particles produced in these events are then processed through GEANT which models the output of the subdetectors according to the probability of interaction at each point, the noise, resolution, etc. This Monte Carlo simulation of OPAL events is know as GOPAL (Geant at OPAL), which is passed through ROPE the same way as normal data, although cheat information is also made available (such as the actual momentum and identity).

2.4 The LEP energy upgrade

Until October 1995 the four experiments at LEP were concentrating on making precision electroweak measurements around the Z^0 production peak at a collision energy around 91 GeV. Since then LEP has been upgraded to reach higher energies to study other aspects of the weak force, including W pair production and to maximise the discovery potential.

The first stage of the upgrade occurred during October 1995, when sixty of the superconducting accelerating cavities were installed replacing eight of the 128 copper cavities which were in use at the time, allowing collision energies of 130 - 140 GeV to be reached. During November 1995 (LEP1.5) data were taken at 130, 136 and 140 GeV. Approximately 2.5 pb^{-1} of data were taken at both 130 GeV and 136 GeV.

During the 1995/96 winter shutdown a further eighty-four superconducting cavities were installed allowing LEP to reach 161 GeV which is above the production threshold for W pairs. This was the start of the LEP2 era. Approximately 10.0 pb^{-1} of data were taken at a collision energy of 161 GeV during July and August 1996. In September 1996 twenty-eight more superconducting cavities were installed bringing the energy up to 170 - 172 GeV. Approximately 1.0 pb^{-1} of data were taken at 170 GeV and 9.3 pb^{-1} at 172 GeV during November 1996.

In the 1996/97 winter shutdown, 34 copper cavities were replaced by a further sixty-eight superconducting cavities, and energies of 181 - 184 GeV were achieved. After a delay, due to a fire affecting the SPS accelerator, LEP delivered 57 pb^{-1} of data in this energy range. For one week at the beginning of October 1997 LEP once again ran at 130 and 136 GeV, taking around 3 pb^{-1} of data at each energy. This weeks running was to check an effect seen by ALEPH during the LEP1.5 run, where an excess of events with a mass around 105 GeV were seen in 4 jet events [37].

Over the winter shutdowns in 1997/8 and 1998/9 all the remaining copper cavities will be replaced and by the end of the LEP2 run a total of 500 pb^{-1} of data will have being delivered. From the end of May until the middle of August 1998 LEP delivered approximately 75 pb^{-1} of data at 189 GeV. For the 1999 and 2000 operation it is hoped that LEP will reach a maximum energy of 200 GeV. When this programme is completed LEP will be decommissioned to allow the building of the Large Hadron Collider (LHC) in the same tunnel.

Chapter 3

The Process $e^+e^- \to \mu^+\mu^-$ or $\tau^+\tau^-$

The measurement of the fermion pair products produced in e^+e^- annihilation at LEP can be used to test many of the predictions of the Standard Model, and to search for evidence of new physics.

The hadronic products test QCD predictions, but this is relatively complicated due to the difficulty in identifying the initial quarks. The neutral leptonic products are invisible. Although electron pair production is very simple to identify and measure, there is an added complication that the production has contributions from both e^+e^- annihilation into Z/γ which then decays into e^+e^- (s-channel) and from scattering of the initial particles (t-channel).

The final fermion pair channels, that of the μ and τ pairs, are very similar processes, occurring only through the s-channel, and it is relatively easy to calculate the predictions of the Standard Model.

This chapter describes the theoretical predictions for μ pair production. The predictions for τ pair production are analogous. However there are small differences due to $m_\tau > m_\mu$, but these are almost negligible as the masses are small compared to the Z^0.

3.1 Cross-section

In the Standard Model the reaction $e^+e^- \to \mu^+\mu^-$ occurs through the exchange of a Z^0 or γ and the simplest Feynman diagrams for this process are shown in figure 3.1.

There is also a contribution from the exchange of a Higgs boson, but as the Higgs boson couples very weakly to the e^+e^- this contribution is negligible.

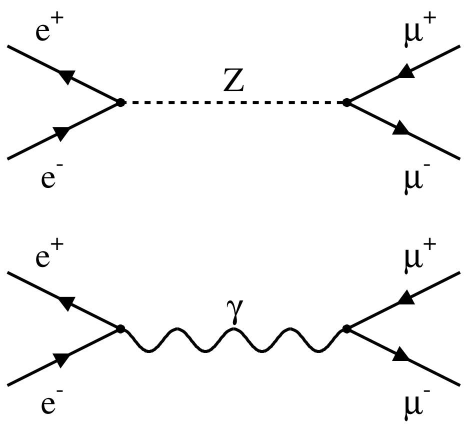

Figure 3.1: The zeroth order (Born level) Feynman diagrams of the processes involved in the reaction $e^+e^- \rightarrow \mu^+\mu^-$.

For a general fermion the electromagnetic coupling is given by $ieQ_f\gamma^\lambda$, and the neutral weak coupling by $\frac{ie}{4\sin\theta_W\cos\theta_W}\gamma^\lambda(c_V^f - c_A^f\gamma^5)$ [1] where

- e is the charge of the electron, Q_f is the charge of the fermion in electron units
- γ_μ ($\mu = 1 - 4$) are the gamma matrices:

$$\gamma^0 = \begin{pmatrix} 1 & 0 \\ 0 & 1 \end{pmatrix}, \quad \gamma^{\vec{\sigma}} = \begin{pmatrix} 0 & \vec{\sigma} \\ -\vec{\sigma} & 0 \end{pmatrix}, \quad \gamma^5 = \gamma^0\gamma^1\gamma^2\gamma^3,$$

  $\vec{\sigma}$ are the Pauli matrices:

$$\sigma_1 = \begin{pmatrix} 0 & 1 \\ 1 & 0 \end{pmatrix} \quad \sigma_2 = \begin{pmatrix} 0 & -i \\ i & 0 \end{pmatrix} \quad \sigma_3 = \begin{pmatrix} 1 & 0 \\ 0 & -1 \end{pmatrix}$$

- θ_W is the weak mixing angle

[1] For the weak charged current $c_V = c_A = \frac{1}{2}$ and the coupling has a vector-axial structure. For the neutral weak current the charged leptons have $c_V \simeq 0$ and so here the coupling is almost entirely axial. This is the reason that the neutral and charged weak currents behave very differently.

- $c_A = T^3$ is the axial coupling factor for the particle, where T^3 is the third component of weak isospin.

- $c_V = c_A - 2Q_f \sin^2\theta_W$ is the vector coupling factor for the particle

The standard model predicts that c_V and c_A do not change between generations. For leptons this is known as lepton universality and so determining these factors for all leptons is important.

For $e^+e^- \to \mu^+\mu^-$ the probability amplitudes are

$$M_\gamma = -\frac{e^2}{k^2}(\bar{v}_\mu\gamma^\lambda u_\mu)(\bar{v}_e\gamma_\lambda u_e) \tag{3.1}$$

and

$$\begin{aligned} M_Z &= -\frac{g^2}{4cos^2\theta_W}(\bar{v}_\mu\gamma^\lambda(c_V^\mu - c_A^\mu\gamma^5)u_\mu)\left(\frac{g_{\lambda\rho} - \frac{k_\lambda.k_\rho}{m_Z^2}}{k^2 - m_Z^2}\right)(\bar{v}_e\gamma^\rho(c_V^e - c_A^e\gamma^5)u_e) \\ &= -\frac{\sqrt{2}Gm_Z^2}{s - m_Z^2}(c_R^\mu\bar{v}_{\mu R}\gamma^\lambda u_{\mu R} + c_L^\mu\bar{v}_{\mu L}\gamma^\lambda u_{\mu L})(c_R^e\bar{v}_{eR}\gamma_\lambda u_{eR} + c_L^e\bar{v}_{eL}\gamma_\lambda u_{eL}) \end{aligned} \tag{3.2}$$

where

- $k_{\lambda(\rho)}$ are the 4-momenta of the incoming particles. Hence $s = k^2$, which is equivalent to the centre-of-mass energy squared.

- $u(v)$ is the 4-spinor of the particle (antiparticle), u_L and u_R with left and right helicity:

$$u = \sqrt{E+m}\begin{pmatrix} \chi_r \\ \frac{\vec{\sigma}.\vec{p}}{E+m}\chi_r \end{pmatrix}, \quad v = \sqrt{E+m}\begin{pmatrix} \frac{\vec{\sigma}.\vec{p}}{E+m}\chi_r \\ \chi_r \end{pmatrix},$$

$$\chi_r = \begin{pmatrix} 1 \\ 0 \end{pmatrix} \quad \textit{for a particle with spin up}$$
$$\qquad \begin{pmatrix} 0 \\ 1 \end{pmatrix} \quad \textit{for a particle with spin down}$$

E, m, and p are the energy, mass and 3-momentum of the particle

- $\bar{u} = u^\dagger \gamma^0$

- $g_{\lambda\rho}$ is the space metric:

$$g_{\lambda\rho} = \begin{pmatrix} 1 & 0 & 0 & 0 \\ 0 & -1 & 0 & 0 \\ 0 & 0 & -1 & 0 \\ 0 & 0 & 0 & -1 \end{pmatrix}$$

- G is the Fermi coupling constant $G = \frac{\sqrt{2}g^2}{8m_W^2}$

- $c_{L(R)} = c_V \pm c_A$ are the coupling factors for the left and right handed particles, and the masses of the leptons are ignored.

The total probability is the sum of the squares of these amplitudes, i.e. $|M|^2 = |M_\gamma + M_z|^2$. This result contains a pure QED term for the photon exchange, $|M_\gamma|^2$, a pure weak term from the Z^0, $|M_z|^2$, and a $\gamma - Z$ interference term. For unpolarised particles it is also necessary to average over the initial spin states and sum over the final spin states.

For the photon exchange the differential cross-section is:

$$\begin{aligned} \frac{1}{4}\sum_{spins} |M_\gamma|^2 &= \frac{e^4}{4q^4}\left((\not{p}_{e^+} - m_e)\gamma^\lambda(\not{p}_{e^-} + m_e)\gamma^\rho\right)\left((\not{p}_{\mu^+} - m_\mu)\gamma_\lambda(\not{p}_{\mu^-} + m_\mu)\gamma_\rho\right) \\ &= \frac{e^4}{4q^4}(Tr(\not{p}_{e^+}\gamma^\lambda\ \not{p}_{e^-}\gamma^\rho) + m_e Tr(\not{p}_{e^+}\gamma^\lambda\gamma^\rho + \gamma^\lambda\ \not{p}_{e^-}\gamma^\rho) + \\ &\quad m_e^2(\gamma^\lambda\gamma^\rho) + Tr(\not{p}_{\mu^+}\gamma_\lambda\ \not{p}_{\mu^-}\gamma_\rho) + m_\mu Tr(\not{p}_{\mu^+}\gamma_\lambda\gamma_\rho + \gamma_\lambda\ \not{p}_{\mu^-}\gamma_\rho) + \\ &\quad m_\mu^2(\gamma_\lambda\gamma_\rho)) \\ &= \frac{e^4}{4q^4}4(p_{e^+}^\lambda p_{e^-}^\rho + p_{e^+}^\rho p_{e^-}^\lambda + p_{e^+}.p_{e^-}\gamma^\lambda\gamma^\rho - m_e^2\gamma_\lambda\gamma_\rho) \times \\ &\quad 4(p_{\mu^+}^\lambda p_{\mu^-}^\rho + p_{\mu^+}^\rho p_{\mu^-}^\lambda + p_{\mu^+}.p_{\mu^-}\gamma_\lambda\gamma_\rho - m_\mu^2\gamma_\lambda\gamma_\rho) \end{aligned} \tag{3.3}$$

ie.,

$$\begin{aligned} \frac{1}{4}\sum_{spins} |M_\gamma|^2 &= \frac{8e^4}{q^4}((p_{e^+}.p_{\mu^+})(p_{e^-}.p_{\mu^-}) + (p_{e^+}.p_{\mu^-})(p_{e^-}.p_{\mu^+}) + (p_{e^+}.p_{e^-})m_\mu^2 + \\ &\quad (p_{\mu^+}.p_{\mu^-})m_e^2 + m_e^2 m_\mu^2) \end{aligned} \tag{3.4}$$

Since $p \gg m_e, m_\mu$, $p_{e^+}.p_{e^-} = p_{\mu^+}.p_{\mu^-} = 0$, $p_{e^+}.p_{\mu^+} = p_{e^-}.p_{\mu^-} = p^2(1-\cos\theta)$ and $p_{e^+}.p_{\mu^-} = p_{e^-}.p_{\mu^+} = p^2(1+\cos\theta)$, where θ is the angle between the incoming e^- and the outgoing μ^-.

$$\begin{aligned} |M_\gamma|^2 &= \tfrac{8e^4}{q^4}\left(p^4(1-2\cos\theta+\cos^2\theta)+p^4(1+2\cos\theta+\cos^2\theta)\right) \\ &= \tfrac{8e^4}{q^4}2p^4(1+\cos^2\theta) \end{aligned} \tag{3.5}$$

$q^2 = s$, $p^2 = \frac{s}{4}$

$$|M_\gamma|^2 = e^4(1+\cos^2\theta) \tag{3.6}$$

Overall the differential cross-section is given by [39]

$$\begin{aligned} \tfrac{d\sigma}{d\Omega}(\gamma) &= \tfrac{1}{64\pi^2 s}\tfrac{p_f}{p_i}|M_\gamma|^2 \\ &= \tfrac{\alpha^2}{4s}(1+cos^2\theta) \end{aligned} \tag{3.7}$$

where $p_f = p_i$ are the final and initial momenta, α is the fine structure constant $\alpha = \frac{e^2}{4\pi\epsilon_0\hbar c}$.

Similar, but more complicated, calculations can be performed for the interference and the Z^0 terms and the total differential cross-section for the process is:

$$\frac{d\sigma}{d\Omega} = \frac{\alpha^2}{4s}\Big[A_0(1+cos^2\theta)+A_1 cos\theta\Big] \tag{3.8}$$

The terms

$$\begin{aligned} A_0 &= 1+2\Re(r)c_V^2+|r|^2(c_V^2+c_A^2)^2 \\ A_1 &= 0+4\Re(r)c_A^2+8|r|^2c_V^2c_A^2 \end{aligned} \tag{3.9}$$

where $\Re(r)$ is the real part of the Z propagator, modified to include the finite resonance width Γ_Z which must be included when $s \approx m_Z^2$.

$$r = \frac{s}{e^2}\frac{\sqrt{2}Gm_Z^2}{(s-m_Z^2+im_Z\Gamma_Z)} \tag{3.10}$$

In A_0 and A_1 the first part arises from the photon exchange, the second from the $\gamma - Z$ interference and the third accounts for the Z^0 exchange. It can be seen that the Z^0 exchange dominates on the peak. The shape of the Born level cross-section predicted by the ZFITTER [38] program is shown in figure 3.2(a).

3.2 Asymmetry

This cross-section can also be expressed in terms of a forward-backward asymmetry formally defined as:

$$A_{FB} \equiv \frac{\sigma_F - \sigma_B}{\sigma_F + \sigma_B} \tag{3.11}$$

where

$$\sigma_F = \int_0^{+1} d\cos\theta \frac{d\sigma}{d\cos\theta} \qquad \sigma_B = \int_{-1}^{0} d\cos\theta \frac{d\sigma}{d\cos\theta} \tag{3.12}$$

$$\int d\cos\theta \frac{d\sigma}{d\cos\theta} = A_0(\cos\theta + \frac{\cos^3\theta}{3}) + A_1\frac{\cos^2\theta}{2} \tag{3.13}$$

Thus,

$$\sigma_F = \frac{4}{3}A_0 + \frac{1}{2}A_1 \qquad \sigma_B = \frac{4}{3}A_0 - \frac{1}{2}A_1 \tag{3.14}$$

Hence,

$$A_{FB} = \frac{3}{8}\frac{A_1}{A_0} \tag{3.15}$$

and so

$$\begin{aligned} A_{FB} &= \tfrac{3}{2}c_A^2\Re(r) \quad (s \neq m_Z^2) \\ A_{FB} &= 3\tfrac{c_V^2 c_A^2}{(c_V^2+c_A^2)^2} \quad (s \approx m_Z^2) \end{aligned} \tag{3.16}$$

The shape of the Born level asymmetry predicted by ZFITTER is shown in figure 3.2(b).

3.3 Electroweak corrections

There are many corrections which have to be applied to the zeroth order diagrams shown above. These corrections can be split into several categories:

- QED photonic corrections:

  These arise from the addition of an extra photon, such as initial state radiation, to the Born level diagrams shown in figure 3.1. Examples of this are shown in

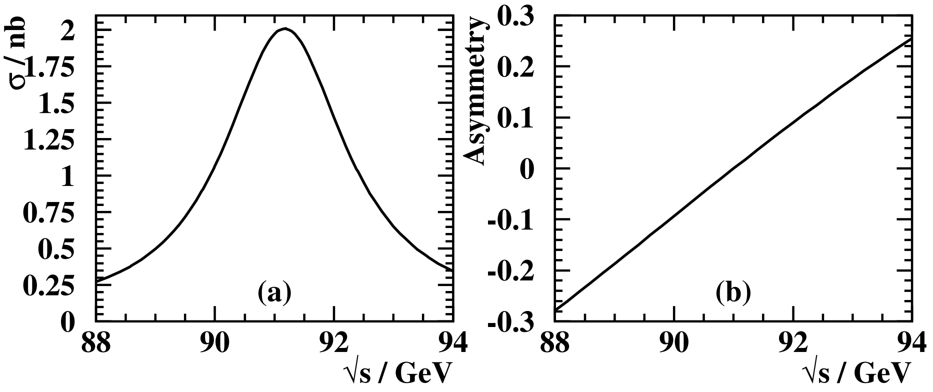

Figure 3.2: The ZFITTER predicted Born level

a) cross-section

b) asymmetry

for the reaction $e^+e^- \to \mu^+\mu^-$.

figure 3.3. The emission of an initial state photon lowers the collision energy; for example at energies above the Z^0 there is a large cross-section for reactions where the initial-state radiation lowers the collision energy to that of the Z mass. This is known as "radiative return". The actual collision energy is labelled $\sqrt{s'}$ GeV.

- Weak corrections:
  These include internal loop diagrams which provide corrections to the boson, or at the vertex, or box diagrams where two massive bosons are exchanged, diagrams of these are shown in figure 3.4.

The cross-section as a function of $\sqrt{s}$ is shown in figure 3.5. The zeroth order Born level prediction is shown as the dashed line, near the Z peak this cross-section has a Breit-Wigner form. The final prediction, after correcting for effect of higher order effects, is shown as the solid line. These corrections shift the peak maximum to slightly higher energy, broaden the peak and, because of the radiative return, the peak is no longer symmetric.

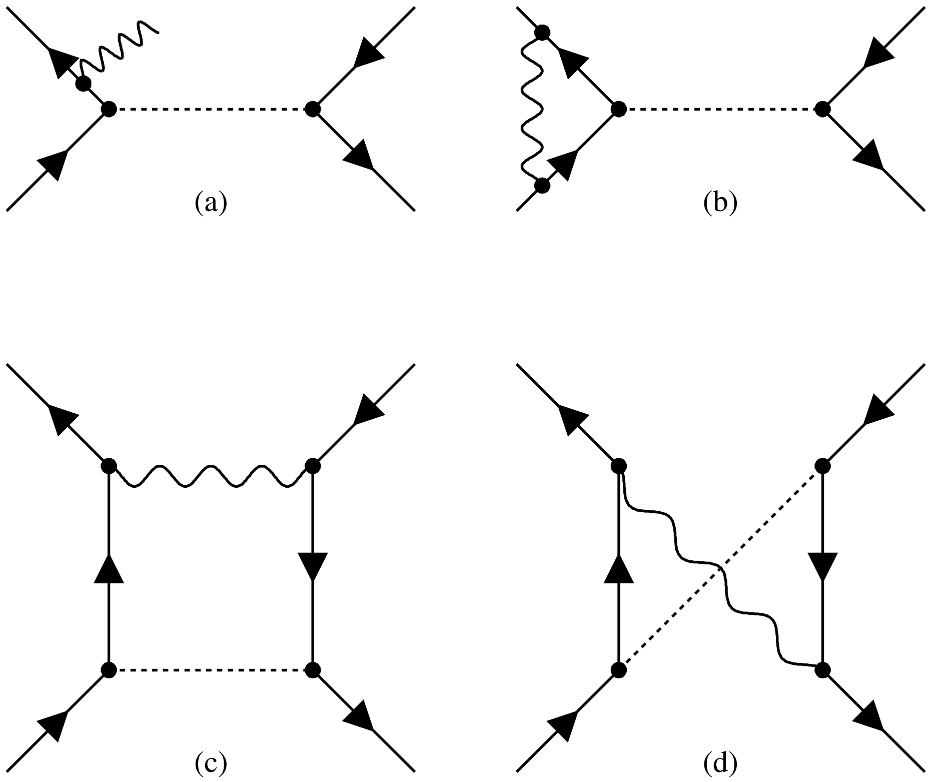

Figure 3.3: Feynman diagrams showing possible photonic corrections to the reaction $e^+e^- \rightarrow \mu^+\mu^-$. The dashed line can be either a Z^0 or γ, the wavy line is the extra photon.

(a) Shows initial state radiation. The extra photon can be emitted from any of the four fermion lines.

(b) The extra photon can be emitted and absorbed by either the incoming (shown) or outgoing fermion pair.

(c) The extra photon can be emitted and absorbed by either the anti-particles (as shown) or the particles.

(d) The extra photon can be emitted and absorbed by the other pair of fermions.

Combinations of (a), (b) and (c) or (d) also need correcting for.

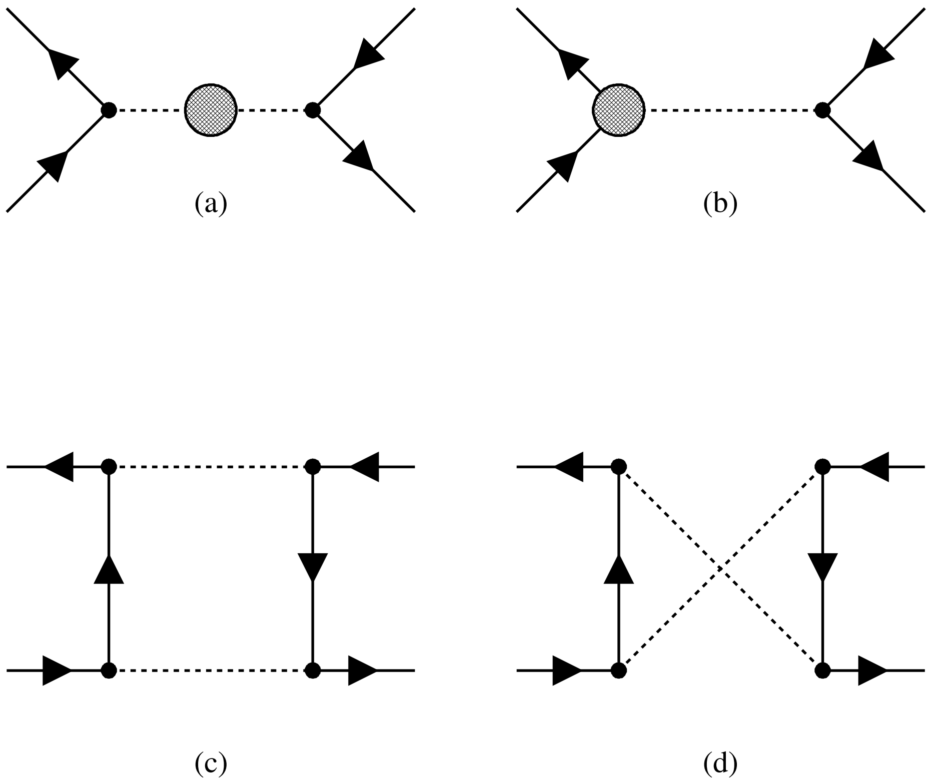

Figure 3.4: Feynman diagrams showing possible weak corrections to the reaction $e^+e^- \rightarrow \mu^+\mu^-$.

(a) Propagator correction.

(b) Vertex correction, the correction can be at any vertex

In these diagrams the dashed lines can be either a Z^0 or γ.

(c)+(d) Box contributions.

Here the dashed lines can either both be Z^0 or W.

The asymmetry as a function of s is shown in figure 3.6. The Born level prediction is shown as the dashed line, the final prediction after correcting for higher order effects is shown as the solid line.

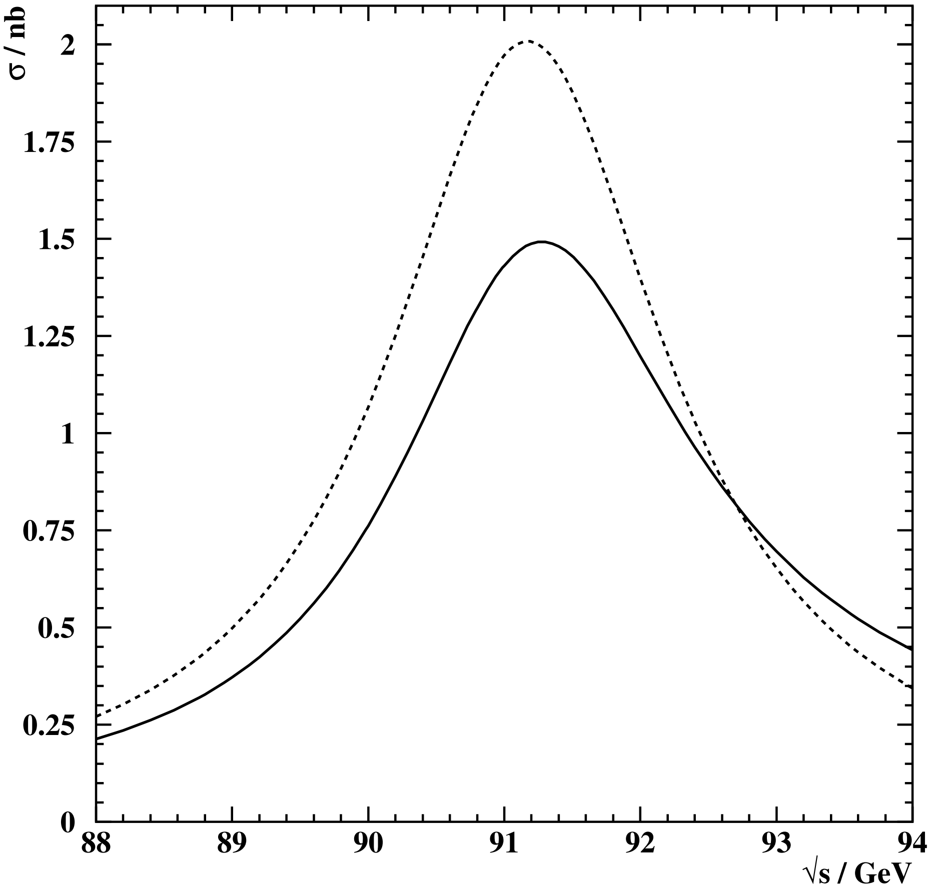

Figure 3.5: The predicted cross-section for $e^+e^- \to \mu^+\mu^-$ (solid line) obtained using the ZFITTER program. For comparison the predicted Born level cross-section (dashed line) is also shown.

3.4 Applications

The measurement of the μ and τ pair cross-section, angular distribution, asymmetry and s$'$ distribution have many applications. Apart from testing the Standard Model these measurements can be used as data for fits to the running of α_{em}, 4-fermion

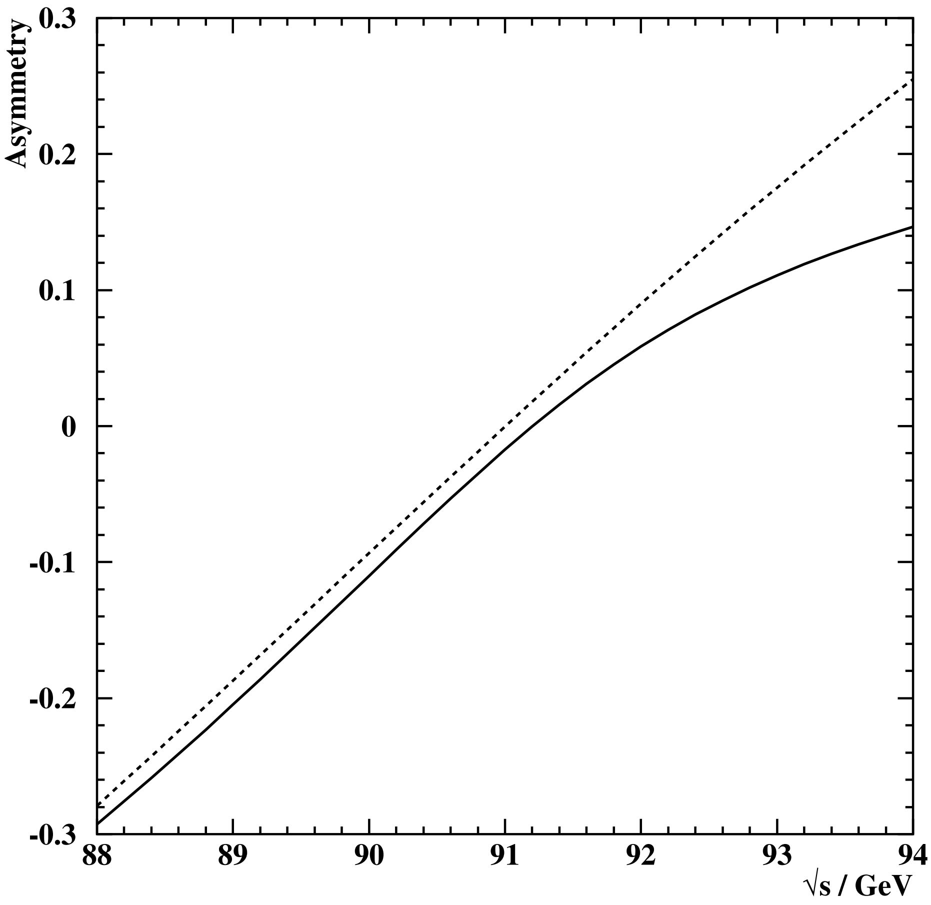

Figure 3.6: The predicted asymmetry for $e^+e^- \to \mu^+\mu^-$ (solid line) obtained using the ZFITTER program. For comparison the predicted Born level asymmetry (dashed line) is also shown.

contact interaction limits, or setting limits on the masses of many new particles, eg. R-parity violating $\tilde{\nu}$.

Contact interactions are processes where the energy scale of the interaction is so high that the mediating particle cannot be resolved (see figure 3.7(a)).

Searches for R-parity violating $\tilde{\nu}$s are searches for processes of the form given in figure 3.7(b). In this process the mediating particle is the supersymmetric partner of the ν_τ. Standard Model particles have an R-parity of 1, whereas supersymmetric have an R-parity of -1, in the reaction shown the R-parity of the initial and final states is $1 \times 1 = 1$, whereas the R-parity of the mediating particle is -1 and so in this process R-parity is violated Such a particle can show up as a resonance in the $\sqrt{s'}$ distribution centred at the mass of the mediating particle.

The limits on the 4-fermion contact interaction and the mass of the R-parity violating $\tilde{\nu}$ using this results in this thesis are given in [42, 43].

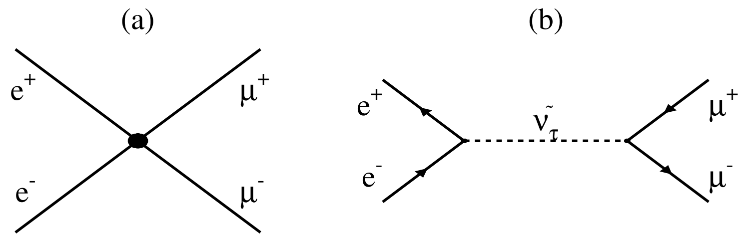

Figure 3.7: Feynman diagrams showing:

a) a 4-fermion contact interaction.

b) s-channel exchange of an R-parity violating $\tilde{\nu}$

In addition the distribution of the μ pair events that have radiatively returned to the Z^0 peak can be used to calculate the actual beam energy at LEP. The rest of this thesis describes the selection and measurement of cross-section, angular distribution and asymmetry for the μ and τ pair events. Some of the applications from the μ and τ pair measurement at energies above the Z mass are also described.

Chapter 4

Preliminary Details of the Analyses

The following analyses are an evolution of those published in [40, 41, 42, 43, 44]. For simplicity, the improved selection, developed during these measurements over the last three years, have been applied to the μ and τ pair analysis at all the high energy data.

4.1 Lepton Pair Preselection

Only a fraction of the events reconstructed by the OPAL detector are relevant for the analyses of lepton pairs. Those events which are not relevant in these analyses are kept to a minimum by performing a preselection. An event is preselected if any of the following conditions are satisfied[1]:

- The event contains a track with the following properties:
  - ≥ 20 hits in the central tracking chambers.
  - $p_t > 0.7$ for data taken before 1998. p_t is the transverse component of the track momentum.
  - $p_t > 0.0165 E_{beam}$ for data taken in 1998[2].
  - $|d_0| < 1$ cm

[1] This preselection forms part of the general OPAL event selection.

[2] This change reduces the amount of non-physics data that is recorded and will be applied to all the data taken at $\sqrt{\mathrm{s}} > M_Z$

– $|z_0| < 50$ cm [3]

These requirements mean the track is well reconstructed with high momentum and originated close to the interaction point at the centre of the detector.

- It contains a track in the muon endcap (ME) detector that originated within 20 cm of the interaction point when projected back to the centre of the detector, providing there are no more than 4 ME tracks.

- For data taken before 1998 it contains a large transverse component of energy, $E_t > 6$ GeV, in at least two electromagnetic clusters, or provided the two clusters are back-to-back to within 25° only $E_t > 2$ GeV has to be deposited in one of the clusters. For data taken during 1998 this requirement was changed to $E_t > 0.15E_{beam}$ in both cases to reduce the amount of non-physics data recorded.

The first selection will detect all types of event; the second and third, respectively, provide a central detector independent selection for detecting endcap muons, and electrons and taus.

Some of the events passing this preselection are quark/anti-quark pairs (known as multihadronic events). For this analysis most of these events are vetoed by applying a loose low multiplicity requirement where the sum of the number of tracks and number of clusters in the event must be below 18. The level of this number is relatively high as the number of track/clusters in the event can be increased due to processes such as final-state photon emission[4] or from split tracks[5].

4.2 Cosmic Ray Rejection

A high number of cosmic rays pass through the OPAL detector, and some of these events pass the above preselection. The majority of these are removed using infor-

[3] d_0 and z_0 are defined on page 20.

[4] Final-state photons can convert into into a pair of charged particles and so increases the number of tracks in the events by two per conversion.

[5] A split track can occur when the charged particle passes close to the cathode plane of the CJ subdetector and as any hits in this region are rejected the original track may be reconstructed as a pair of tracks, thereby increasing the number of tracks in the event by one per split track.

mation from the TOF counters if the event lies in the barrel region, $|\cos\theta| < 0.8$, or by estimating how well the tracks match to the nominal interaction point if the event lies in the endcap region.

The cosmic ray rejection for the muon pair analysis is described below.

A barrel event must either:

- Have a consistent TOF measurement.

  For cosmic rays travelling downwards it is expected that the TOF counter below the level of the beampipe will measure a later time than the counter above the level of the beampipe. So Δt, defined as the time measured by the lower counter minus the time measured by the upper counter must be small.

  Figure 4.1(a), shows the time difference, Δt, between pairs of back-to-back TOF counters for the 184 GeV data. There is a reasonable separation between the signal events ($-10 < \Delta t < 10$ ns) and cosmic ray events (the peak of events with $10 < \Delta t < 30$ ns). There are few events close to this cut indicated by the arrow showing that this cut is relatively insensitive to the positioning of the cut. Figure 4.1(b) shows the measured time, t_0, corrected for the flight time of a $\beta = 1$ particle from the interaction point for the events passing $|\Delta t| < 10$ ns, and figure 4.1(c) shows the t_0 distribution for events which do not have a pair of back-to-back TOF counters.

  Again there is no evidence for a large cosmic ray contamination.

  Or,

- Pass a tight vertex cut, $\Sigma|d_0| < 0.08$ cm and $\Sigma z_0 < 10$ cm implying the tracks originate very close to the nominal interaction point.

  Figure 4.2(a) shows the $\Sigma|d_0|$ versus Σz_0 distribution for events taken at 184 GeV which are identified as cosmics by the TOF cuts. As expected these events are evenly distributed over the plot. Few events are recovered by the tight vertex cut indicated by the dashed line.

  Figures 4.2(b) and (c) show events which were accepted as good by the TOF cuts with back-to-back TOF counters and with only one TOF counter, respec-

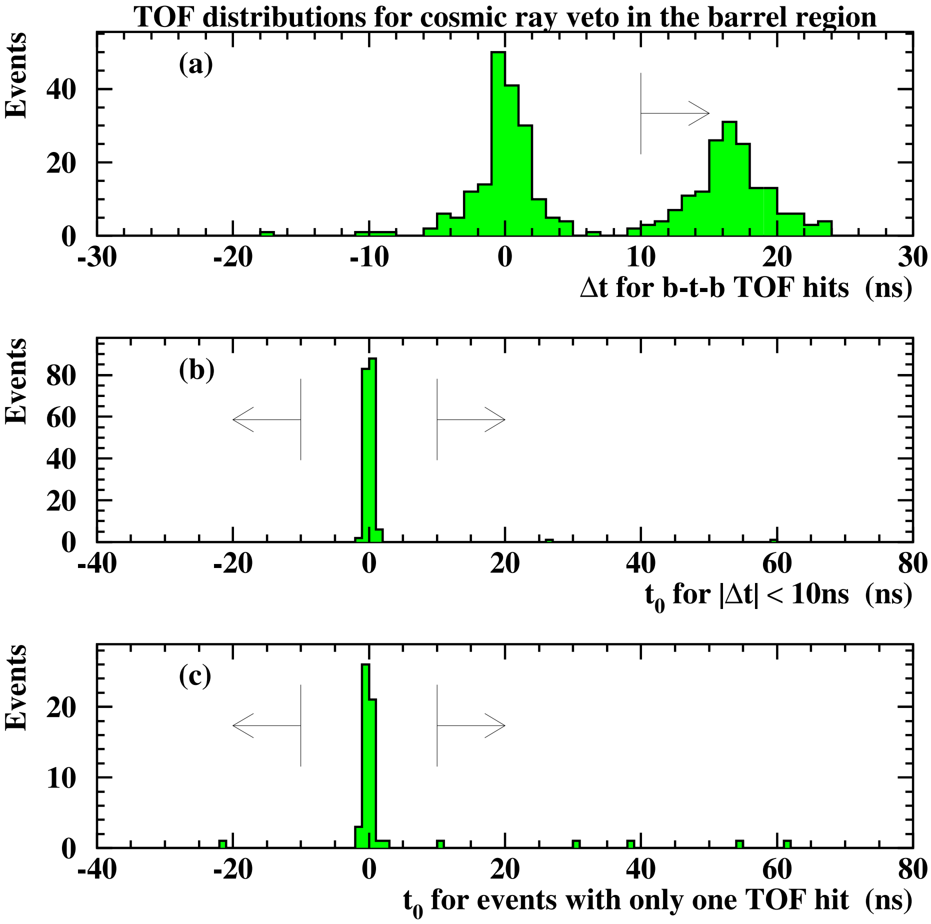

Figure 4.1: For the 184 GeV data:

(a) Time difference (Δt) between pairs of back-to-back TOF counters.

(b) The measured time, t_0, (corrected for flight time) for events passing the Δt cut.

(c) The measured time t_0 for events with a single TOF counter hit.

tively. In these plots the events are clustered close to the interaction point and any cosmic ray contamination is clearly small.

As the position resolution in the endcaps is significantly poorer than in the barrel an endcap event is required to pass the looser vertex requirement of $\Sigma|d_0| < 0.6$ cm and $\Sigma z_0 < 50$ cm. Figure 4.2(d) shows $\Sigma|d_0|$ versus Σz_0 for these events. There is a cluster of events close to the interaction point with a small number of events spread throughout the region. There are only a few events close to the vertex cut indicating a relatively low cosmic ray background.

From these plots it can be seen that the cuts used to reject the cosmic ray background in the muon pairs do so very cleanly. The number of possible misidentified cosmic events remaining, determined by the number of events lying close the the cuts, is applied as a systematic error to the cross-section..

Cosmic rejection for the tau pairs is similar except that in the endcaps the vertex requirement is $\Sigma|d_0| < 1.5$ cm and $\Sigma z_0 < 50$ cm. In addition all events must originate close to the interaction point by requiring the d_0 of the track with the smallest d_0 to be less than 0.5 cm and the average of the unconstrained signed z_0 of all the tracks must be less than 20 cm.

4.3 Monte Carlo simulation

The different processes that arise from Z^0 decaying to quarks, charged leptons and other physics processes that may be misidentified as lepton pairs are modelled by separate Monte Carlo samples. A high statistics sample (at least 100 times the number of events obtained in data) of μ and τ pairs are used to determine the efficiency for selecting events. The background, from types of events other than those wanted, that pass selection cuts is determined by applying the selection to Monte Carlo samples modelling multihadronic and Bhabha decays of the Z^0 (as well as using the Monte Carlo for the other lepton pair process), two-photon $e^+e^-f\bar{f}$ processes (figure 4.3(a)), $We\nu_e$ process (figure 4.3(b)), other four-fermion processes such as ZZ production (figure 4.3(c)), t-channel W^+W^- production (figure 4.3(d)) t-channel $(Z/\gamma)^*e^+e^-$ (figure 4.3(e)) or a general four-fermion process (figure 4.3(f)). The

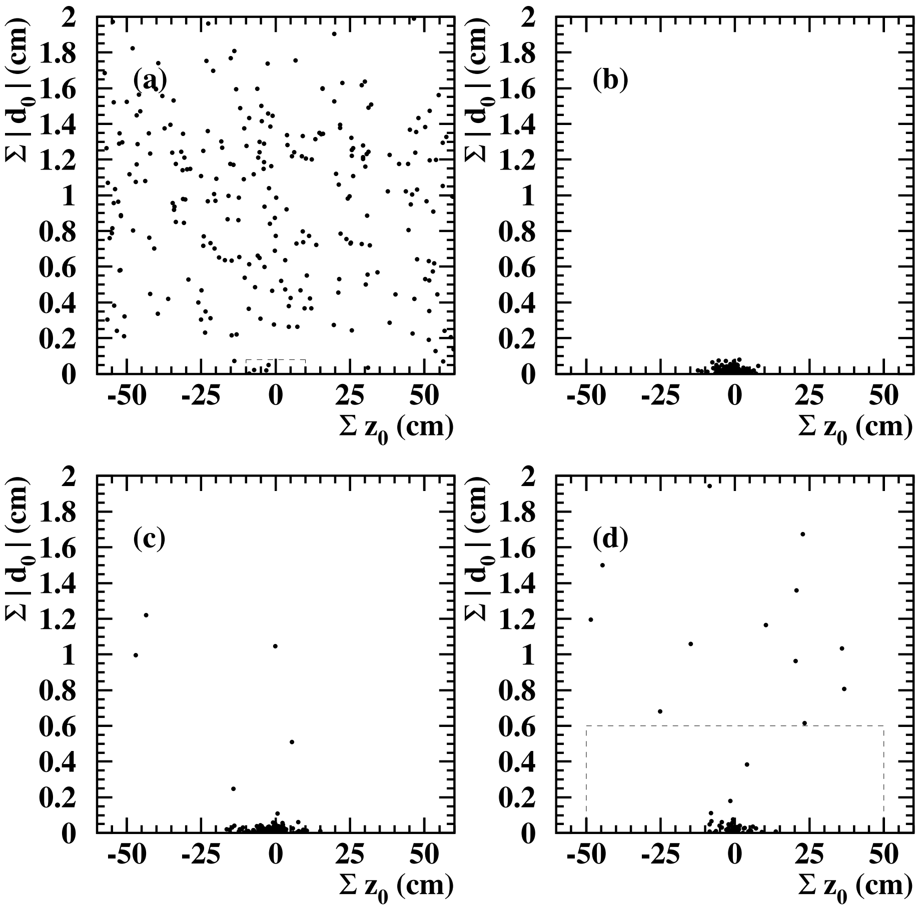

Figure 4.2: For the 184 GeV data:

$\Sigma|d_0|$ versus Σz_0 for:

(a) barrel events which fail the TOF cuts.

(b) barrel events with back-to-back TOF counters which pass the TOF cuts.

(c) barrel events with a single TOF counter hit which pass the TOF cuts.

(d) endcap events.

combination of Monte Carlo samples used in these analyses are given in table 4.1.

<table>
<tr><th colspan="2" rowspan="2">Monte Carlo</th><th colspan="5">$\sqrt{s}$</th></tr>
<tr><th>133</th><th>161</th><th>171</th><th>184</th><th>189</th></tr>
<tr><td rowspan="4">2-fermion</td><td>$q\bar{q}$</td><td colspan="5">PYTHIA [45]</td></tr>
<tr><td>e^+e^-</td><td colspan="5">BHWIDE [46]</td></tr>
<tr><td>$\mu^+\mu^-$</td><td colspan="5" rowspan="2">KORALZ</td></tr>
<tr><td>$\tau^+\tau^-$</td></tr>
<tr><td rowspan="3">2γ</td><td>$e^+e^-q\bar{q}$(tagged)</td><td>HERWIG</td><td colspan="2">PYTHIA</td><td colspan="2">HERWIG [47]</td></tr>
<tr><td>$e^+e^-q\bar{q}$(untagged)</td><td>PYTHIA</td><td colspan="4">PHOJET [48]</td></tr>
<tr><td>$e^+e^-l^+l^-$</td><td colspan="5">VERMASEREN [49]</td></tr>
<tr><td rowspan="5">4-fermion</td><td>$f\bar{f}f'\bar{f}'$</td><td colspan="3">EXCALIBUR [50]</td><td colspan="2" rowspan="5">GRACE4F</td></tr>
<tr><td>$e^+e^-f\bar{f}$</td><td colspan="3">FERMISV</td></tr>
<tr><td>$We\nu_e$</td><td colspan="3">PYTHIA</td></tr>
<tr><td>$(Z/\gamma)^*e^+e^-$</td><td colspan="3">GRACE4F</td></tr>
<tr><td>$(Z/\gamma)^*e^+e^- \rightarrow e^+e^-e^+e^-$</td><td colspan="3">PYTHIA</td></tr>
</table>

Table 4.1: The generators used to produce the Monte Carlo samples at each energy.

As the Monte Carlo samples are generated at a slightly different energy, E_{MC}, from the final official LEP beam energy, E_{CM}, the cross-sections are scaled by a factor of

$$(E_{MC})^2/(E_{CM})^2 \tag{4.1}$$

This scale factor is typically less than 1.5%, however where the same set of Monte Carlo samples generated at energies between 130 and 136 GeV is used for the analyses of these energies the scaling factor reaches 10%. For simplicity equation 4.1 is used to scale all Monte Carlo samples. This is a reasonable assumption as most of the events passing the selections are either from two fermion processes, and hence have a cross-section proportional to $\frac{1}{s}$, or from $\gamma\gamma$ or γZ processes, which have a "flat" cross-section for all values s. The scale factor would not be sensible to apply to events coming from W^+W^- or ZZ production where the cross-section increases sharply above the production threshold of 161 and 182 GeV, however very few events

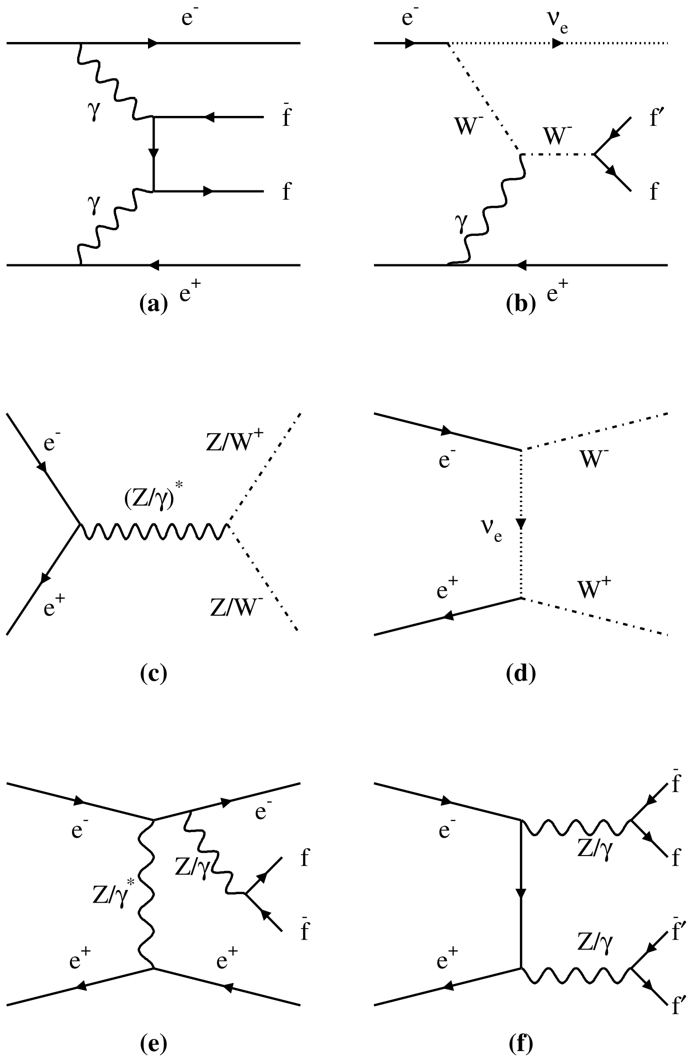

Figure 4.3: Feynman diagram showing the Monte Carlo processes of:

a) Two photon $e^+e^-f\bar{f}$.

b) $We\nu_e$.

c) s-channel W or Z pair production.

d) t-channel W pair production.

e) $(Z/\gamma)^*e^+e^-$

f) General 4 fermion production.

of this type are selected. In all cases the error caused by applying the scaling factors is taken into account in the systematic error.

4.4 Determining the Centre of Mass Energy of the Collision

Collisions at energies above the Z^0 energy have a tendency to 'radiatively return' to the Z^0 peak by the emission of an initial state photon. This emitted photon reduces the effective centre-of-mass energy, $\sqrt{\mathrm{s}'}$, of the subsequent e^+e^- collision. Hence the data are divided into two samples, the first containing the non-radiative events at high or full energy, selected by making an $\mathrm{s}'/\mathrm{s} > 0.7225$ cut[6], and the second being an inclusive selection containing all events satisfying $\mathrm{s}'/\mathrm{s} > 0.01$.

The $\sqrt{\mathrm{s}'}$ of the e^+e^- collision was estimated using the polar angles, θ_1 and θ_2, of the two lepton candidates relative to the beam direction. For the μ pairs the $\cos\theta$ of tracks in the barrel region are determined using the hits in the central tracking chambers. In the endcap region the $\cos\theta$ is determined from the ME subdetector. For the τ pairs, the $\cos\theta$ of each τ is determined from the summed vector track momentum and vector ECAL cluster energy of each cone (see section 6.1.1).

The energy of a possible undetected initial state photon along the beam direction, E_γ, was estimated assuming massless three-body kinematics as:

$$E_\gamma = \sqrt{s}\frac{|\sin(\theta_1+\theta_2)|}{|\sin(\theta_1+\theta_2)| + \sin\theta_1 + \sin\theta_2}, \tag{4.2}$$

and thus the effective centre-of-mass energy is calculated from:

$$\sqrt{\mathrm{s}'} = \sqrt{s - 2E_\gamma\sqrt{s}}. \tag{4.3}$$

The actual $\sqrt{\mathrm{s}'}$ is compared to the reconstructed $\sqrt{\mathrm{s}'}$ for the 184 GeV τ pair Monte Carlo sample in Figure 4.4. There is a strong correlation between these quantities, but the reconstructed $\sqrt{\mathrm{s}'}$ is too high in some events. These events

[6]The position of this cut was decided by the LEP Electroweak working group. All four LEP experiments use this cut, which will make future combined LEP results easier to calculate.

mainly occur when two initial state photons are emitted, one from the electron and one from the positron, resulting in a more back-to-back event than would occur for a single emitted photon and hence a higher $\sqrt{s'}$ is reconstructed. These are known as 'feedthrough' events. In other cases the reconstructed $\sqrt{s'}$ is too low which happens when either of the lepton candidates emits a photon, called a final state photon. This changes the momentum and direction of the lepton candidate and results in the event being less back-to-back than immediately after the collision. The emission of a final-state photon can also result in the reconstructed $\sqrt{s'}$ being too high.

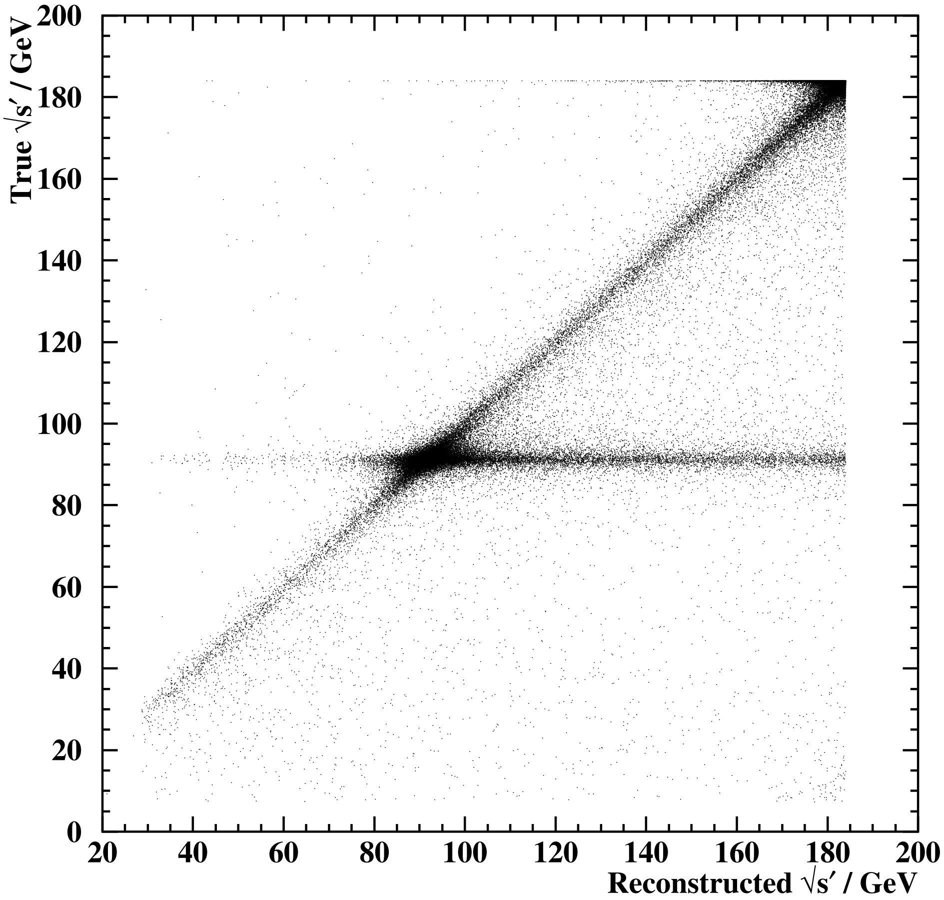

Figure 4.4: True $\sqrt{s'}$ against reconstructed $\sqrt{s'}$ for the 184 GeV τ pair Monte Carlo sample.

4.5 Efficiency

The efficiency is defined as the number of selected signal events divided by the number of generated signal events. Both the selected and generated signal events have to have a generated $s'/s > 0.7225$ for the non-radiative selection.

4.5.1 Correction to efficiency due to 4-fermion events

There are small corrections to this efficiency from four-fermion effects. Consider the four fermion process of the type $\mu^+\mu^- f\bar{f}$, where $f\bar{f}$ is any fermion pair.

If this event comes from an s-channel process (such as that shown in figure 3.3(a) where the initial-state photon converts into a fermion pair), then this event is consistent with being a signal event and should therefore be taken into account when determining the efficiency. However, if this event arises from any of the processes shown in figure 4.3 (with the exception of figure 4.3(f) which, in certain instances, can be redrawn as the s-channel process) the physics is completely different from that of signal events.

For a 4-fermion event to be classified as a signal event, all the following kinematic requirements have to be satisfied:

1. $m_{\mu^+\mu^-} > m_{f\bar{f}}$
2. $m_{f\bar{f}} < 70$ GeV
3. $\frac{m^2_{\mu^+\mu^-}}{s} > 0.7225$ for non-radiative selection, or
   $\frac{m^2_{\mu^+\mu^-}}{s} > 0.01$ for the inclusive selection.

The third kinematic requirement merely means the μ pair has to satisfy the s'/s cut. The four possible combinations of Z and γ in figure 4.3(f) producing an s-channel event are considered below. In all cases the first Z/γ decays to $\mu^+\mu^-$ and the second decays to $f\bar{f}$.

- $ZZ \to \mu^+\mu^- f\bar{f}$.

In this case the process is mediated by two heavy vector bosons and, like a W pair event, is background. This intuitive classification is fulfilled by the second kinematic requirement given above.

- $Z\gamma \rightarrow \mu^+\mu^- f\bar{f}$

  The first kinematic requirement naturally classifies these types of event as signal. The process is equivalent to the initial/final-state conversion mentioned above.

- $\gamma Z \rightarrow \mu^+\mu^- f\bar{f}$

  This case is similar to that above, but is classified as background from the first kinematic requirement. It is a signal for the process $e^+e^- \rightarrow f\bar{f}$.

- $\gamma\gamma \rightarrow \mu^+\mu^- f\bar{f}$

  This process can obviously be classified as signal or background depending on the nature of the event and the first kinematic requirement classifies the event sensibly.

Although this method of classifying signal and background 4-fermion events has been applied to all $\sqrt{\mathrm{s}}$ energies, some of these classifications may only be valid for $\sqrt{\mathrm{s}}$ below the ZZ production threshold. Further study would be needed to determine whether the classifications need altering for the highest energy data.

4.6 Feedthrough and Background

The feedthrough background for the non-radiative selection is the number of Monte Carlo events that incorrectly pass the selection as they have a generated $\mathrm{s}'/\mathrm{s} < 0.7225$. Clearly the background arising from other physics processes is the number of background events that pass the selection.

Both of these background quantities are calculated in terms of a visible cross-section defined as:

$$\sigma_{\mathrm{Background}} = \frac{\mathrm{N}_{\mathrm{passing}}}{\mathrm{N}_{\mathrm{generated}}}\sigma_{\mathrm{generated}}$$

4.7 Initial/Final-state Radiation Interference

The existence of interference between initial- and final-state radiation causes several problems for the analyses of the μ and τ pair cross-section, angular distribution and asymmetry measurements.

The interference causes an ambiguity in the definition of $\sqrt{s'}$ which is defined as the centre-of-mass energy of the e^+e^- system after initial-state radiation. In addition the Monte Carlo generators used to determine the efficiencies, backgrounds and acceptances do not include this interference. Therefore the use of the Monte Carlo predictions is only valid if corrections are applied so that the data and Monte Carlo have a consistent treatment of the interference.

In the following cross-section, angular distribution and asymmetry measurements, this necessary correction is applied to the data such that the effects of the interference are removed and the measurements are compared to theoretical predictions where the interference has also been removed. This method also has the the advantage of making the $\sqrt{s'}$ definition unambiguous.

The interference contribution in the data is calculated from the predictions of the ZFITTER program which has the option of enabling or disabling this interference when calculating its predictions.

First a differential "interference cross-section", $(\frac{d^2\sigma_{\mathrm{IFSR}}}{dm_{ll}\, d\cos\theta})$ is calculated. This is a function of the mass of the lepton pair, m_{ll}, and the angle, θ, between the incoming electron and the outgoing lepton. It is defined as the difference between the predicted ZFITTER differential cross-sections including $(\frac{d^2\sigma_{\mathrm{int}}}{dm_{ll}\, d\cos\theta})$ and excluding $(\frac{d^2\sigma_{\mathrm{noint}}}{dm_{ll}\, d\cos\theta})$ interference. The $(\cos\theta, m_{ll})$ plane is divided into twenty equal m_{ll} bins and 12 $\cos\theta$ bins.

The fraction of this cross-section passing the selection cuts is deduced by assuming the selection efficiency

$$\epsilon_{IFSR}(\cos\theta, m_{ll}) = \epsilon_{noint}(\cos\theta, m_{ll}) \tag{4.4}$$

where ϵ_{noint} in each bin is determined from the Monte Carlo events for both s'/s samples. It is defined as the number of events in the bin passing the s'/s selection (with a generated m_{ll} and reconstructed $\cos\theta$); divided by the total number of generated events in the bin (with a generated m_{ll} and generated $\cos\theta$).

From this the accepted interference cross-section, which can be negative or positive depending on the angle, θ, is estimated as a function of $\cos\theta$ enabling it to be applied easily to the total cross-sections, angular distributions and asymmetry measurements.

The error on this procedure was determined by using a different estimate for the efficiency, ϵ_{IFSR}, described below.

Consider the case where $m_{ll} \approx \sqrt{\mathrm{s}}$. In these events there is very little initial-state radiation, hence the efficiency for selecting these events can be assumed to equate to the efficiency for selecting final-state radiation events. Similarly, those events with $m_{ll} \approx M_Z$ are dominated by initial-state radiation. From the selection efficiencies given in the next chapters it can be seen that the final-state radiation efficiency ($\simeq$ efficiency for $\mathrm{s}'/\mathrm{s} > 0.7225$) is greater than that for initial-state radiation ($\simeq$ efficiency for $\mathrm{s}'/\mathrm{s} > 0.01$).

Events with $m_{ll} < \sqrt{\mathrm{s}}$ contain a mixture of the lower selection efficiency initial-state radiation and higher selection efficiency final-state radiation.

So for events with large m_{ll} (dominated by final-state radiation) the original efficiency estimate, ϵ_{noint}, is a good approximation to the true efficiency ϵ_{IFSR}. Events with small m_{ll} will normally arise from initial-state radiation and so the estimated efficiency may be a good approximation. However, in rare cases, small m_{ll} may arise from final-state radiation. In this case the actual efficiency may be higher than the estimated efficiency and so might be underestimated. To allow for this the error on ϵ_{IFSR} is taken as half the difference between the predicted efficiency of the bin, $\epsilon_{noint}(\cos\theta, m_{ll})$ and the maximum efficiency for the $\cos\theta$ range, $\epsilon_{noint}(\cos\theta, \sqrt{\mathrm{s}})$, so the new estimated efficiency is given by

$$\epsilon_{IFSR}(\cos\theta, m_{ll}) = \frac{\epsilon_{noint}(\cos\theta, m_{ll}) + \epsilon_{noint}(\cos\theta, \sqrt{\mathrm{s}})}{2} \tag{4.5}$$

The results of the interference correction were checked by using an independent estimate using the KORALZ Monte Carlo generator. Normally this generator is allowed to generate multiple photons and interference between initial- and final-state radiation is not included. However, if only a single photon is allowed to be emitted then interference can either be enabled or disabled. For both cases a sample of μ pairs was generated at 171 GeV, and the differences between the observed cross-sections, angular distributions and asymmetries were compared with the ZFITTER estimates. Figure 4.5 shows the comparison of the angular distributions. The two predictions are in good agreement. In all bins only the statistical error is considered and over half of the bins differ by less than one standard deviation. Of the remainder all but one agree to within two standard deviations.

Overall the interference correction is small, and as it is calculated at the detector level, it is applied before the corrections for efficiency. The corrections to the cross-sections and asymmetries for the 172 GeV results are shown in table 4.2, similar corrections are obtained for each of the centre-of-mass energies. Note the interference correction for the combined inclusive asymmetry is larger than for the individual μ and τ pair asymmetries; this will be discussed in a later chapter.

	s′/s > 0.01	s′/s > 0.7225
$\delta\sigma/\sigma_{SM}(\mu\mu)(\%)$	-0.42 ± 0.05	-1.5 ± 0.4
$\delta\sigma/\sigma_{SM}(\tau\tau)(\%)$	-0.44 ± 0.06	-1.2 ± 0.3
$\delta A_{FB}(\mu\mu)$	-0.0058 ± 0.0008	-0.017 ± 0.005
$\delta A_{FB}(\tau\tau)$	-0.0061 ± 0.0010	-0.015 ± 0.004
$\delta A_{FB}(combined)$	-0.0064 ± 0.0009	-0.017 ± 0.005

Table 4.2: The corrections, $\Delta\sigma$ and ΔA_{FB}, which have to be applied to the measured 172 GeV cross-sections and asymmetries in order to remove the contribution from the interference between the initial- and final-state radiation. The correction to the cross-sections are expressed as a percentage of the expected Standard Model cross-section. The corrections to the asymmetries are absolute numbers. The error is the uncertainty arising from the modelling of the selection efficiency for the interference cross-section discussed earlier in this section.

4.8 Luminosity

The integrated data luminosity is determined using information from the SW and FD subdetectors. These subdetectors both measure the luminosity by counting the number of Bhabha scattered electrons into the precisely known detector acceptance.

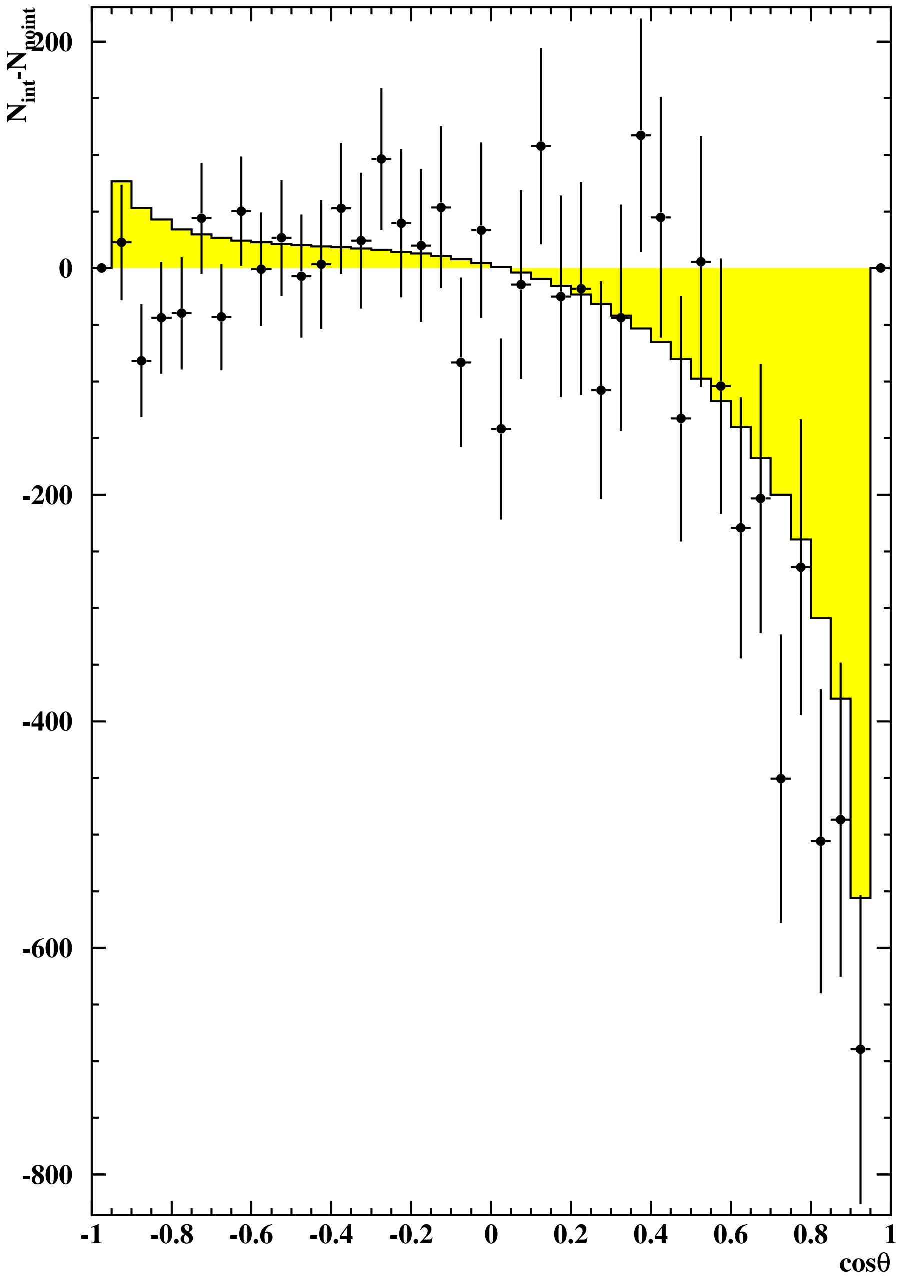

Figure 4.5: The comparison between the ZFITTER and KORALZ predictions for the $\cos\theta$ dependence of initial and final state radiation interference cross-section. The distributions show the predicted number of events without interference minus the predicted number with interference in 40 equal bins of $\cos\theta$.

The histogram represents the ZFITTER prediction, the points are the KORALZ prediction, the error bars are statistical.

This process has a cross-section varying as $\approx \frac{1}{\theta^3}$, where θ is the angle between the incoming and scattered electron and can be calculated to a high degree of precision (0.25%). Any analysis of the data will be more reliant on certain subdetectors than others and so each subdetector classifies its operating status according to the convention shown in table 4.3.

Status	Meaning
0	Status unknown
1	Detector not on
2	Detector partially on (low voltage or readout problems) m
3	All seems OK

Table 4.3: The classification convention for the status of each subdetector.

The integrated luminosities from SW and FD subdetectors can be split into three mutually exclusive categories depending on their status:

1. SW status = 3 and FD status $\neq$ 3.
2. SW status = 3 and FD status = 3.
3. SW status $\neq$ 3 and FD status = 3.

If both luminosity measuring subdetectors have bad status, the data are rejected.

The analyses described in this thesis have the additional subdetector and triggering requirements given in table 4.4. As the status requirements for each analysis are very similar the integrated luminosity obtained from the generally tighter τ pair analysis status requirements was used in both analyses. The difference on the integrated luminosity due to the status requirements was checked and found to be negligible compared to the overall error on the luminosity.

The integrated data luminosity taken at each energy used for the analysis of the μ and τ pairs was obtained from the sum of the SW luminosity in category 1 and the FD luminosity in category 3. The exception to this was for the 1995 LEP1.5 data taking when acceptance of the SW luminometer was artificially reduced at the trigger level to prevent the subdetector readout electronics being overloaded due to

Subdetector	Minimum status μ pair	Minimum status τ pair
CV	2	2
CJ	2	2
CJ Trigger	2	2
TB	2	3
TB Trigger	2	3
EB	3	3
EB Trigger	0	2
EE	3	3
EE Trigger	0	3
ME Trigger	2	0
Other	0	0

Table 4.4: The subdetector status required for the μ and τ pair analyses.

a severe synchrotron radiation problem[7]. For these runs the luminosity was obtained using a more complicated procedure using the sum of:

1. The average of the SW and FD luminosities in category 2.
2. The difference in the SW luminosities in categories 1 and 2.
3. The FD luminosity in category 3.

The luminosity weighted mean beam energy and the integrated data luminosities for the energies measured are given in table 4.5. The systematic error on the luminosity is the combined uncertainties arising from the theoretical calculation (0.25%), experimental effects ($\approx$ 0.30% and the beam energy ($<$ 0.1%). The data taken in 1995 and 1997 at centre-of-mass energies of 130 and 136 GeV are shown separately and combined. Many checks were performed to verify the consistency between the data taken during both these years and throughout the rest of this thesis only the combined 1995 and 1997 values will be considered.

[7] This problem was solved for the data taken after 1995 by introducing tungsten shielding which protects the SW subdetector from the synchrotron radiation.

$\sqrt{s}$ (GeV)			Year	Luminosity (pb^{-1})				
130.25	$\pm$	0.050	1995	2.70	$\pm$	0.02	$\pm$	0.01
130.00	$\pm$	0.030	1997	2.52	$\pm$	0.02	$\pm$	0.01
130.12	$\pm$	0.042	1995+1997	5.22	$\pm$	0.03	$\pm$	0.02
136.22	$\pm$	0.050	1995	2.58	$\pm$	0.02	$\pm$	0.01
135.98	$\pm$	0.030	1997	3.36	$\pm$	0.03	$\pm$	0.02
136.07	$\pm$	0.040	1995+1997	5.95	$\pm$	0.03	$\pm$	0.03
161.34	$\pm$	0.050	1996	9.92	$\pm$	0.04	$\pm$	0.03
172.08	$\pm$	0.060	1996	10.11	$\pm$	0.04	$\pm$	0.04
182.68	$\pm$	0.060	1997	53.85	$\pm$	0.14	$\pm$	0.19
188.66	$\pm$	0.200	1998	74.42	$\pm$	0.10	$\pm$	0.30

Table 4.5: The luminosity weighted mean beam energy, the year at which the data was taken and the integrated data luminosity for the energies analysed. The error on the beam energy is the combined statistical and systematic error, for the luminosity the first is statistical the second systematic.

Chapter 5

Study of Muon Pair Events

5.1 Monte Carlo Studies

The μ pair events are easy to identify as the μ is a relatively long lived minimum ionising particle which passes through the lead glass of the ECAL without losing much of its energy and, unlike the hadrons, it is not stopped by the iron in the HCAL. This means it is able to travel through the detector before decaying and in general it is the only particle from the e^+e^- interaction to leave hits in the muon chambers.

5.1.1 Muon Identification

The identification of muons in the detector has been intensively studied for the LEP1 analyses and is based on the series of cuts on the track properties listed below.

A track passing the lepton pair preselection given in chapter 4 is identified as a muon if either:

1. There are at least two muon chamber hits associated with the charged track.

2. There are at least four hadron calorimeter strip hits with an average number of hits per layer less than two. In addition for $|\cos\theta| < 0.65$ there must be at least one hit in one of the outer three layers of these strips.

3. The track has momentum p where $p > 15$ GeV, and less than 3 GeV is deposited in the ECAL within 63 mrad of the track.

5.1.2 Event Selection

The μ pair event selection is also based on that used at LEP1, with modifications to improve the efficiency of the selection for the higher collision energies and reduce the background, which increases with $\sqrt{s}$. The selection used for the results presented in this thesis is given below.

For an event to be selected as a μ pair:

- There must be at least two tracks that are identified as muons, within $|\cos\theta| < 0.95$ separated by at least 320 mrad.

  If more than one pair of tracks satisfy this criterion then the pair with the highest momentum sum is selected.

- There must be less than three tracks with $p_T > 0.7$ GeV.

- $X_{TOT} > 0.35 + \frac{M_Z^2}{2s}$ where X_{TOT} is the scalar sum of the momenta of the two muon candidates plus the energy of the largest ECAL cluster in the event divided by the centre-of-mass energy.

  In the original LEP1 selection this cut was $X_{TOT} > 0.6$.

The distribution of this quantity for 161 and 189 GeV data and Monte Carlo is shown in figure 5.1(a) and (b) respectively, each plot has three peaks. The peak at high X_{TOT} is predominantly due to the non-radiative events, the peak at low X_{TOT} to the 2-photon background events and the events in the central peak are mainly radiative events. In these events the photons escape down the beam pipe, and so are undetected, leaving only the momenta of the two boosted muons for the calculation of this quantity. As the energy of the emitted photons increases with increasing $\sqrt{s}$ the central peak shifts towards lower values of X_{TOT} and so to obtain the largest efficiency for detecting radiative events the position of the cut on this quantity varies as a function of $\sqrt{s}$ to be below the position of this peak. The value which the function of this cut takes for the range $100 < \sqrt{s} < 200$ GeV is shown in figure 5.2.

In addition to the above a non-radiative event must satisfy:

- Reconstructed $s'/s > 0.7225$.

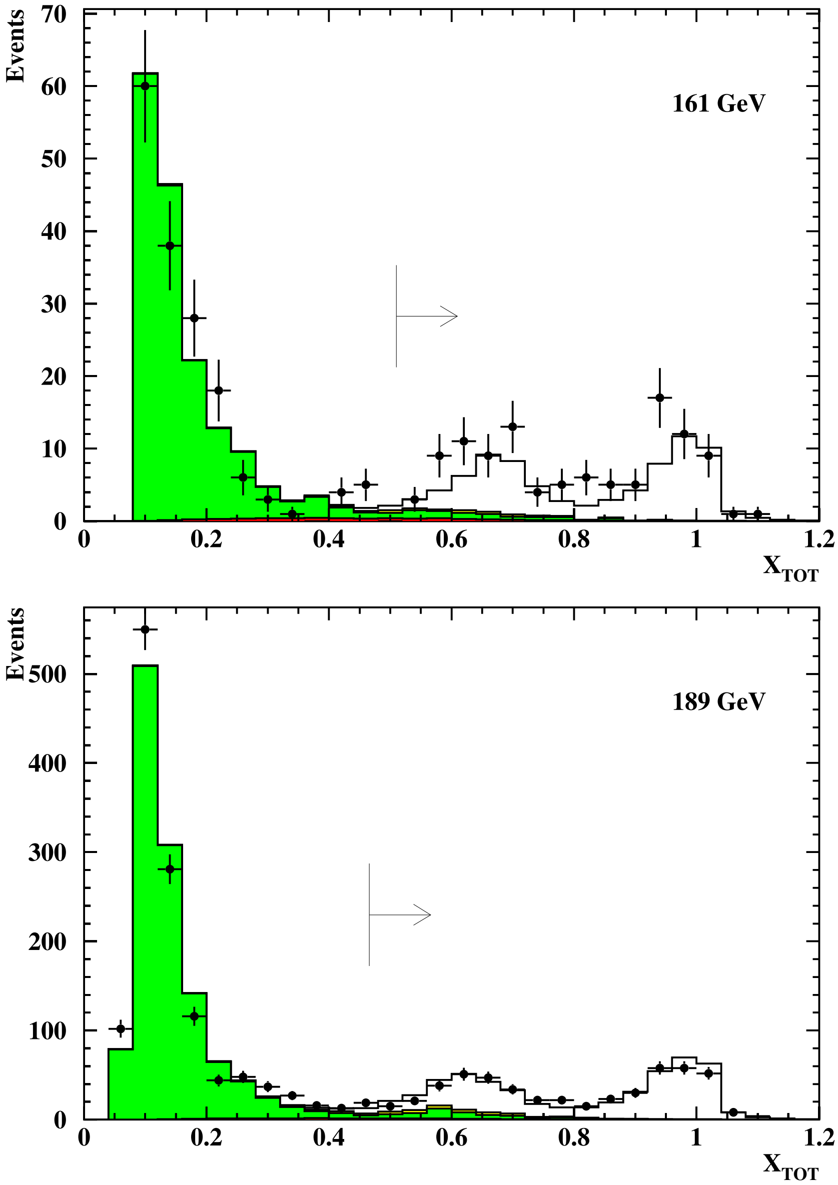

Figure 5.1: The distribution of X_{TOT} before the cut on this quantity for the μ pair events at 161 GeV and 189 GeV.

The points represent the data and the histograms are the Monte Carlo prediction scaled to the integrated data luminosity. The open histogram is the μ pair Monte Carlo prediction and the medium grey histogram is the predicted background contribution. The arrow shows which events are selected.

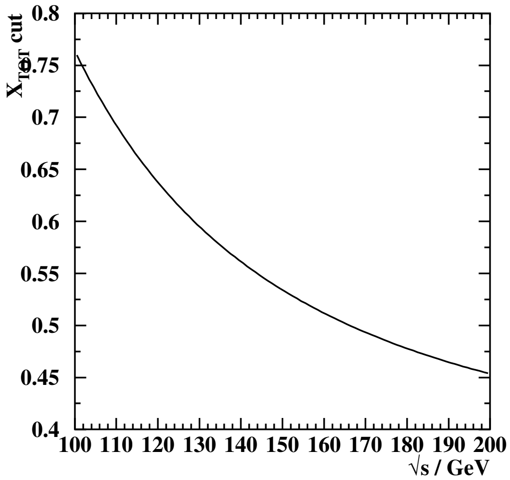

Figure 5.2: The position of the cut on X_{TOT} as a function of $\sqrt{\mathrm{s}}$ for all energies between 100 and 200 GeV.

Figure 5.3 shows the distribution of X_{TOT} against $M_{\mu^+\mu^-}$ before cuts on these quantities are applied for the $\mathrm{s}'/\mathrm{s} > 0.7225$ selection at 184 GeV. The μ pair events which have a generated $\mathrm{s}'/\mathrm{s} > 0.7225$ are shown as the black points, these are clustered at high X_{TOT} and high $M_{\mu^+\mu^-}$. The tail of events at $X_{TOT} = 1$ stretching up to high values of $M_{\mu^+\mu^-}$ are events where the momentum of the tracks are poorly measured. Events lying along the diagonal, from (0,0) to ($\sqrt{\mathrm{s}}$,1), are events where any emitted initial state photons are undetected. The feedthrough μ pair events, usually arising when both the incoming electron and positron emit an initial-state photon, are the dark grey crosses, these are mainly clustered in three regions around $M_{\mu^+\mu^-} = M_Z$. Some are in a high X_{TOT} region where all photons are detected, and others in a low X_{TOT} region where none of the photons are detected, and the middle X_{TOT} region where some of the photons are detected. The very light grey x's are the background events. These are clustered at low values of $M_{\mu^+\mu^-}$.

As can be seen in figure 5.3 some background and many feedthrough events still pass the cut on X_{TOT}, but these generally have low $M_{\mu^+\mu^-}$. These events can be rejected with little effect on the μ pair selection efficiency by an additional cut. This cut is positioned just above the radiative return Z^0 peak.

- $M_{\mu^+\mu^-} > \sqrt{(M_Z^2 + 0.1s)}$.

Hence, events for the non-radiative sample are selected if they lie above the solid line, showing the position of the cut on X_{TOT} for the 184 GeV data, rejecting the majority of background events; and if they lie to the right of the dashed line, showing the additional cut on $M_{\mu^+\mu^-}$, rejecting more of the background contamination and many feedthrough events.

Figure 5.4 shows the same distribution for the s$'$/s > 0.01 selection at 184 GeV before the cuts on these quantities. The black points represent the signal μ pair events, they are clustered in the same regions as for figure 5.3 but with many more events in the regions near $M_{\mu^+\mu^-} = M_Z$, these are the additional radiative return events where initial-state photons were only emitted from one of the incoming particles. The very light grey x's are the background events. Again these are clustered at low values of $M_{\mu^+\mu^-}$.

The solid line shows the position of the cut on X_{TOT} for the 184 GeV data. Events can only be selected if they lie above this line, so again the majority of background events are rejected. The amount of background passing the selection can also be reduced by cutting on $M_{\mu^+\mu^-}$. This cut is shown by the vertical dashed line. It is positioned just below the radiative return Z^0 peak. However, as the background events generally have low values of X_{TOT}, whereas some signal events have $X_{TOT} = 1$, some selection efficiency can be recovered by restricting the range the cut on $M_{\mu^+\mu^-}$ acts over. So inclusive events must satisfy:

- $X_{TOT} > 0.75 + \frac{M_Z^2}{2s}$

Or,

- $M_{\mu^+\mu^-} > 70$ GeV, where $M_{\mu^+\mu^-}$ is the mass of the μ pair system.

This requirement on the values of X_{TOT} or $M_{\mu^+\mu^-}$ is shown by the dashed lines forming a box. Events are only selected if they lie outside this box.

5.1.3 Efficiency, Feedthrough and Background

This selection is applied to the various Monte Carlo samples used at each energy to give the efficiency, feedthrough and background estimate given in table 5.1.

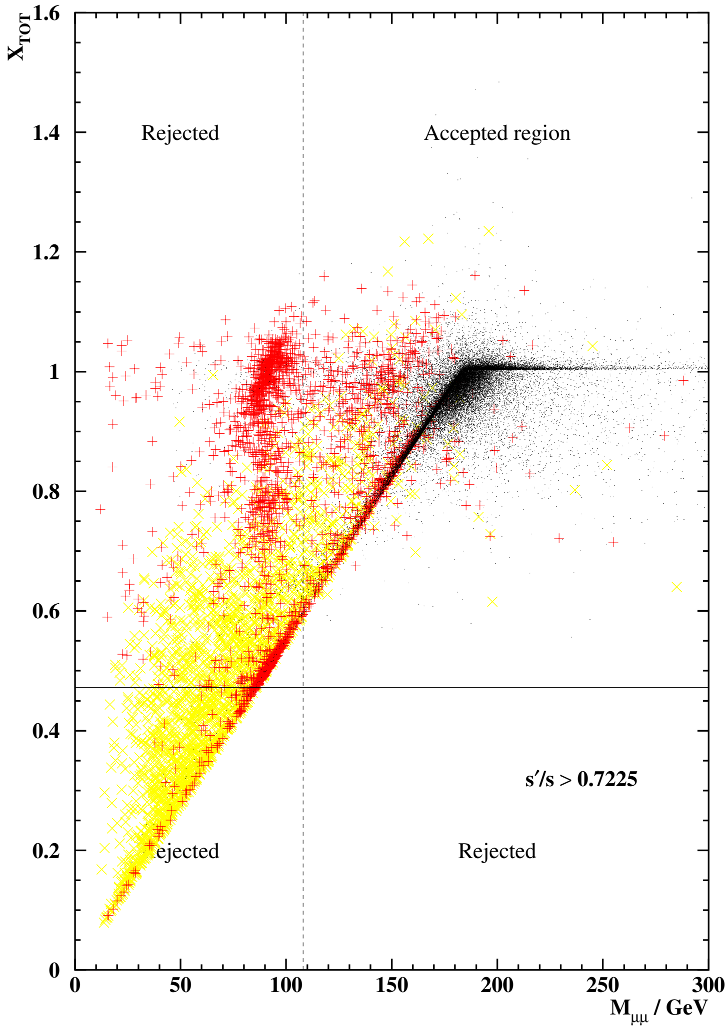

Figure 5.3: The distribution of X_{TOT} against $M_{\mu^+\mu^-}$ in GeV before the cut on either of these quantities for the 184 GeV Monte Carlo samples for $\mathrm{s}'/\mathrm{s} > 0.7225$ events.

The black points represent the truly non-radiative μ pair events, the dark grey crosses represent the feedthrough μ pair events and the very light grey x's are the background from other processes. The lines show the position of the cuts on these quantities.

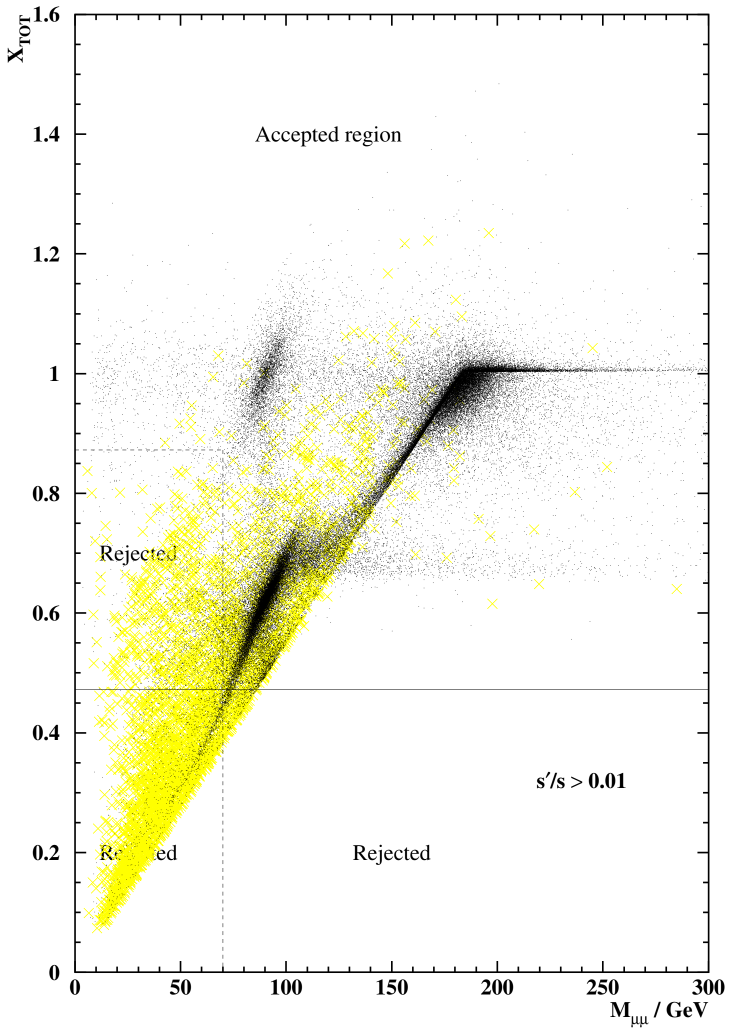

Figure 5.4: The distribution of X_{TOT}, against $M_{\mu^+\mu^-}$ in GeV before the cut on either of these quantities for the 184 GeV Monte Carlo samples for $\mathrm{s}'/\mathrm{s} > 0.01$ events.

The black points represent the μ pair events and the very light grey x's are the background from other processes. The lines show the position of the cuts on these quantities.

	$\sqrt{s}$ GeV	Efficiency %	Background pb	Feedthrough pb
$s'/s > 0.01$	130.12	$79.88 \pm 0.29 \pm 0.80$	$0.327 \pm 0.120 \pm 0.110$	N/A
	136.07	$79.36 \pm 0.29 \pm 0.79$	$0.299 \pm 0.110 \pm 0.101$	
	161.34	$77.41 \pm 0.15 \pm 0.77$	$0.296 \pm 0.041 \pm 0.079$	
	172.08	$76.21 \pm 0.14 \pm 0.76$	$0.391 \pm 0.048 \pm 0.094$	
	182.68	$74.25 \pm 0.14 \pm 0.74$	$0.308 \pm 0.014 \pm 0.074$	
	188.66	$74.20 \pm 0.15 \pm 0.74$	$0.326 \pm 0.024 \pm 0.083$	
$s'/s > 0.7225$	130.12	$86.68 \pm 0.40 \pm 0.87$	$0.113 \pm 0.100 \pm 0.057$	$0.246 \pm 0.017 \pm 0.006$
	136.07	$86.96 \pm 0.39 \pm 0.87$	$0.103 \pm 0.091 \pm 0.052$	$0.148 \pm 0.012 \pm 0.013$
	161.34	$88.10 \pm 0.19 \pm 0.88$	$0.056 \pm 0.018 \pm 0.013$	$0.091 \pm 0.004 \pm 0.001$
	172.08	$88.39 \pm 0.16 \pm 0.88$	$0.055 \pm 0.014 \pm 0.018$	$0.076 \pm 0.003 \pm 0.002$
	182.68	$88.33 \pm 0.16 \pm 0.88$	$0.063 \pm 0.005 \pm 0.024$	$0.065 \pm 0.002 \pm 0.001$
	188.66	$88.65 \pm 0.18 \pm 0.89$	$0.077 \pm 0.008 \pm 0.031$	$0.060 \pm 0.002 \pm 0.002$

Table 5.1: The predicted efficiency, feedthrough and background for the μ pair analysis at each energy. The first error is statistical and the second systematic.

Efficiency

For the non-radiative selection the efficiency is high and fairly constant. However, due to the poorer resolution of the Z^0 peak at the higher energies, the positioning of the X_{TOT} cut is eating slightly into the Z^0 peak. Hence, the inclusive efficiency decreases with increasing $\sqrt{\mathrm{s}}$.

The systematic error on the efficiency was determined using the high statistics Z peak LEP1 data and Monte Carlo samples as opposed to the LEP2 data. However, the position of the X_{TOT} cut scales with $\sqrt{\mathrm{s}}$ and so when the selection is used at the Z^0 energy it seriously eats into the Z peak. This was overcome by relaxing such cuts. The relaxed selection is then applied to the LEP1 data and Monte Carlo, and the number of data events selected is compared to the number predicted by the Monte Carlo. The percentage difference is taken to be the systematic error on the efficiency.

Feedthrough

The feedthrough background decreases with increasing $\sqrt{\mathrm{s}}$ due to the increasing separation between the full energy $\sqrt{\mathrm{s}}$ peak and the Z^0 peak.

The systematic error on the feedthrough is obtained by comparing the measured feedthrough to that obtained when the $\mathrm{s'/s}$ cut for the non-radiative selection is changed to $\mathrm{s'/s} > 0.75$[1] and $\mathrm{s'/s} > 0.65$[2].

Background

In the inclusive sample the cross-section of the background is relatively constant for all energies. At 189 GeV the background accounts for approximately 5% of the all selected events. Of these over 50% of the background arises from the two photon $e^+e^-\mu^+\mu^-$ process, these will generally be where the electron pair escape down the beam pipe. A further 25% arises from τ pair events where both τ's decay into μ's. The remainder are from other 4-fermion and two photon processes involving a muon or tau pair. Above the W pair production threshold, the fraction of events arising

[1] This increase is 10% of the difference between its normal value of $\mathrm{s'/s} > 0.7225$ and $\mathrm{s'/s} = 1$.
[2] This decrease is 10% of the difference between its normal value and $\mathrm{s'/s} = 0$.

from a pair of W's decaying into $\mu\nu_\mu$ increases. At 189 GeV this process alone accounts for approximately 20% of the background.

For the non-radiative selection between 1.5% and 2.5% of the events are from other physics processes but the background composition is significantly different due to the requirement that the event has a high $\sqrt{s'}$ and hence is back-to-back. Because of this, nearly 40% of the background arises from τ pair events where the τ's are produced back-to-back and both decay into μ's. Approximately 30% arise from the $l^+l^-l^+l^-$ process and 20% from the two photon $e^+e^-\mu^+\mu^-$ process mentioned above. The feedthrough background makes up approximately 2% of all selected events, bringing the total background to a similar level as that for the inclusive selection.

Table 5.2 shows the predicted background cross-sections for the 189 GeV analysis.

		$s'/s > 0.7225$ $\sigma(pb)$	$s'/s > 0.01$ $\sigma(pb)$	systematic %
2-fermion	$\mu^+\mu^-$	0.060 ± 0.002	N/A	-
	$\tau^+\tau^-$	0.031 ± 0.002	0.086 ± 0.003	50
	e^+e^-	0.003 ± 0.003	0.003 ± 0.003	50
2γ	$e^+e^-\mu^+\mu^-$	0.015 ± 0.007	0.17 ± 0.02	2.9
4-fermion	$e^+e^-\mu^+\mu^-$	0.0016 ± 0.0006	0.0068 ± 0.0011	50
	$e^+e^-\tau^+\tau^-$	0	0.0006 ± 0.0004	50
	$l^+l^-q\bar{q}$	0.0012 ± 0.0005	0.0012 ± 0.0005	50
	$l^+l^-l^+l^-$	0.024 ± 0.002	0.059 ± 0.003	50

Table 5.2: The Monte Carlo predicted background for the 189 GeV μ pair selection showing the Monte Carlo process, the background cross-section for the $s'/s > 0.7225$ and $s'/s > 0.01$ selections and the percentage systematic errors that are applied to the predicted cross-section.

The systematic error on the background cross-section is determined by loosening the cuts which are important for rejecting the background under study. This loosened selection is then applied to the data and Monte Carlo samples for each energy. By combining the data taken at each energy the statistical limitation is reduced. A region in the observable physical quantities where the background reaction dominates all other reactions is selected and the total number of data events passing the selection in this region is compared with the Monte Carlo prediction and the percentage difference is used as the systematic error.

Figure 5.5 illustrates this for the two-photon $e^+e^-\mu^+\mu^-$ background process. The plot shows the X_{TOT} distribution, after all other cuts, for all energies combined. In the region indicated by the arrows there are 2503 data events, the Monte Carlo predicts that there should be a total of 2576 events in this region. In this instance the statistical precision on the number of data events is 2.0%, however the discrepancy of approximately 73 events equates to a 2.9% error and this value was used for the systematic error on this two-photon $e^+e^-\mu^+\mu^-$ background Monte Carlo for all energies.

In cases where the statistical precision limits this method, it is the statistical error on the number of data events which is taken as the systematic error.

For the background reactions where no region can be found in which the reaction dominates all other reactions the systematic error was conservatively taken to be 50%.

5.1.4 Comparison to other LEP experiments

The selection efficiencies and backgrounds for both the $\mathrm{s}'/\mathrm{s} > 0.7225$ and $\mathrm{s}'/\mathrm{s} > 0.01$ samples are similar to those obtained in the analyses of this process performed by the ALEPH experiment [52]. However, unlike the other LEP experiments ALEPH selects non-radiative events by requiring $\mathrm{s}'/\mathrm{s} > 0.81$ and scales the measurement using a theoretical prediction to the same $\mathrm{s}'/\mathrm{s} > 0.7225$ used by the other experiments. ALEPH does not quote a value for the feedthrough.

The DELPHI experiments analyses [53] generally have selection efficiencies a few percent higher for the $\mathrm{s}'/\mathrm{s} > 0.7225$ sample. DELPHI define the inclusive selection as $\sqrt{\mathrm{s}'} > 75$ GeV; they obtain selection efficiencies around 90%, several percent higher than that for the $\mathrm{s}'/\mathrm{s} > 0.01$ sample in this thesis.

In addition the DELPHI experiment calculates the $\sqrt{\mathrm{s}'}$ using a kinematic fit, hence the feedthrough is generally a factor of two smaller. However, the background contamination in the analyses in this thesis are around half those in the DELPHI

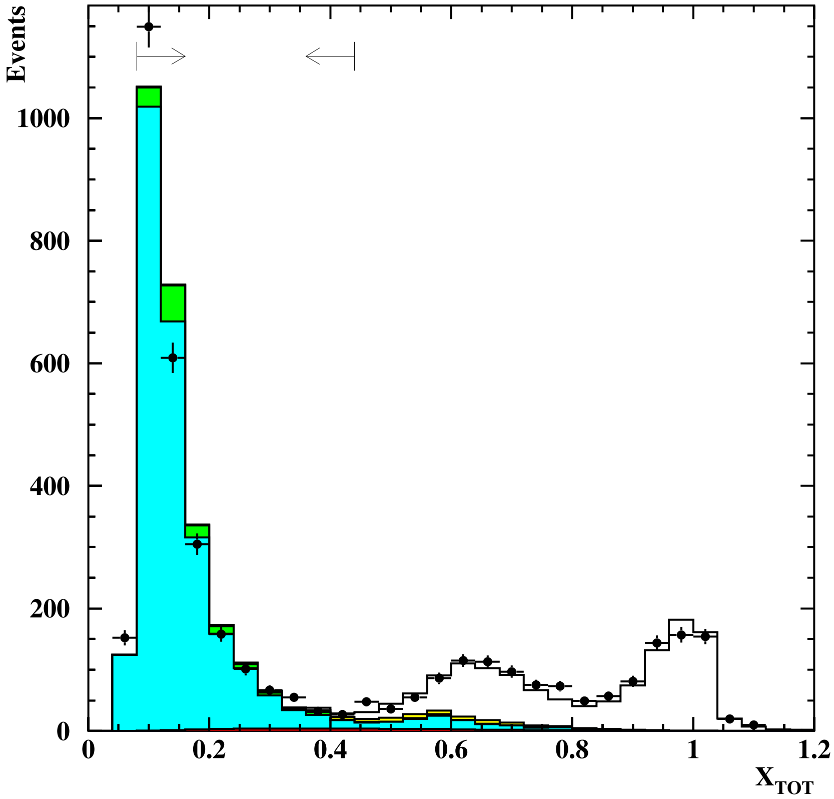

Figure 5.5: The X_{TOT} distribution for all energies combined.

The points represent the data and the histograms are the Monte Carlo prediction scaled to the integrated data luminosity. The open histogram is the μ pair Monte Carlo prediction, the light grey histogram is the background from the two photon $e^+e^-\mu^+\mu^-$ process and the medium grey histogram is the predicted background contribution from other two photon eeff processes. The arrows indicate the region in which the number of events from data and Monte Carlo are compared.

analysis.

The analyses performed by the L3 experiment [54] have selection efficiencies which are significantly lower than those of the other LEP experiments at around 70% for the $s'/s > 0.7225$ sample and 60% for the $s'/s > 0.01$ sample. The feedthrough and backgrounds obtained by the L3 experiment are 3-4 times higher than those in the analyses presented here.

5.2 Data

The μ pair selection described in the previous section was applied to the data taken at each energy to measure the cross-sections, angular distributions and asymmetries for the two s'/s samples.

The $\sqrt{s'}$ distributions for each energy are shown in figures 5.6 and 5.7. The full energy and radiative return peaks can clearly be seen and there is generally good agreement between data and Monte Carlo. The number of data events in the non-radiative peak at 136 GeV is high compared to the prediction, but this discrepancy is only around two standard deviations above the expectation so is consistent with a statistical fluctuation.

5.2.1 Cross-section

To calculate the cross-section for the μ pair production for the $s'/s > 0.7225$ and $s'/s > 0.01$ selections at the different energies the number of events passing the cuts, N, is converted to a cross-section by dividing by the integrated luminosity, L (pb^{-1}). It is corrected for the total accepted interference cross-section, σ_{int}, the background cross-section from other processes, σ_b, the feedthrough background cross-section, σ_f, and finally for the selection efficiency, ϵ, to give a cross-section in *pb*.

$$\sigma = \frac{\frac{N}{L} - \sigma_{int} - \sigma_b - \sigma_f}{\epsilon} \tag{5.1}$$

The measured cross-sections for the inclusive and non-radiative μ pair selections are tabulated in table 5.3 and shown in figure 5.8. The inserts (figure 5.8(a) and (b)) show the ratio of the measured cross-section to the Standard Model predictions

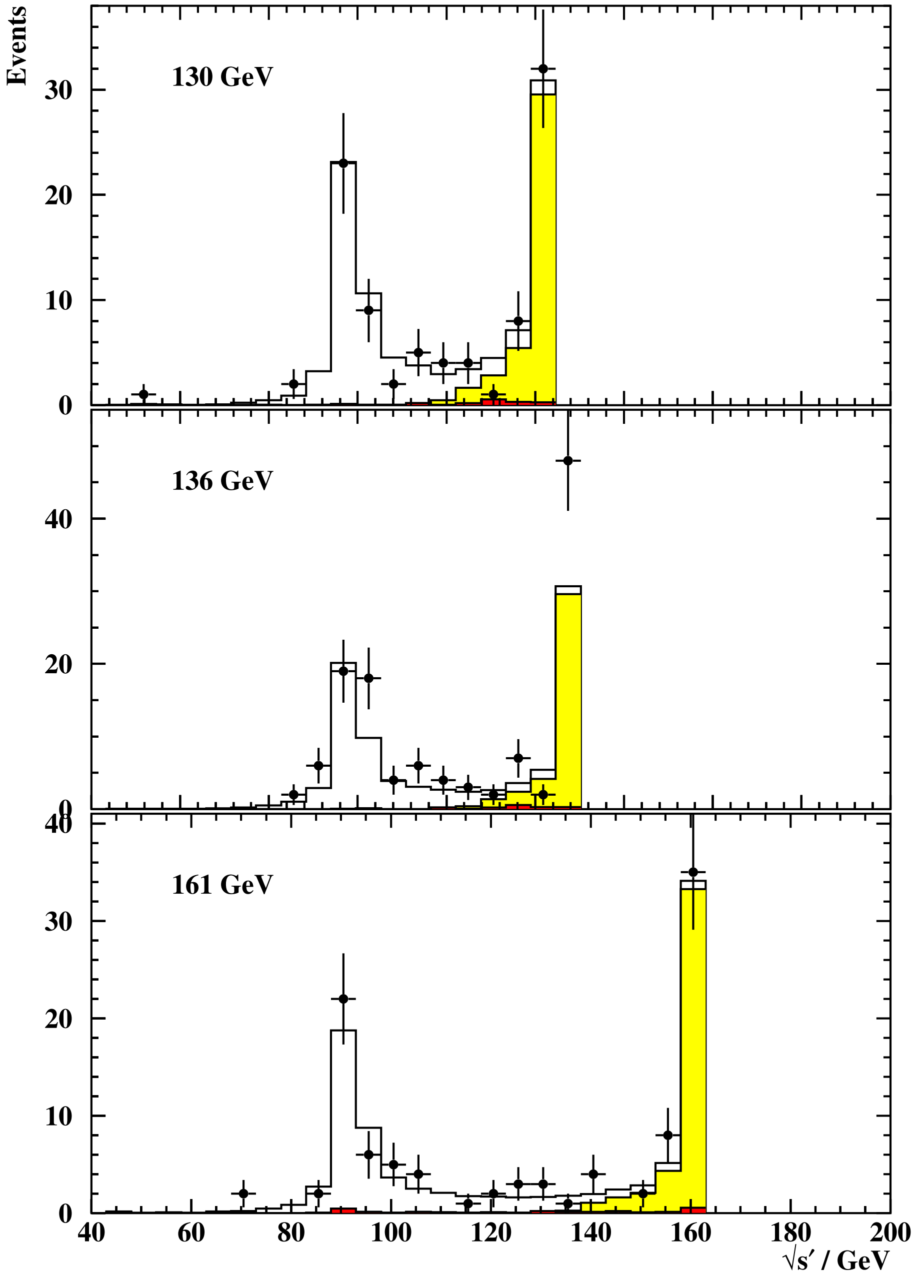

Figure 5.6: The $\sqrt{s'}$ distributions for the μ pair events at 130, 136 and 161 GeV. The points represent the data and the histograms are the Monte Carlo prediction scaled to the integrated data luminosity. The open histogram is the μ pair Monte Carlo prediction for the $s'/s > 0.01$ selection, the very light grey histogram is the $\mu^+\mu^-$ Monte Carlo prediction for the true $s'/s > 0.7225$ events and the dark grey shading is the predicted background contribution.

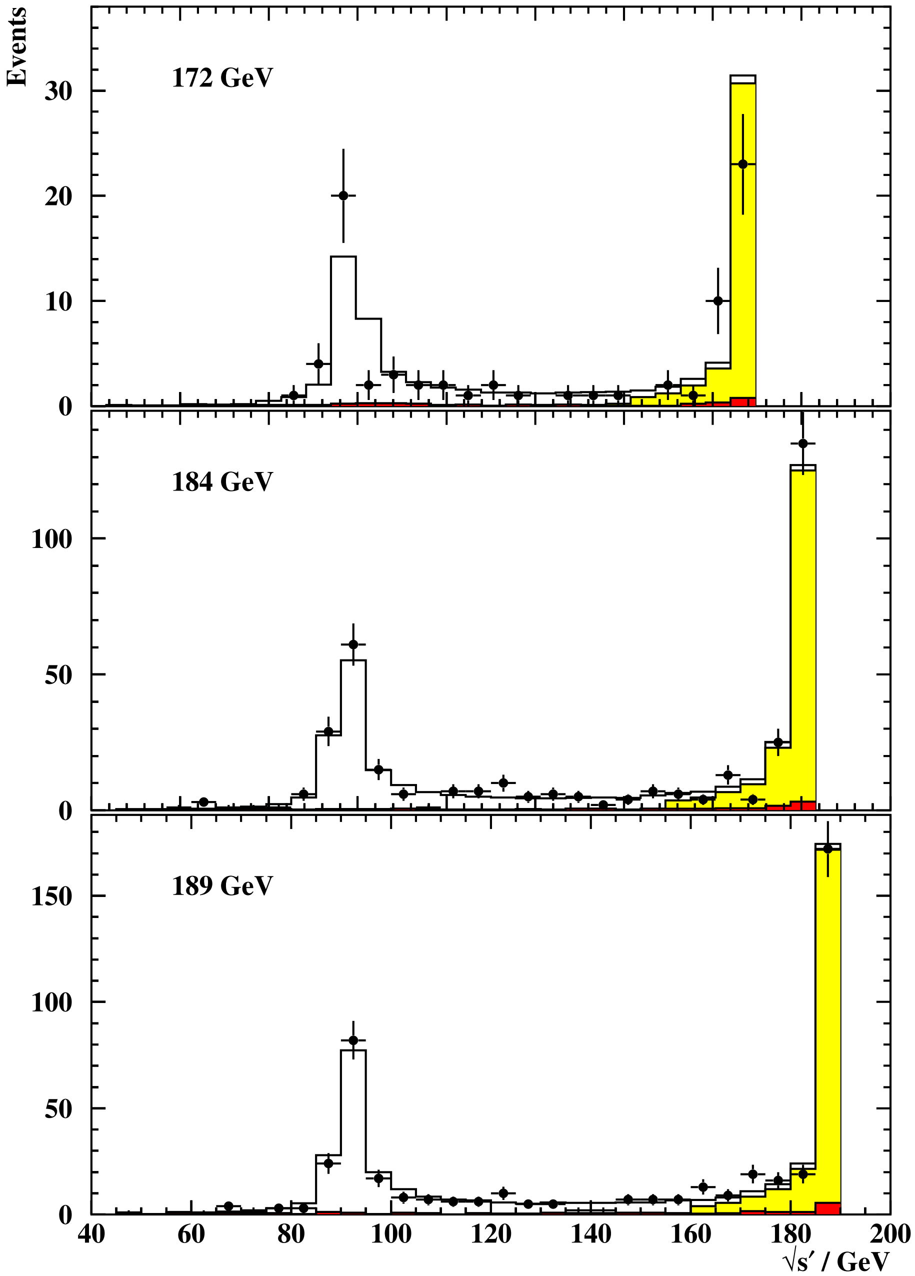

Figure 5.7: The $\sqrt{s'}$ distributions for the μ pair events at 172, 184 and 189 GeV. The symbols and shadings are the same as used in figure 5.6.

for the s′/s > 0.01 and s′/s > 0.7225 selections respectively. The measured cross-sections shown are generally close to the ZFITTER prediction. Due the the excess of non-radiative events seen in the 136 GeV data, the measured cross-sections are well above the predicted value.

	$\sqrt{s}$ GeV	Selected Events	σ pb	σ^{SM} pb
s′/s > 0.01	130.12	91	21.32 ± 2.24 ± 0.34	22.12
	136.07	121	25.20 ± 2.29 ± 0.43	18.88
	161.34	100	12.60 ± 1.26 ± 0.23	11.27
	172.08	77	9.44 ± 1.08 ± 0.22	9.59
	182.68	367	8.73 ± 0.46 ± 0.19	8.31
	188.66	460	7.86 ± 0.37 ± 0.19	7.72
s′/s > 0.7225	130.12	38	7.86 ± 1.28 ± 0.17	8.46
	136.07	54	10.05 ± 1.37 ± 0.27	7.31
	161.34	42	4.57 ± 0.71 ± 0.13	4.62
	172.08	35	3.71 ± 0.63 ± 0.12	3.96
	182.68	174	3.46 ± 0.26 ± 0.12	3.45
	188.66	226	3.23 ± 0.22 ± 0.12	3.21

Table 5.3: The measured cross-sections for μ pair events at each energy after the small correction for small initial/final-state radiation interference. Shown are the number of selected events, the measured cross-section and the ZFITTER prediction. The first error is statistical and the second systematic.

The systematic error on the cross-section is assessed by comparing the measured cross-section using this formula to that obtained when the error on the luminosity and interference correction, the number of cosmic ray events and the statistical and systematic errors of the efficiency, background and feedthrough are taken into account in equation 5.1[3].

Table 5.4 shows the systematic errors considered for the μ pair cross-section measurements at 189 GeV, the corresponding errors for the τ pairs are also shown.

[3]For instance, the systematic error arising from the statistical error on the luminosity, ΔL_{stat},

Note that in all cases the statistical error dominates the systematic errors. For the lower statistics runs taken at 130-172 GeV, the systematic error is approximately a factor of 5 times smaller than the statistical error. This is reduced to approximately a factor of 2 for the higher statistic runs of 184 and 189 GeV.

For the μ pair cross-section the dominant systematic error comes from the uncertainty due to the number of cosmic ray events. For future higher energy running the systematic error from the possible cosmic ray contamination may become increasingly dominant as the number of cosmic ray events is constant with time whereas the Standard Model predicts the number of data events will decrease for the same LEP performance. In addition, the uncertainty on the inclusive μ pair cross-section measurement also has a large contribution arising from the systematic error assigned to the background.

The cross-section results of the other LEP experiments are similar to those presented here and the measurements have a reasonable scatter above and below the predicted Standard Model cross-section, thereby providing further indication that large excess of μ pair events seen at 136 GeV is a statistical fluctuation. All experiments quote a similar value of 3-5% for the systematic error on the cross-section measurement for both the $s'/s > 0.7225$ and $s'/s > 0.01$ samples at all energies.

5.2.2 Angular Distribution and Asymmetry

The uncorrected angular distributions for data and that predicted by Monte Carlo are shown for the μ pair $s'/s > 0.01$ and $s'/s > 0.7225$ selections at each energy in figures 5.9 and 5.10. The histograms, showing the Monte Carlo prediction, are normalised to the same integrated luminosity as the data, shown by the points. Here the error bars show the size of the statistical error, due to the low number of events this error is calculated from Poissonian statistics. For the $\cos\theta$ measurement if there are fewer than 3 hits in both the Stereo wires of the CV subdetector and in the CZ subdetector the track is considered to be poorly reconstructed and so the $\cos\theta$ is

---

is:

$$\Delta\sigma(\Delta L_{stat}) = |\sigma - \frac{\frac{N}{L+\Delta L_{stat}} - \sigma_{int} - \sigma_b - \sigma_f}{\epsilon}|$$

	$s'/s > 0.01$		$s'/s > 0.7225$	
	$\mu^+\mu^-$	$\tau^+\tau^-$	$\mu^+\mu^-$	$\tau^+\tau^-$
$\Delta\sigma(\Delta\epsilon_{stat})$	0.016	0.037	0.006	0.016
$\Delta\sigma(\Delta\sigma_{b_{stat}})$	0.032	0.084	0.009	0.034
$\Delta\sigma(\Delta\sigma_{f_{stat}})$	–	–	0.003	0.005
$\Delta\sigma(\Delta\epsilon_{sys})$	0.079	0.214	0.033	0.085
$\Delta\sigma(\Delta\sigma_{b_{sys}})$	0.112	0.276	0.035	0.063
$\Delta\sigma(\Delta\sigma_{f_{sys}})$	–	–	0.002	0.001
$\Delta\sigma(N_{cosmic})$	0.127	–	0.106	–
$\Delta\sigma(\Delta L_{stat})$	0.012	0.014	0.005	0.005
$\Delta\sigma(\Delta L_{sys})$	0.033	0.040	0.014	0.015
$\Delta\sigma(\Delta\sigma_{int})$	0.004	0.005	0.012	0.010
$\Delta\sigma stat$	0.367	0.491	0.216	0.261

Table 5.4: The systematic errors considered for the cross-section measurements at 189 GeV showing the cause of the systematic, and the error in pb for the $s'/s > 0.01$ and $s'/s > 0.7225$ selections of the μ and τ pair analyses. For comparison the statistical error is also given.

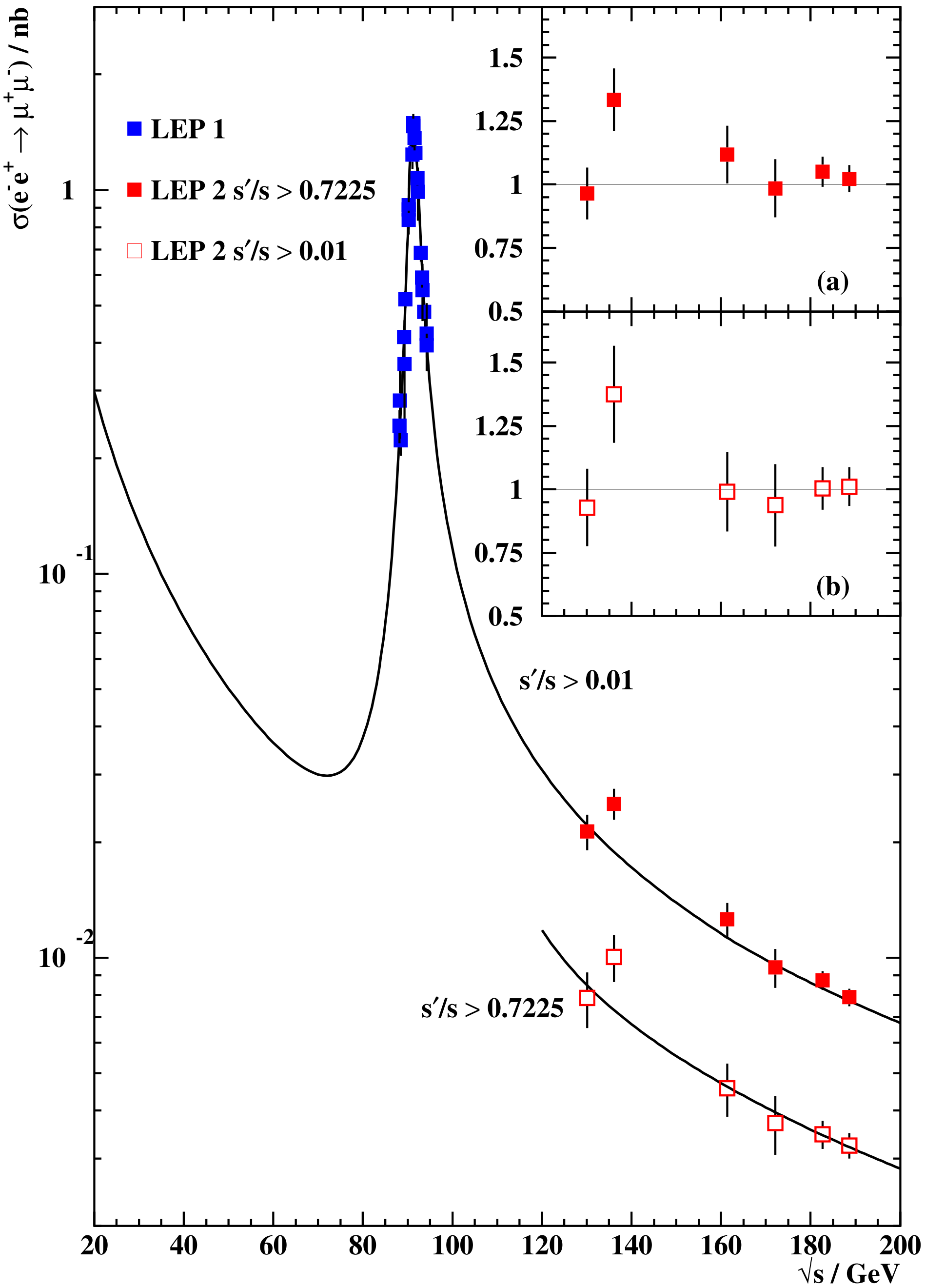

Figure 5.8: The measured cross-section for $e^+e^- \to \mu^+\mu^-$ as a function of $\sqrt{s}$ showing the results taken at LEP1 [51] and the results obtained in the analyses for $s'/s > 0.7225$ and $s'/s > 0.01$ selections. The solid lines are the ZFITTER prediction for the Standard Model cross-section. Inserts (a) and (b) show the ratio of the measured and predicted cross-sections for the $s'/s > 0.01$ and $s'/s > 0.7225$ selections.

obtained from the Muon Chambers. In instances when there is no measurement from the Muon Chambers the track is rejected. For the 130-172 GeV typically 3 to 5 tracks are rejected. However for the later part of the 184 GeV data and all 189 GeV data there was a problem with $\frac{1}{3}$ of the stereo wires in the CV subdetector. This increases the number of rejected tracks to around 1 per pb^{-1} of data. This problem is modelled in the Monte Carlo simulation and so does not cause any bias in the measurements.

In approximately 9% of the events at 130 GeV increasing to 15% of the events at 189 GeV, the two muons are reconstructed as having the same charge. Most of these events occur in the large $|\cos\theta|$ bins. To overcome this other information is used to assign the charges as being different. First if both muons have left well measured tracks in the the central tracking chambers then if the acoplanarity, θ_{acop}[4], of the muons tracks is greater than zero the charge of the highest energy muon is assumed to be the μ^-. This assumption is correct for approximately 80% of such events when studied with the Monte Carlo sample. In events where one of the tracks is well measured the charge of that μ is assumed to be correct. If neither track is well measured the charge of the μ which left the most hits in the central tracking chambers, or has the smallest error on its momentum is assumed to be correct.

Overall there is generally good agreement between the measured and predicted distributions. As the $s'/s > 0.7225$ distribution is a subset of the $s'/s > 0.01$ distribution fluctuations in the same $\cos\theta$ bins at the same energy are correlated.

The measured angular distributions are corrected for background, initial/final-state radiation interference and selection efficiency as illustrated for the μ pair analysis at 184 GeV in figures 5.11 and 5.12.

First the $-q * \cos\theta$ distributions of the selected Monte Carlo events are divided into forty bins covering the full $\cos\theta$ range (figures 5.11(a) and (b)). For the non-radiative case only those events selected with a generated $s'/s > 0.7225$ are used. These distributions are compared to the generated $\cos\theta$ distribution for all Monte Carlo events (figures 5.11(c) and (d)) to obtain a bin by bin selection efficiency (figures 5.11(e) and (f)).

[4] defined as 180° - the angle between the muon tracks in the x-y plane

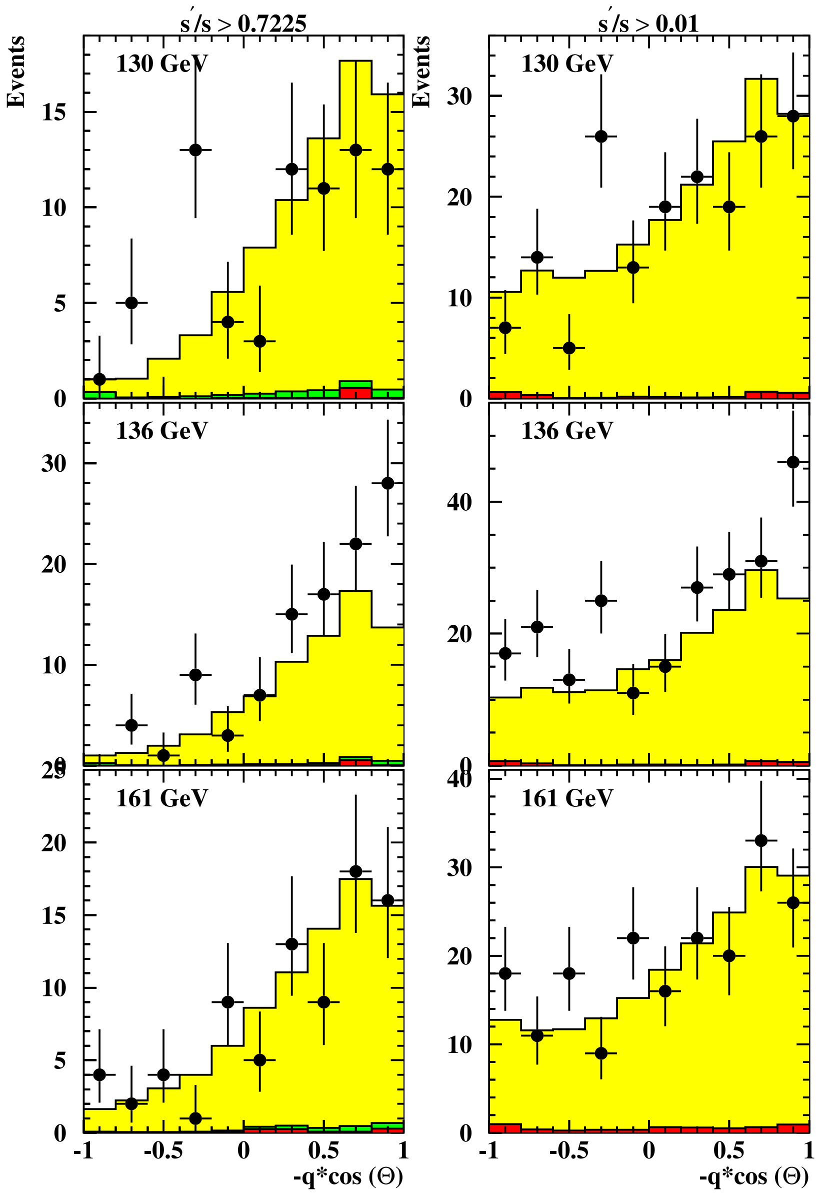

Figure 5.9: The combined negative and positive particle $-q * \cos\theta$ distributions obtained for the $\mathrm{s}'/\mathrm{s} > 0.7225$ and $\mathrm{s}'/\mathrm{s} > 0.01$ μ pair events at 130, 136 and 161 GeV.

The points represent the data, the error bars show the Poissonian statistical error and the histograms are the Monte Carlo prediction scaled to the integrated data luminosity. The very light grey histogram is the μ pair Monte Carlo prediction and the dark grey histogram is the predicted background contribution. The medium grey histogram is the expected contribution from feedthrough events for $\mathrm{s}'/\mathrm{s} > 0.7225$.

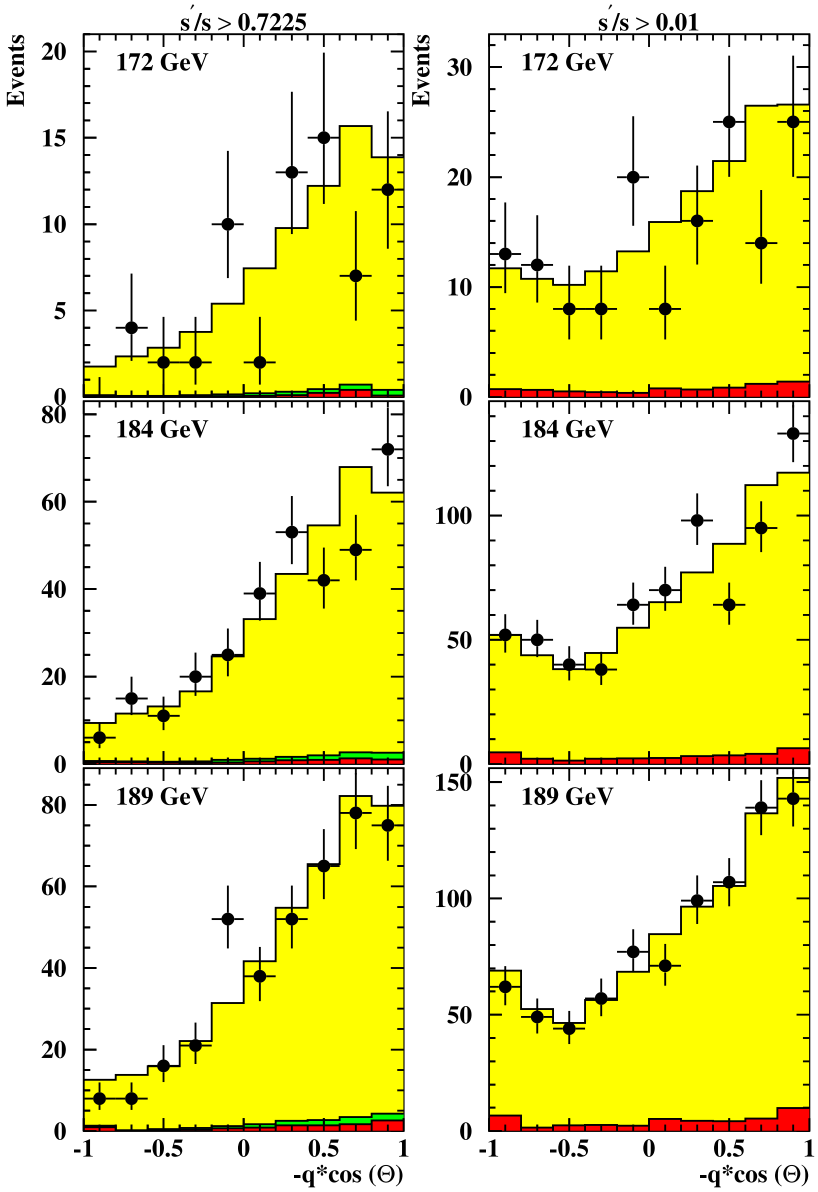

Figure 5.10: The combined negative and positive particle $-q * \cos\theta$ distributions obtained for the $s'/s > 0.7225$ and $s'/s > 0.01$ μ pair events at 172, 184 and 189 GeV. The symbols and shadings are the same as used in figure 5.9.

The efficiency for the $s'/s > 0.7225$ selection (figure 5.11(e)) is generally symmetrical. The lack of symmetry in the outermost bins arises from charge misassignment. Here the event which should have been in the forward (backward) region is reconstructed as being in the backward (forward) region and, as there are more events in the forward region, this leads to an increase in the number of selected events in the backward region and a decrease in the number of events in the forward region. Hence, the overall selection efficiency the bin $-0.95 < \cos\theta < -0.9$ is increased and the selection efficiency in the bin $0.9 < \cos\theta < 0.95$ is decreased.

The efficiency for the $s'/s > 0.01$ selection (figures 5.11(f)) is less symmetric. This is caused by the radiative events. Such events have a lower asymmetry and so are more likely to populate the backward hemisphere. However, as there is a decrease in the overall selection efficiency for these events the efficiency in the backward region is poorer than for the non-radiative event dominated forward region.

In both s'/s samples there is a reduction in the efficiency around $|\cos\theta| = 0.6$. This is the overlap region between the barrel and endcap subdetectors.

Next the distributions of the selected data events (figures 5.12(a) and (b)) are first corrected for small effect from initial/final-state radiation interference by adding the ZFITTER prediction for the number of events in the bin (figures 5.12(c) and (d)), then the backgrounds are corrected for by subtracting the Monte Carlo prediction for the number of events passing the selections arising from other physics processes (medium grey histogram in figures 5.12(e) and (f)) and, in the case of the non-radiative selection, for Monte Carlo prediction for the number of feedthrough events (dark grey histogram in figure 5.12(f)). Finally the distribution is corrected for the efficiency in each $\cos\theta$ bin. The corrected $\cos\theta$ distributions are shown in figures 5.12(g) and (h).

The main background for the $s'/s > 0.7225$ selection arises from the τ pair events, these events have a similar angular distribution to that of the μ pair events. For the $s'/s > 0.01$ selection the $e^+e^-\mu^+\mu^-$ two-photon process provides a significant contribution and these events tend to be in the large $|\cos\theta|$ regions.

Although the two leptons are emitted back-to-back in the rest frame of the collision, the angles measured in the detector for the radiative events are boosted by the

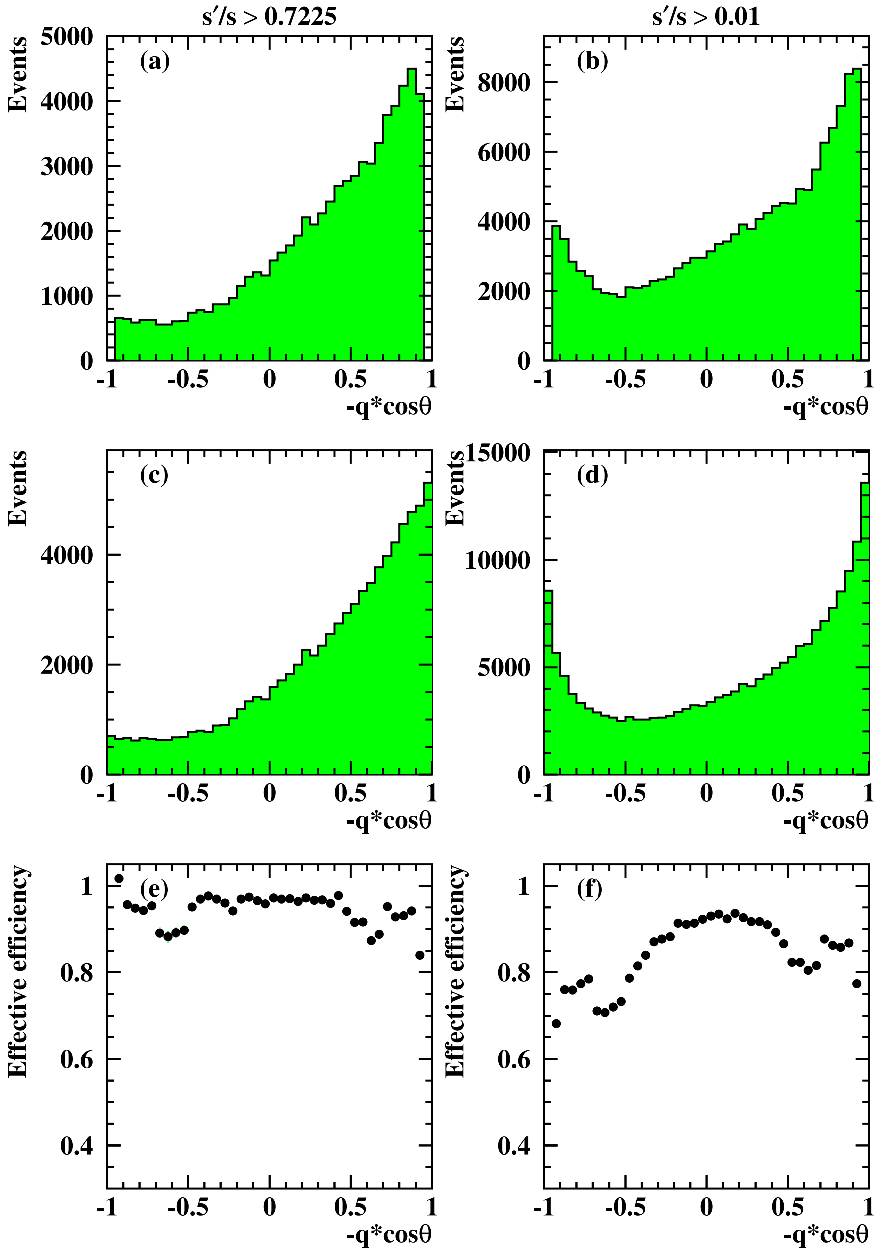

Figure 5.11: Distributions used in the determination of the efficiency for each $\cos\theta$ bin used in the calculation of the asymmetry for the μ pair analysis for $\mathrm{s}'/\mathrm{s} > 0.01$ and $\mathrm{s}'/\mathrm{s} > 0.7225$ events at 184 GeV.

(a) and (b) The $-q * \cos\theta$ distributions of the selected Monte Carlo events.

(c) and (d) The generated $-q * \cos\theta$ distribution of all Monte Carlo events.

(e) and (f) The resulting efficiencies for each $\cos\theta$ bin, here the error bars are statistical.

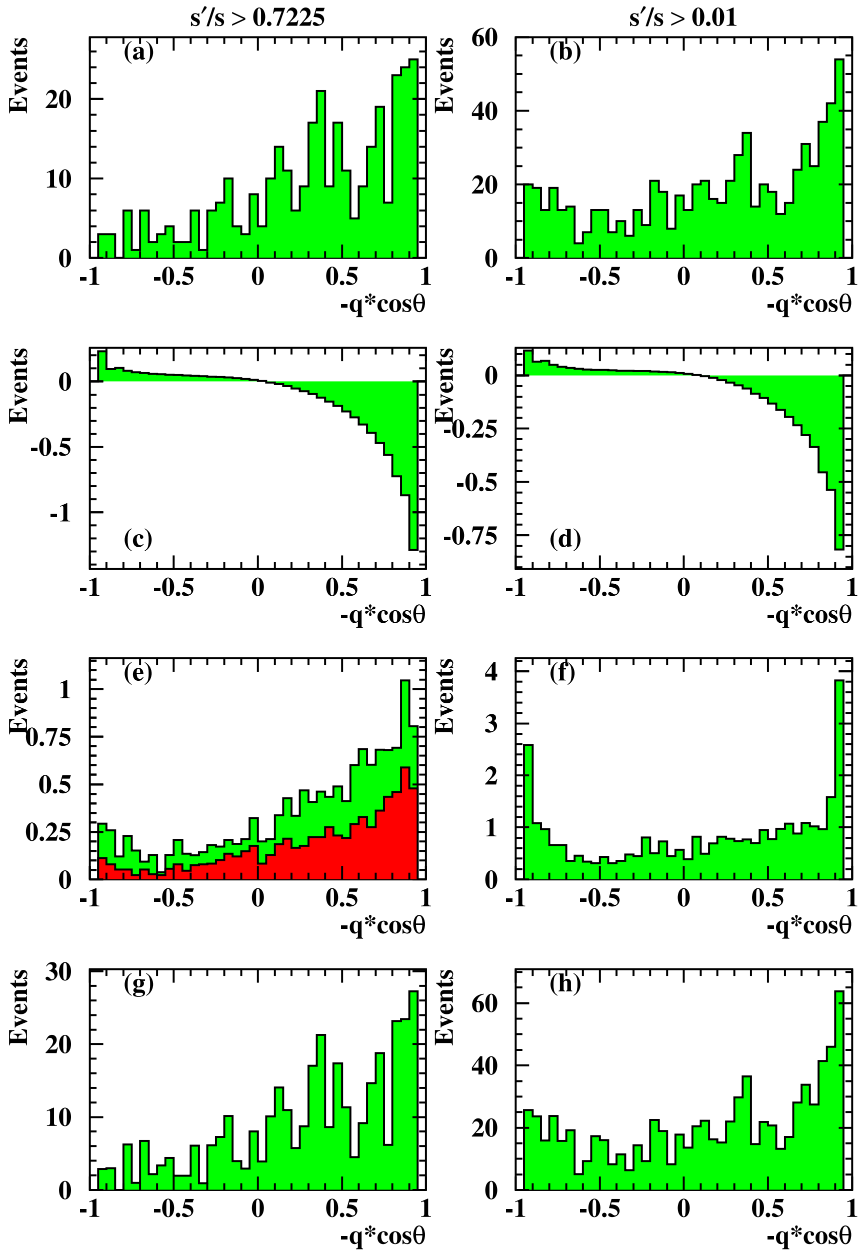

Figure 5.12: Distributions used in the calculation of the asymmetry for the μ pair analysis for $\mathrm{s'/s} > 0.01$ and $\mathrm{s'/s} > 0.7225$ events at 184 GeV.

(a) and (b) The $-q * \cos\theta$ distributions of selected data events.

(c) and (d) The $-q * \cos\theta$ distributions of the interference correction.

(e) and (f) The predicted Monte Carlo $-q * \cos\theta$ distributions of background events (medium grey) and feed-through events for $\mathrm{s'/s} > 0.7225$ (dark grey).

(g) and (h) The corrected $-q * \cos\theta$ distributions of data events.

emission of the initial-state photon(s) so that the two tracks no longer occupy the same $\cos\theta$ bin and hence have a different correction for background, initial/final-state radiation interference and efficiency. This could introduce a difference depending on which lepton was used to determine the asymmetry.

There are two possibilities for reducing this effect. Either the $\cos\theta$ of the leptons in the rest frame of the parent boson can be used, or the distributions obtained from both leptons (signed according to the charge) can be averaged. For the analyses in this thesis the latter method is used.

The summed negative and positive $-q{*}\cos\theta$ distributions are then used to obtain the forward/backward asymmetries for the inclusive and non-radiative μ pair events. The asymmetry was evaluated using the counting method

$$A_{fb} = \frac{N_f - N_b}{N_f + N_b} \tag{5.2}$$

where $N_{f(b)}$ is the corrected number of events in the forward (backward) region.

The statistical error on the asymmetry is determined using

$$(\Delta F(x_1, x_2, ...))^2 = \sum \left(\frac{\delta F}{\delta x_i}\right)^2 \Delta {x_i}^2 \tag{5.3}$$

Then $A_{FB} = \frac{N_F - N_B}{N_F + N_B}$ gives

$$\Delta {A_{FB}}^2 = \frac{4\sqrt{2}}{(N_F + N_B)^4}({N_B}^2 \Delta {N_F}^2 + {N_F}^2 \Delta {N_B}^2) \tag{5.4}$$

where $N_F = \sum \frac{N_{F_i} - B_i}{\epsilon_i}$. Assuming $\Delta B_i = 0$ and $\Delta\epsilon_i = 0$ gives

$$\Delta {N_F}^2 = \sum \frac{\Delta N_{F_i}^2}{{\epsilon_{F_i}}^2} \tag{5.5}$$

Overall this gives

$$\Delta A_{FB}^2 = \frac{4\sqrt{2}}{{N_{total}}^4}((N_B)^2 \sum \frac{\Delta N_{F_i}^2}{{\epsilon_{F_i}}^2} + (N_F)^2 \sum \frac{\Delta N_{B_i}^2}{{\epsilon_{B_i}}^2}) \tag{5.6}$$

where N_{total}, N_F and N_B are the background and efficiency corrected number of events in the full angular distribution, in the forward region and in the backward region respectively, and N_{F_i} and N_{B_i} are the raw number of events in bin i of the forward and backward regions respectively. As the $\cos\theta$ measurements of both particles are fully correlated the statistical error is no longer proportional to $\sqrt{N}$

and so combining the distributions of the negative and positive particles gives no improvement in the statistical error, hence the factor of $\sqrt{2}$ is included in the above formula.

The systematic error is determined by comparing the measured asymmetries using different methods of obtaining $\cos\theta$ to that using the standard method described above. These different methods use the $\cos\theta$ determined by

- Demanding the central tracking chambers are used in the barrel region. Events where there are too few CV stereo/CJ hits are rejected.

- Demanding the central tracking chamber measurement is used for barrel and endcap region regardless of the number of hits in the chambers.

- Using the standard method with the additional constraint that both tracks have at least 3 hits in both the stereo CV wires and in CZ.

Because of the low statistics of the data, the Monte Carlo is assumed to be a good model for the data and is used to estimate the systematic error for these effects. The measured asymmetry only covers the range $|\cos\theta| < 0.95$ and it has to be corrected to the full angular range. This is achieved by assuming the Standard Model and scaling the asymmetry by a factor predicted from ZFITTER. The scaling factors for each energy are given in table 5.5. Also given are the corresponding scaling factors that are applied to correct the τ pair asymmetry to the full angular range from the measured asymmetry range of $|\cos\theta| < 0.9$.

The measured and predicted Standard Model asymmetries are given in table 5.6 and shown in figure 5.13. Given the limited statistics at each energy there is good agreement between data and Monte Carlo although the overall trend is for the measurements to be slightly below the Standard Model prediction. The method used to obtain the asymmetry was checked using the Monte Carlo sample as though it were data. The 189 GeV μ pair Monte Carlo sample was split into two halves. The first half was used to obtain the efficiency in each bin and the second half was used to obtain the angular distribution for the selected events. This distribution was corrected for feedthrough (there is no background arising from other physics processes), selection efficiency and corrected to the full solid angle. The procedure

	$s'/s > 0.01$		$s'/s > 0.7225$	
$\sqrt{s}$ GeV	$\mu^+\mu^-$	$\tau^+\tau^-$	$\mu^+\mu^-$	$\tau^+\tau^-$
130	0.997	1.013	1.027	1.059
136	0.994	1.008	1.027	1.059
161	0.978	0.984	1.027	1.059
172	0.974	0.979	1.027	1.058
184	0.971	0.975	1.027	1.058
189	0.969	0.973	1.027	1.058

Table 5.5: The scaling factor obtained from ZFITTER used to correct the measured asymmetries to the full solid angle from $|\cos\theta| < 0.95$ for the μ pairs and $|\cos\theta| < 0.9$ for the τ pairs.

was then repeated using the first half to obtain the angular distribution and the second half to obtain the efficiency. The resulting asymmetries for the inclusive sample are 0.283 ± 0.006 and 0.284 ± 0.006, which are in good agreement with the Standard Model prediction of 0.279. For the non-radiative sample the resulting asymmetries are 0.572 ± 0.007 and 0.566 ± 0.007. Again these are in good agreement with the Standard Model prediction of 0.566 and so no bias is seen in the method used to measure the asymmetry.

The asymmetries for this channel obtained by the other LEP experiments are consistent with those presented here and with the Standard Model prediction. Again the deviations of the individual measurements from the Standard Model show a reasonable scatter indicating that the fluctuations are consistent with been statistical.

	$\sqrt{s}$ GeV	Raw Data N_F	Raw Data N_B	Corrected Data N_F	Corrected Data N_B	A_{FB}	A_{FB}^{SM}
$s'/s > 0.01$	130.12	114	65	126.72	75.48	$0.25\ ^{+0.10}_{-0.19} \pm 0.01$	0.29
	136.07	148	87	167.11	106.66	$0.22\ ^{+0.09}_{-0.15} \pm 0.00$	0.29
	161.34	117	78	128.94	93.18	$0.16\ ^{+0.10}_{-0.18} \pm 0.01$	0.28
	172.08	88	61	94.99	73.98	$0.12\ ^{+0.11}_{-0.22} \pm 0.01$	0.28
	182.68	460	244	504.21	289.09	$0.26\ ^{+0.05}_{-0.07} \pm 0.01$	0.28
	188.66	559	289	630.79	349.33	$0.28\ ^{+0.05}_{-0.07} \pm 0.02$	0.28
$s'/s > 0.7225$	130.12	51	23	52.64	23.83	$0.39\ ^{+0.15}_{-0.36} \pm 0.02$	0.70
	136.07	89	17	94.47	17.63	$0.70\ ^{+0.09}_{-0.25} \pm 0.02$	0.68
	161.34	61	20	62.40	20.66	$0.52\ ^{+0.13}_{-0.33} \pm 0.02$	0.61
	172.08	49	18	48.89	18.81	$0.46\ ^{+0.15}_{-0.39} \pm 0.02$	0.59
	182.68	255	77	256.26	78.93	$0.54\ ^{+0.07}_{-0.12} \pm 0.02$	0.57
	188.66	308	105	317.67	110.19	$0.50\ ^{+0.06}_{-0.11} \pm 0.02$	0.57

Table 5.6: The measured asymmetries for μ pair events at each energy after correcting for the small effect from initial/final- state radiation interference. Shown are the raw number of events in the forward and backward hemispheres, the background and efficiency corrected number of events in the forward and backward hemispheres, the measured asymmetry and the Standard Model prediction. The first error is statistical and the second systematic. The systematic error for the $\mathrm{s}'/\mathrm{s} > 0.01$ selection at 136 GeV is too small for the quoted precision.

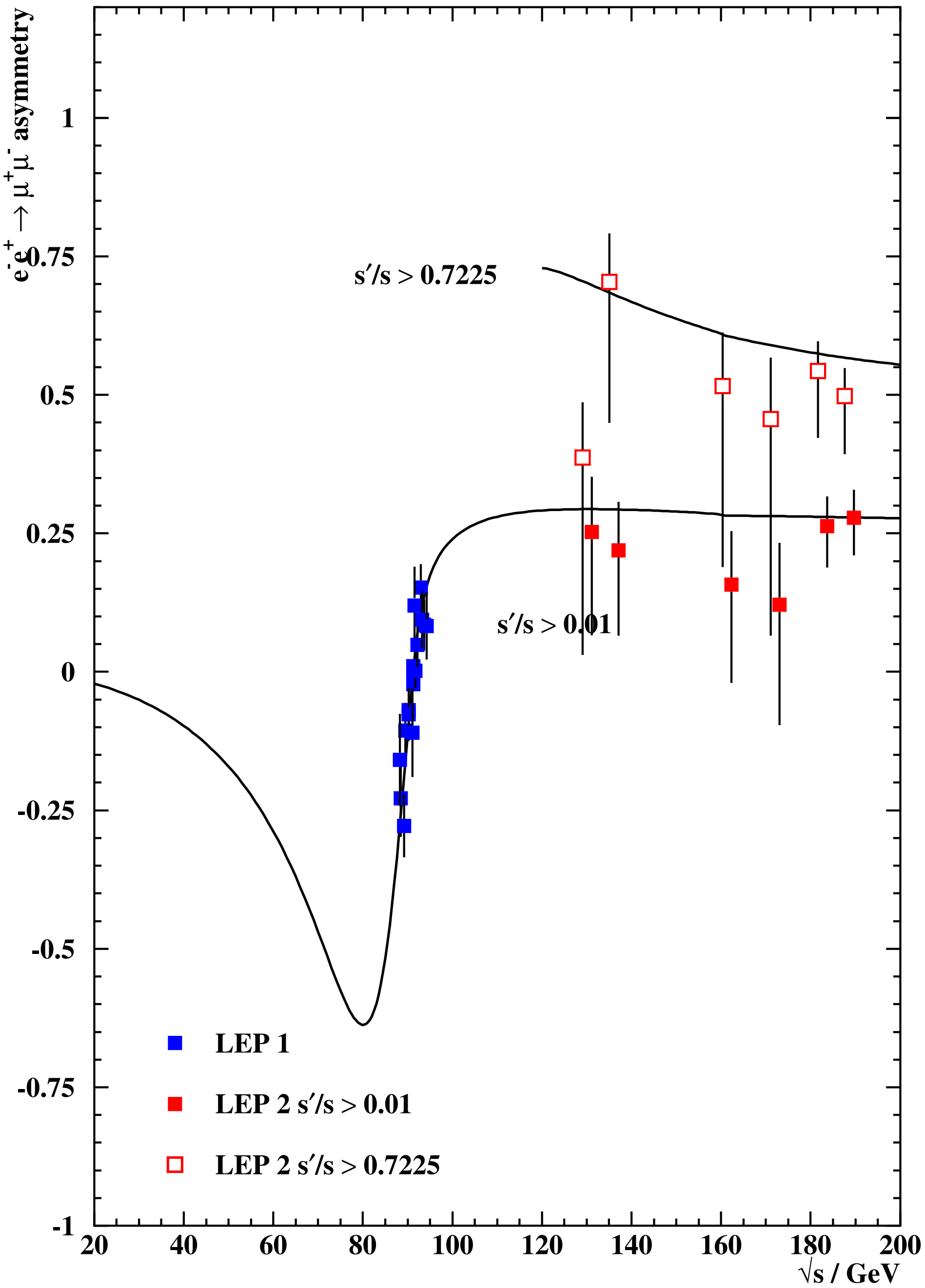

Figure 5.13: The measured asymmetry for $e^+e^- \rightarrow \mu^+\mu^-$ as a function of $\sqrt{s}$ showing the results taken at LEP1 [51] and the results obtained in the analyses for $\mathrm{s}'/\mathrm{s} > 0.7225$ and $\mathrm{s}'/\mathrm{s} > 0.01$ selections. The points at each energy have been separated for clarity. The solid lines are the ZFITTER prediction for the Standard Model asymmetry.

Chapter 6

Study of Tau Pair Events

6.1 Monte Carlo Studies

The analysis of the τ pairs is complicated by the short lifetime (≈ 291 fs) of the τ. This means only the products of the decay can be detected. Additionally, its many decay modes (to the other charged leptons and to the lightest quarks), all produce undetectable ν's which carry away some energy. This makes the identification of τ pairs much more difficult than that of μ pairs.

6.1.1 Event Selection

As with the μ pairs, the original selection used at LEP2 to identify τ pairs is based on that used for the LEP1 analysis, however many more modifications have been made during the continuing analysis to improve the selection efficiency and reduce the increased background due to the new processes involved, such as W pair production. The case where both W's decay leptonically looks similar to τ pair production as all that is detected are particles which could be the τ decay products with missing energy in the event.

After the initial lepton pair preselection described in section 4.1, an event is selected as a τ pair candidate if it satisfies the following conditions:

The identification of a τ in the event is made using a cone algorithm. Here, the highest energy track in the event is assigned a cone with a half-angle of 15°. This track is then combined with the next highest energy track or cluster within the cone and this combined track is assigned a new cone. This process is repeated until there are no more tracks or clusters within the cone and then begins with next highest energy track in the event and continues until there are no more tracks.

- There must be two cones in the event.

Additionally hadronic decays of the Z^0 can produce low multiplicity jets which could be confused with a hadronic τ decay. These are rejected by demanding N_{trk}, the number of tracks in the event, and $N_{tot} = N_{trk} + N_{cls}$, the total number of tracks and ECAL clusters (N_{cls}) in the event, be low. The probability that a τ will decay hadronically and produce 5 or more tracks is less than 0.1%. Hence, these requirements cleanly reject the multihadronic events leaving a high τ pair selection efficiency.

- $N_{trk} < 7$.

- $N_{tot} < 16$.

Rejecting the background from other sources is more difficult due to the similarities in the momentum, energies and particles which are detected. The background from μ pairs is rejected by vetoing events which pass the LEP1 μ pair selection described in the previous chapter[1].

- μ pair veto.

The much higher production cross-section of Bhabha events makes it difficult to reject them without significantly reducing the τ pair selection efficiency, so several cuts are used. The Bhabha asymmetry is higher than for the τ pairs due to the additional t-channel process. This results in relatively more events in the forward regions of the detector, so the $\cos\theta$ range for the tracks is restricted. In Bhabha events, where the missing energy is carried away by any initial-state radiation, the vector of the missing momentum is expected to be along the beampipe. For τ pair events the ν's arising from the decay provide additional components to the vector of missing momentum and so will shift this vector away from the beampipe. Hence

[1]Many improvements could be made in future analyses by vetoing μ pairs using the LEP2 selection described in the previous chapter.

restricting the angle of the missing momentum helps reduce the amount of Bhabha background. As the measurement of the track momentum becomes progressively poorer in the forward region the ECAL clusters are also used to calculate the cosine of the direction of missing momentum, $\cos\theta_{p^{ECAL}_{missing}}$. As electrons deposit all their energy in the ECAL, for Bhabha events the measured ECAL energy, $E_{cone(i)}$, divided by momentum, $p_{cone(i)}$ in cone i should be close to one for both cones and so the selection rejects such events.

- $|\cos\theta| < 0.9$ for both cones.
- $|\cos\theta_{p^{ECAL}_{missing}}| < 0.99$
- Events are rejected if $0.9 < \frac{E_{cone(i)}}{p_{cone(i)}} < 1.1$ for both cones

The acolinearity, θ_{acol}, is a measure of the back-to-backness of the event. It is defined as 180° - the angle between the particles.

The distribution of θ_{acol} for 130 and 189 GeV data and Monte Carlo is shown in figure 6.1(a) and (b) respectively. Each plot has two peaks, with the one near $\theta_{acol} = 0$ consisting mainly of the back-to-back non-radiative events. The second peak consists mainly of the boosted radiative return events and this peak shifts towards higher values of θ_{acol} as the boost increases. To obtain the largest efficiency for selecting these events, the cut on this function varies with $\sqrt{\mathrm{s}}$ to be just above the position of this peak.

The position of the cut is required to be slightly greater than the acolinearity calculated assuming that both τ's are emitted transversely to the momentum of the Z^0 from which they originate and that the Z^0 has been boosted by the emission of a single initial-state photon. This means

- $\theta_{acol} < 180° - 2\tan^{-1}\left(\frac{2\mathrm{M_Z}\sqrt{\mathrm{s}}}{\mathrm{s}-\mathrm{M_Z^2}}\right) + 10°$,

The value which the function of this cut takes for the range $100 < \sqrt{\mathrm{s}} < 200$ GeV is shown in figure 6.2.

In 4-fermion events the two τ candidates are not usually emitted from the same boson, hence the vector of their momentum need not lie in a plane. This allows them

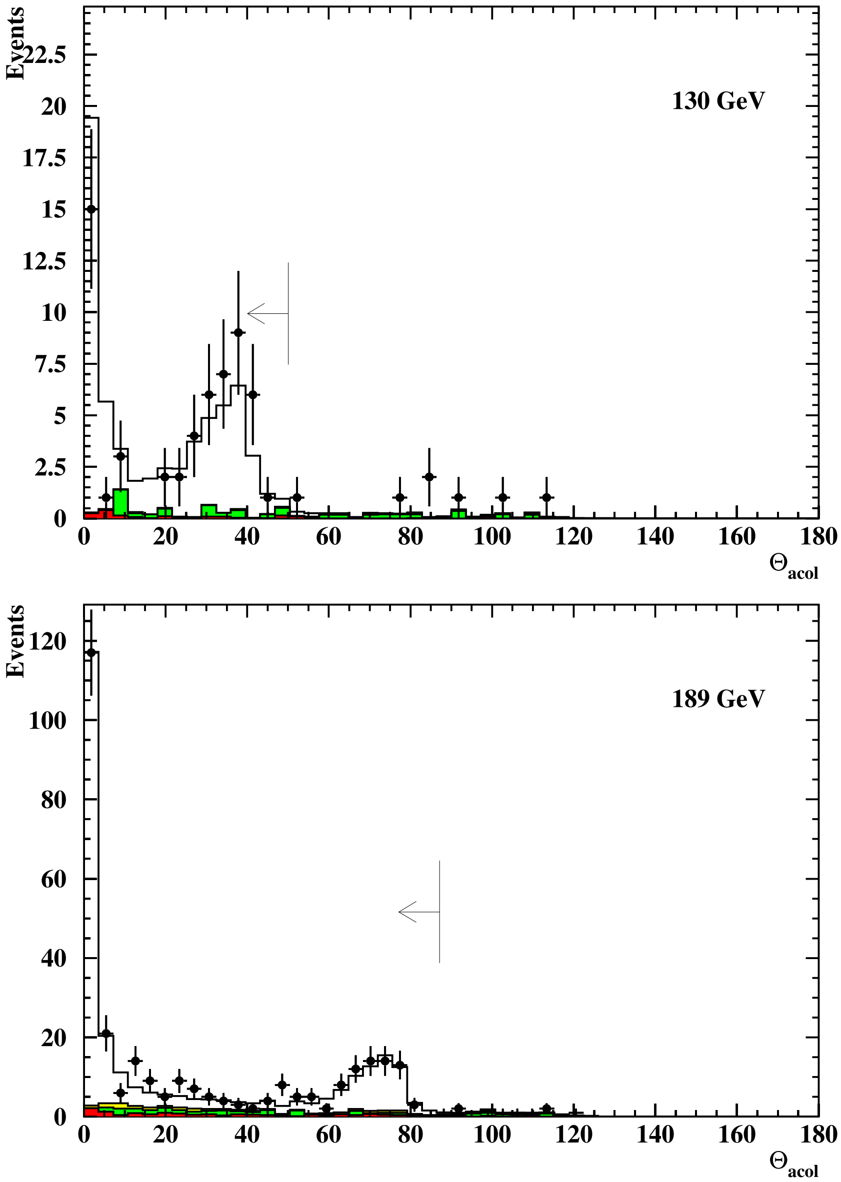

Figure 6.1: The distribution of the acolinearity, θ_{acol} between the two τ candidates before the cut on this quantity for the τ pair events at 130 GeV and 189 GeV.

The points represent the data and the histograms are the Monte Carlo prediction scaled to the integrated data luminosity. The open histogram is the τ pair Monte Carlo prediction and shaded histograms are the predicted background contributions. The arrow shows which events are selected.

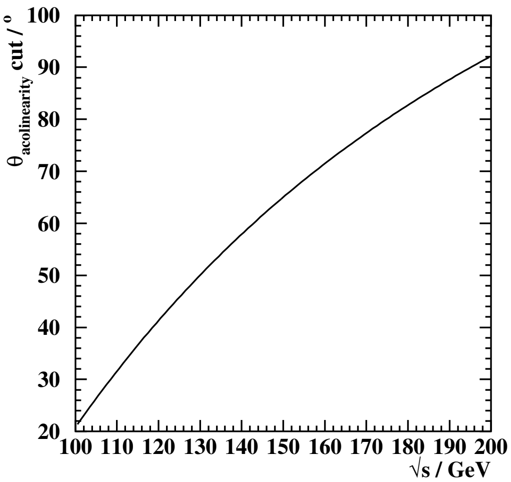

Figure 6.2: The position of the cut on the acolinearity, θ_{acol} between the two τ candidates as a function of $\sqrt{s}$ for all energies between 100 and 200 GeV.

to be rejected by restricting the acoplanarity, θ_{acop}, defined as 180°- angle between particles in the x-y plane.

- $\theta_{acop} < 30°$

For centre-of-mass energies above the W^+W^- production threshold a W pair veto is applied. This veto uses the standard OPAL W pair selection [44, 55].

- W pair veto

Cuts on the measured energy in the event allow additional rejection of many background processes. Figure 6.3(a) shows the distribution of R_{shw}, the total ECAL energy divided by $\sqrt{s}$, against R_{trk}, the total track momentum divided by $\sqrt{s}$, after all other cuts except those on energy (either ECAL energy or track momentum) for the 184 GeV τ pair Monte Carlo sample. The medium grey points represent the events and the lines represent the positions of the cuts on these variables as listed below. Also indicated is the region where events are accepted.

- $0.02 < R_{shw} < 0.7$. Shown by the two horizontal lines.

- $R_{trk} < 0.8$. Shown by the vertical line.

- $R_{vis} = R_{shw} + R_{trk} < 1.1$. Shown by the diagonal line.
- $R_{shw} > 0.2$ OR $R_{trk} > 0.2$. Shown by the box near the origin.

The events are clustered in the low to medium energy regions of both R_{shw} and R_{trk}. This is the region where events are accepted.

Figure 6.3(b) shows the same distribution for the 184 GeV μ pair Monte Carlo sample. Many μ pair events are already rejected by the μ pair veto. The remaining events are clustered in two regions, both with low R_{shw}. The cluster of events with medium R_{trk} consist of the events which have radiatively returned to the Z^0. The second cluster at higher R_{trk} are the non-radiative events which are rejected.

Figure 6.3(c) shows the same distribution for the 184 GeV Bhabha Monte Carlo sample. These events are clustered at high R_{shw} and R_{trk}. The majority of these events are rejected with little effect on the τ pair selection efficiency, however as this is such a major background the additional cut on R_{vis} is used to reject many more events at the cost of some efficiency.

Figure 6.3(d) shows the same distribution for all the 184 GeV two-photon Monte Carlo samples listed in table 4.1. These events are clustered in the low R_{shw} and R_{trk} region and are rejected by the requirement $R_{shw} > 0.2$ OR $R_{trk} > 0.2$. However this cut also rejects τ pair events and hence there is a significant reduction in the selection efficiency.

As two-photon events typically have low transverse momentum a further cut on the sum of the transverse momentum calculated using the energy deposited in the ECAL, $PTCLS$, helps in the rejection.

- $PTCLS > 0.015\sqrt{\mathrm{s}}$

These cuts significantly reduce the background while leaving good selection efficiency, however a further reduction in the background is achieved using a variable similar to that used by DELPHI [53]. Here the measured ECAL and track energies in the two cones are compared to what would be expected given the angles of cones and assuming a single initial-state photon emitted down the beampipe.

The expected energy in cone i, $R_{cone(i)}$ is determined using a modified version of

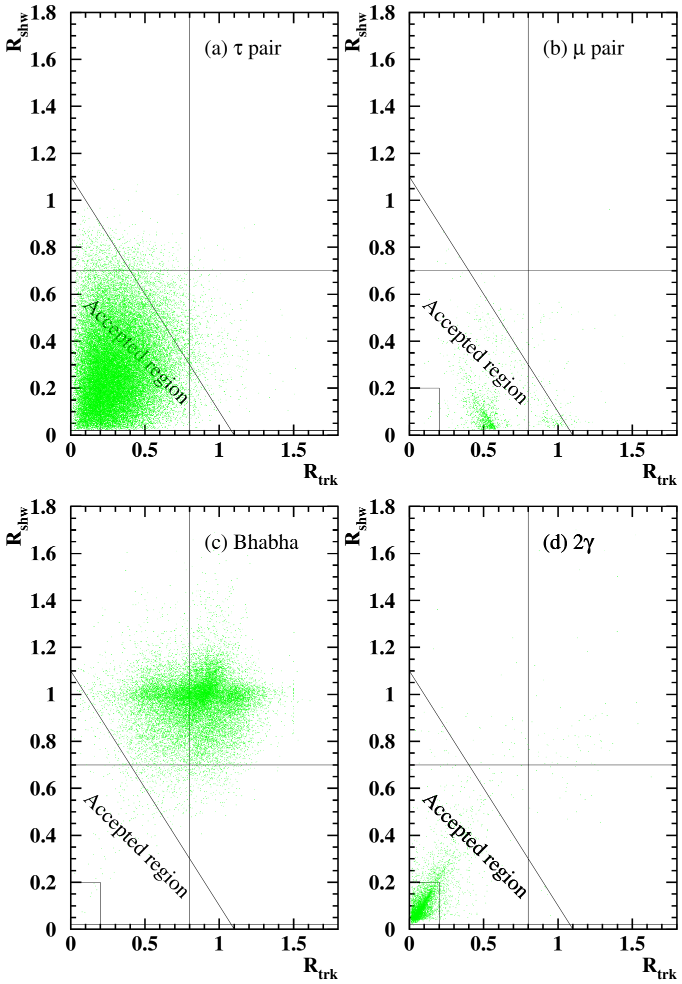

Figure 6.3: The distributions of R_{shw} against R_{trk} for 184 GeV Monte Carlo samples.

a) The τ pair Monte Carlo.

b) The μ pair Monte Carlo.

d) The Bhabha Monte Carlo.

d) The two-photon Monte Carlos.

In all plots the points represent the predicted distribution and the lines represent the positions of the cuts used. The accepted region is also indicated.

formula 4.2.

$$R_{cone(i)} = \sqrt{\mathrm{s}}\frac{|\sin\theta_i|}{|\sin(\theta_1+\theta_2)|+\sin\theta_1+\sin\theta_2} \tag{6.1}$$

where θ_i is the angle of cone i. For a Bhabha background event the measured ECAL energy in both cones should be close to that which is expected. For a μ pair background event the measured ECAL energy should be low. In both cases the measured track momentum in both cones should be close to that which is expected. This leads to the following additional cuts.

- $0.02 < \sqrt{\frac{E^2_{cone(1)}+E^2_{cone(2)}}{R^2_{cone(1)}+R^2_{cone(2)}}} < 0.8$, where
- $\sqrt{\frac{p^2_{cone(1)}+p^2_{cone(2)}}{R^2_{cone(1)}+R^2_{cone(2)}}} < 0.8$.

6.1.2 Efficiency, Feedthrough and Background

The τ pair selection described in the previous section is applied to the various Monte Carlo samples used at each energy to give the efficiency, feedthrough and backgrounds given in table 6.1.

Efficiency

Due to the extra difficulties in identifying a pure sample of τ pair events, the selection efficiencies are lower than those for the μ pair analyses. The inclusive efficiency is lower for the analyses at energies above 161 GeV due to the introduction of the W pair veto. This effect is not seen in the non-radiative selection efficiency, which remains relatively constant, due to the s$'$/s requirement that the tracks are back-to-back.

As with the μ pairs the systematic error on the efficiency was determined using the LEP1 Z peak data and relaxing any cuts which eat into the Z peak.

Feedthrough

Compared to the μ pairs the feedthrough is approximately 2.5 times higher at 130 GeV, decreasing to 1.25 times higher at 189 GeV. The decreasing ratio between the μ pair and τ pair feedthrough is due to the ν's emitted during the decay of the τ's.

	$\sqrt{s}$ GeV	Efficiency %	Background pb	Feedthrough pb
$s'/s > 0.01$	130.12	$49.03 \pm 0.36 \pm 1.21$	$1.065 \pm 0.186 \pm 0.088$	N/A
	136.07	$47.97 \pm 0.36 \pm 1.18$	$0.974 \pm 0.170 \pm 0.080$	
	161.34	$43.41 \pm 0.16 \pm 1.07$	$0.624 \pm 0.061 \pm 0.084$	
	172.08	$41.69 \pm 0.16 \pm 1.03$	$0.671 \pm 0.060 \pm 0.108$	
	182.68	$40.35 \pm 0.16 \pm 0.99$	$0.612 \pm 0.023 \pm 0.097$	
	188.66	$40.36 \pm 0.18 \pm 0.99$	$0.583 \pm 0.034 \pm 0.111$	
$s'/s > 0.7225$	130.12	$58.71 \pm 0.58 \pm 1.44$	$0.465 \pm 0.134 \pm 0.042$	$0.617 \pm 0.027 \pm 0.097$
	136.07	$59.10 \pm 0.57 \pm 1.45$	$0.425 \pm 0.123 \pm 0.038$	$0.366 \pm 0.018 \pm 0.048$
	161.34	$59.12 \pm 0.25 \pm 1.45$	$0.200 \pm 0.035 \pm 0.022$	$0.159 \pm 0.004 \pm 0.011$
	172.08	$59.06 \pm 0.25 \pm 1.45$	$0.218 \pm 0.033 \pm 0.036$	$0.121 \pm 0.004 \pm 0.009$
	182.68	$58.94 \pm 0.25 \pm 1.45$	$0.221 \pm 0.014 \pm 0.038$	$0.085 \pm 0.003 \pm 0.001$
	188.66	$58.46 \pm 0.27 \pm 1.44$	$0.188 \pm 0.020 \pm 0.037$	$0.073 \pm 0.003 \pm 0.001$

Table 6.1: The predicted efficiency, feedthrough and background for the τ pair analysis at each energy. The first error is statistical and the second systematic.

Consider the case where the τ decays hadronically. In this decay one ν is emitted and the hadronic decay products receive a boost of up to ≈ 1 GeV transverse to the momentum vector of the original τ. This boost is relative to the original momentum of the τ and so at the higher energies the maximum change in the angle is smaller, hence is closer to that which would be obtained in the equivalent μ pair event.

The systematic error on the feedthrough is obtained in the same way as for the μ pair analysis described in section 5.1.3.

Background

The cross-section of the background events in the inclusive sample decreases as $\sqrt{s}$ increases, but not as fast as the τ pair cross-section. This results in the background increasing from 9% of all events at 130 GeV to 16% at 189 GeV. The most important background sources are Bhabha events (20%), two photon $e^+e^-e^+e^-$ (30%) and $e^+e^-\tau^+\tau^-$ (15%) events and $l^+l^-l^+l^-$ events (15%).

The background cross-section for the non-radiative selection decreases at a similar rate to the τ pair cross-section and so accounts for a constant percentage (9%) of the total number of selected events. The same processes dominate although the contribution from two-photon events is reduced by the requirement that the τ candidates are back-to-back.

The predicted background cross-sections for the 189 GeV analysis are shown in table 6.2. Again the systematic error on the background cross-section is determined by loosening the cuts which are important for rejecting the background under study and comparing the predicted number of events from the Monte Carlo samples to the total number of data events in the region where the background is dominant.

Figure 6.4 illustrates this for the $\mu^+\mu^-$ background process. The plot shows the R_{vis} distribution after all other cuts, except those on energy (ECAL or track) and the μ pair veto, for all energies combined. In the region indicated by the arrows there are 270 data events, the Monte Carlo predicts that there should be a total of 285 events in this region. The discrepancy of approximately 15 events equates to a 5.6% error, however, here the statistical precision on the number of data events is 6.1%, and it is this value which was used for the systematic error on the $\mu^+\mu^-$

		$\mathrm{s}'/\mathrm{s} > 0.7225$ $\sigma(pb)$	$\mathrm{s}'/\mathrm{s} > 0.01$ $\sigma(pb)$	systematic %
2-fermion	$\tau^+\tau^-$	0.073 ± 0.003	N/A	-
	$\mu^+\mu^-$	0.0120 ± 0.0011	0.051 ± 0.002	6.1
	e^+e^-	0.049 ± 0.012	0.12 ± 0.02	11.1
	$q\bar{q}$	0.0028 ± 0.0008	0.017 ± 0.002	23.8
2γ	$e^+e^-q\bar{q}$(tagged)	0.002 ± 0.002	0.002 ± 0.002	3.2
	$e^+e^-e^+e^-$	0.041 ± 0.013	0.132 ± 0.02	3.2
	$e^+e^-\mu^+\mu^-$	0	0.009 ± 0.005	3.2
	$e^+e^-\tau^+\tau^-$	0.025 ± 0.007	0.083 ± 0.013	3.2
4-fermion	$e^+e^-q\bar{q}$	0.0014 ± 0.0005	0.015 ± 0.002	50
	$e^+e^-e^+e^-$	0.0020 ± 0.0007	0.0059 ± 0.0011	50
	$e^+e^-\mu^+\mu^-$	0.0024 ± 0.0007	0.013 ± 0.002	50
	$e^+e^-\tau^+\tau^-$	0.0036 ± 0.0009	0.030 ± 0.002	50
	$q\bar{q}q'\bar{q}'$	0.0004 ± 0.0003	0.0004 ± 0.0003	50
	$l^+l^-q\bar{q}$	0.0026 ± 0.0007	0.0076 ± 0.0012	50
	$l^+l^-l^+l^-$	0.044 ± 0.003	0.095 ± 0.004	50

Table 6.2: The Monte Carlo predicted background for the 189 GeV τ pair selection showing the Monte Carlo process, the background cross-section for the $\mathrm{s}'/\mathrm{s} > 0.7225$ and $\mathrm{s}'/\mathrm{s} > 0.01$ selections and the percentage systematic errors that are applied to the predicted cross-section.

background Monte Carlo for all energies.

The poor agreement between the data and Monte Carlo seen in Bhabha dominated region (dark grey histogram) of figure 6.4 is accounted for in the background systematic applied to the Bhabha Monte Carlo sample. To check that no bias was introduced by this disagreement, the predicted number of Bhabha events was scaled up by 20%, and the analysis repeated for the 189 GeV data. The resulting changes to the measured cross-sections and asymmetries were less than 10% of the assigned systematic error.

6.1.3 Comparison with other LEP experiments

The selection efficiencies obtained in the analyses presented in this thesis are approximately 10-15% higher than those obtained in a similar analyses performed by the L3 experiment, also the background contamination in the L3 analysis is 2-4% higher at 130 GeV increasing to almost twice as high at 172 GeV than those in this thesis. The feedthrough background is comparable.

The selection efficiencies in the ALEPH analyses are generally a few percent higher than those in this thesis. Although the background for the $s'/s > 0.01$ sample are also a few percent lower than those obtained here, the backgrounds in the $s'/s > 0.7225$ selection[2] are a few percent higher. Again ALEPH do not quote a value for the feedthrough.

The DELPHI analyses typically have a selection efficiency for the $\sqrt{s'} > 75$ GeV sample which is 2-5% smaller than those for the $s'/s > 0.01$ sample in this thesis. For the $s'/s > 0.7225$ sample the selection efficiency is typically 13% smaller. The background contamination of both the $s'/s > 0.7225$ and $s'/s > 0.01$ samples are between 1.5 and 2 times higher than those quoted in this thesis. The feedthrough background at 130 GeV is lower that obtained in this thesis, however for 172 GeV it is nearly twice as large.

[2] ALEPH use $s'/s > 0.81$ and scale to $s'/s > 0.7225$

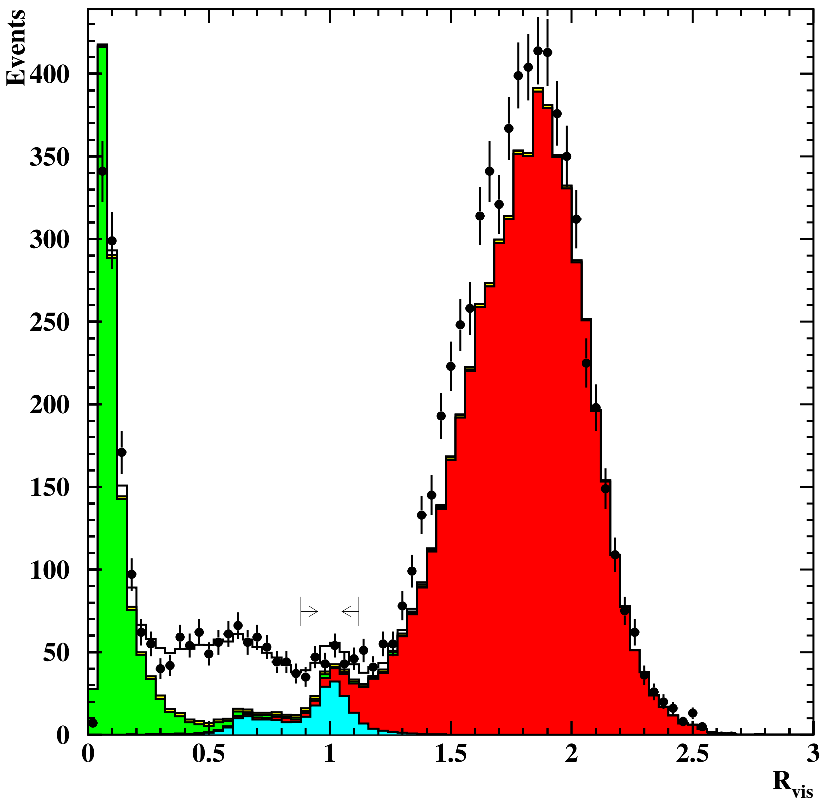

Figure 6.4: The R_{vis} distribution for all energies combined.

The points represent the data and the histograms are the Monte Carlo prediction scaled to the integrated data luminosity. The open histogram is the τ pair Monte Carlo prediction, the light grey histogram is the background from the $\mu^+\mu^-$ process, the dark grey histogram is the background from other 2-fermion process and the medium grey histogram is the predicted background contribution from two photon $e^+e^-f\bar{f}$ processes. The arrows indicate the region in which the number of events from data and Monte Carlo are compared.

6.2 Data

The τ pair selection described in the previous selection was applied to the data taken at each energy to measure the cross-sections, angular distributions and asymmetries.

The $\sqrt{s'}$ distribution for the sample at each energy are shown in figures 6.5 and 6.6. The full energy and radiative return peaks can clearly be seen and there is generally good agreement between data and Monte Carlo. The discrepancies between the data and Monte Carlo in the radiative return peaks for the 130, 136 and 172 GeV data were studied to verify the measurement. These checks revealed no apparent problems and so we assume these are statistical fluctuations in the low statistic data sets.

6.2.1 Cross-section

The cross-sections are determined for the inclusive and non-radiative τ pair selections in the same way as for the μ pair cross-sections. They are tabulated in table 6.3 and shown in figure 6.7. The measured cross-sections are scattered close to the ZFITTER prediction at each energy.

The breakdown for the systematic errors for 189 GeV are given in table 5.4 of the previous chapter. The dominant systematic uncertainties come from the systematic errors on the selection efficiencies and backgrounds. Once again the statistical error dominates the systematic error.

As with the μ pair analyses all four LEP experiments measure similar cross-sections which are in consistent with the Standard Model predictions. At 161 GeV all experiments see an excess of events, but this excess is still statistically consistent with the prediction. All experiments but DELPHI quote similar values for the systematic error of 3-4%, DELPHI quotes 7%.

6.2.2 Angular Distribution and Asymmetry

The uncorrected angular distributions of data and Monte Carlo events at each energy are shown for the $s'/s > 0.7225$ and $s'/s > 0.01$ τ pair selections in figures 6.8 and 6.9. Here the $\cos\theta$ used for the τ candidate is exactly the same as for the $\sqrt{s'}$ calculation.

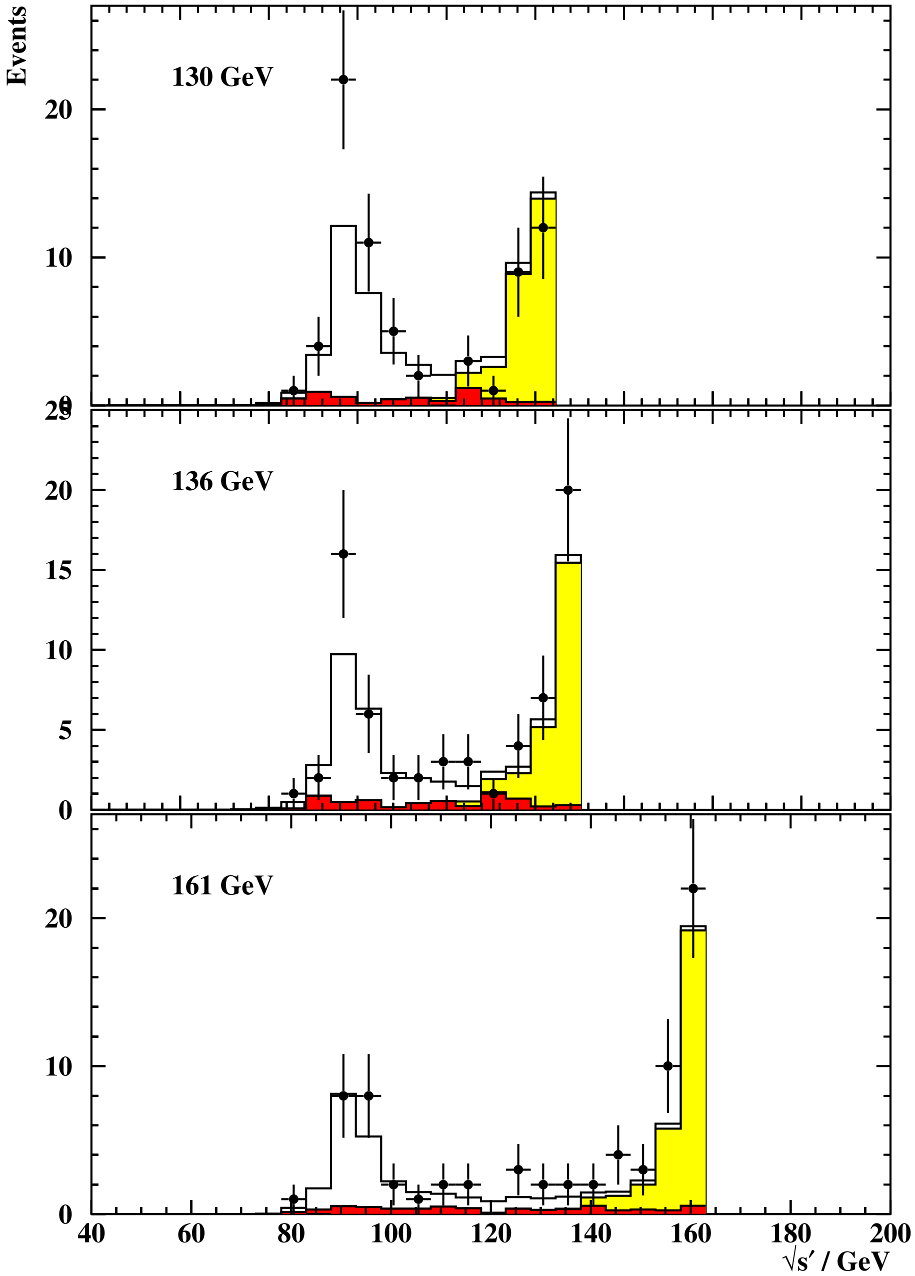

Figure 6.5: The $\sqrt{s'}$ distributions for the τ pair events at 130, 136 and 161 GeV. The points represent the data and the histograms are the Monte Carlo prediction scaled to the integrated data luminosity. The open histogram is the τ pair Monte Carlo prediction for the $s'/s > 0.01$ selection, the very light grey histogram is the Monte Carlo prediction for the true $s'/s > 0.7225$ events and dark grey histogram is the predicted background contribution.

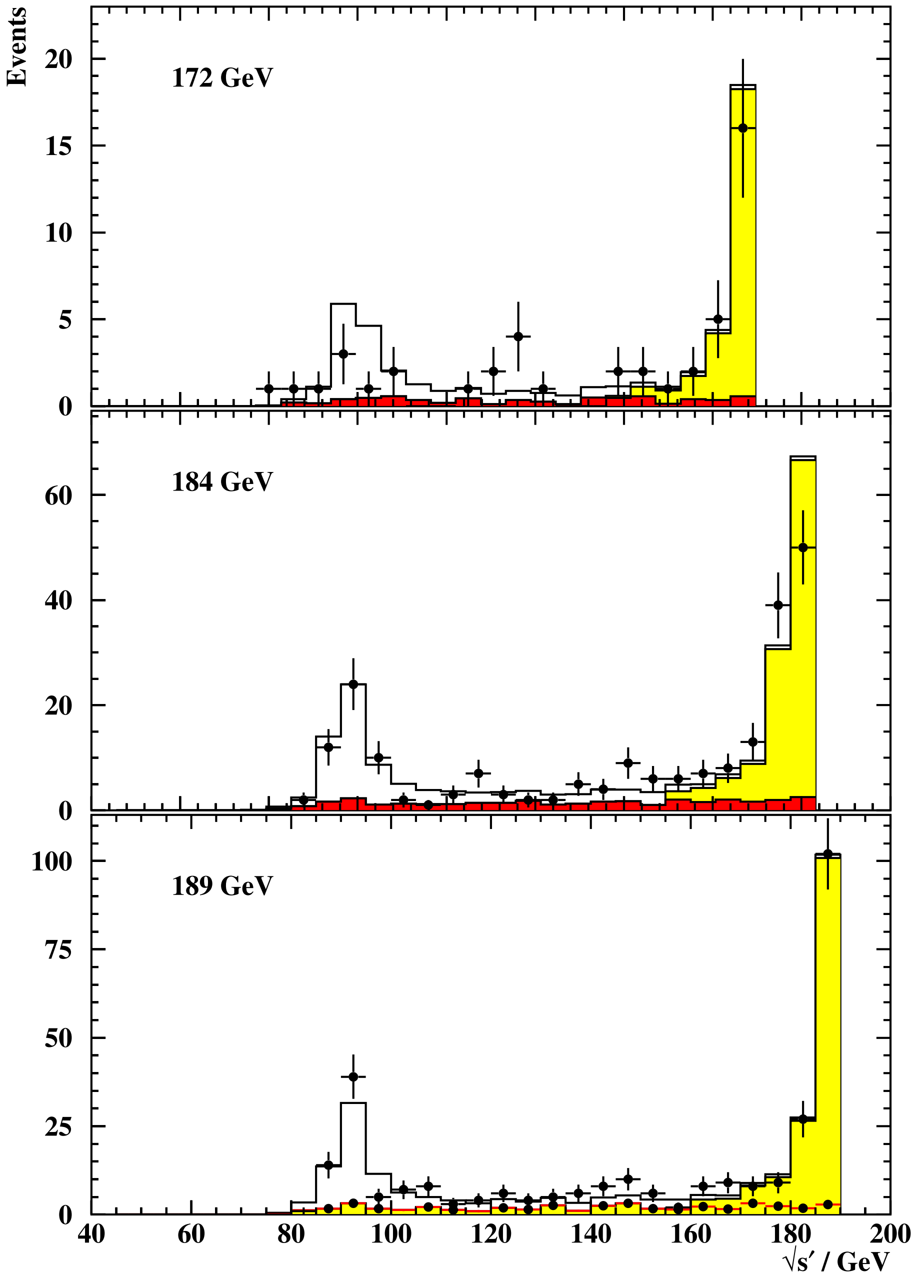

Figure 6.6: The $\sqrt{s'}$ distributions for the τ pair events at 172, 184 and 189 GeV. The symbols and shadings are the same as used in figure 6.5.

	$\sqrt{s}$ GeV	Selected Events	σ pb	σ^{SM} pb
$s'/s > 0.01$	130.12	70	$25.09 \pm 3.00 \pm 0.81$	22.09
	136.07	67	$21.40 \pm 2.62 \pm 0.71$	18.86
	161.34	72	$15.24 \pm 1.80 \pm 0.47$	11.25
	172.08	45	$9.02 \pm 1.35 \pm 0.38$	9.58
	182.68	215	$8.34 \pm 0.57 \pm 0.33$	8.30
	188.66	299	$8.48 \pm 0.49 \pm 0.36$	7.71
$s'/s > 0.7225$	130.12	25	$6.21 \pm 1.25 \pm 0.34$	8.46
	136.07	32	$7.68 \pm 1.36 \pm 0.32$	7.31
	161.34	41	$6.33 \pm 0.99 \pm 0.18$	4.62
	172.08	27	$3.90 \pm 0.75 \pm 0.13$	3.96
	182.68	123	$3.32 \pm 0.30 \pm 0.11$	3.45
	188.66	167	$3.35 \pm 0.26 \pm 0.11$	3.21

Table 6.3: The measured cross-sections for τ pair events at each energy after correcting for the small effect from initial/final- state radiation interference. Shown are the number of selected events, the measured cross-section and the ZFITTER prediction. The first error is statistical and the second systematic.

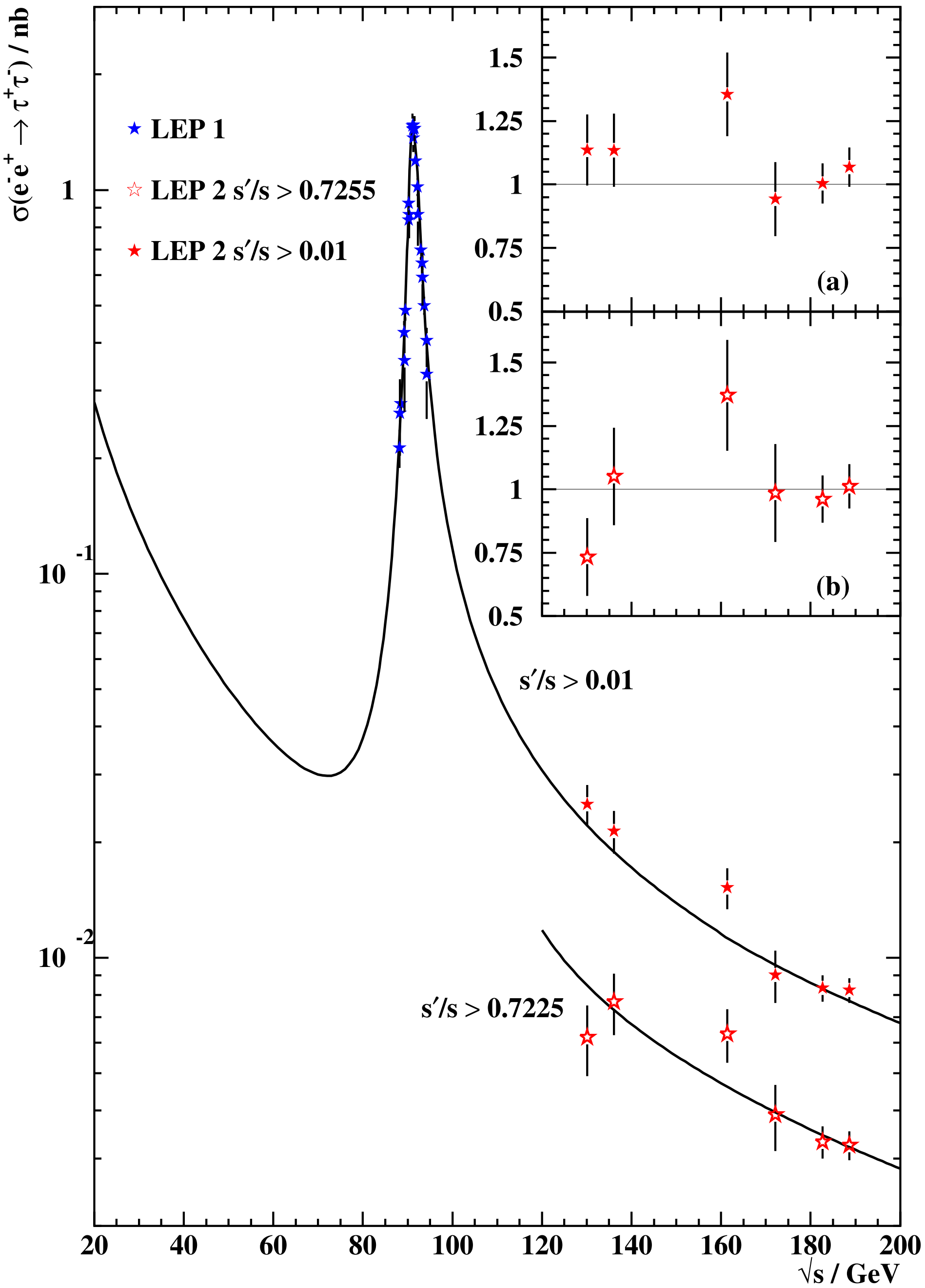

Figure 6.7: The measured cross-section for $e^+e^- \to \tau^+\tau^-$ as a function of $\sqrt{s}$ showing the results taken at LEP1 [51] and the results obtained in the analyses for $s'/s > 0.7225$ and $s'/s > 0.01$ selections. The solid lines are the ZFITTER prediction for the Standard Model cross-section. Inserts (a) and (b) show the ratio of the measured and predicted cross-sections for the $s'/s > 0.01$ and $s'/s > 0.7225$ selections.

Only events where the τ candidates are reconstructed as having opposite signed charges, one of which must have a charge of ± 1, are plotted. This leads to the rejection of roughly 4% of the total number of data events at all energies. This is consistent with the Monte Carlo prediction that approximately 2.5% of events will be rejected.

There is generally good agreement between the measured and predicted distributions. Many checks on the data were made and discrepancies between the data and Monte Carlo were determined to be statistical fluctuations. The $\mathrm{s}'/\mathrm{s} > 0.7225$ distribution is a subset of the $\mathrm{s}'/\mathrm{s} > 0.01$ distribution and so fluctuations in the same $\cos\theta$ bins at the same energy are correlated.

The measured angular distributions are corrected for background, initial/final-state radiation interference and selection efficiency. This is illustrated for the 184 GeV τ pair analysis in figures 6.10 and 6.11. First the $-q * \cos\theta$ distributions of the selected Monte Carlo events are divided into forty bins covering the full $\cos\theta$ range (figures 6.10(a) and (b)). For the non-radiative case only those events selected with a generated $\mathrm{s}'/\mathrm{s} > 0.7225$ are used. These distributions are compared to the generated $\cos\theta$ distribution for all Monte Carlo events (figures 6.10(c) and (d)) to obtain a bin by bin selection efficiency (figures 6.10(e) and (f)).

The distributions of the efficiencies are are similar to those obtained for the μ pair analysis(figures 5.11(e) and (f)), although naturally the overall efficiency is lower. The efficiency for the $\mathrm{s}'/\mathrm{s} > 0.01$ selection (figures 6.10(f)) is even less symmetric than for the inclusive μ pair efficiencies because, in the τ analysis, the efficiency for selecting the radiative events is significantly less than the non-radiative selection efficiency. Again this results in the overall selection efficiency for events in the backward region to be worse than for the forward region. The efficiency for the $\mathrm{s}'/\mathrm{s} > 0.7225$ selection (figure 6.10(e)) is generally symmetrical. In the backward region there is some fluctuation due to the lower statistics and, as the selection efficiency falls much more rapidly than for the μ pairs, the efficiency may be slightly lower than in the forward region.

The distributions of the selected data events (figures 6.11(a) and (b)) are first corrected for initial/final-state interference by adding the ZFITTER prediction for

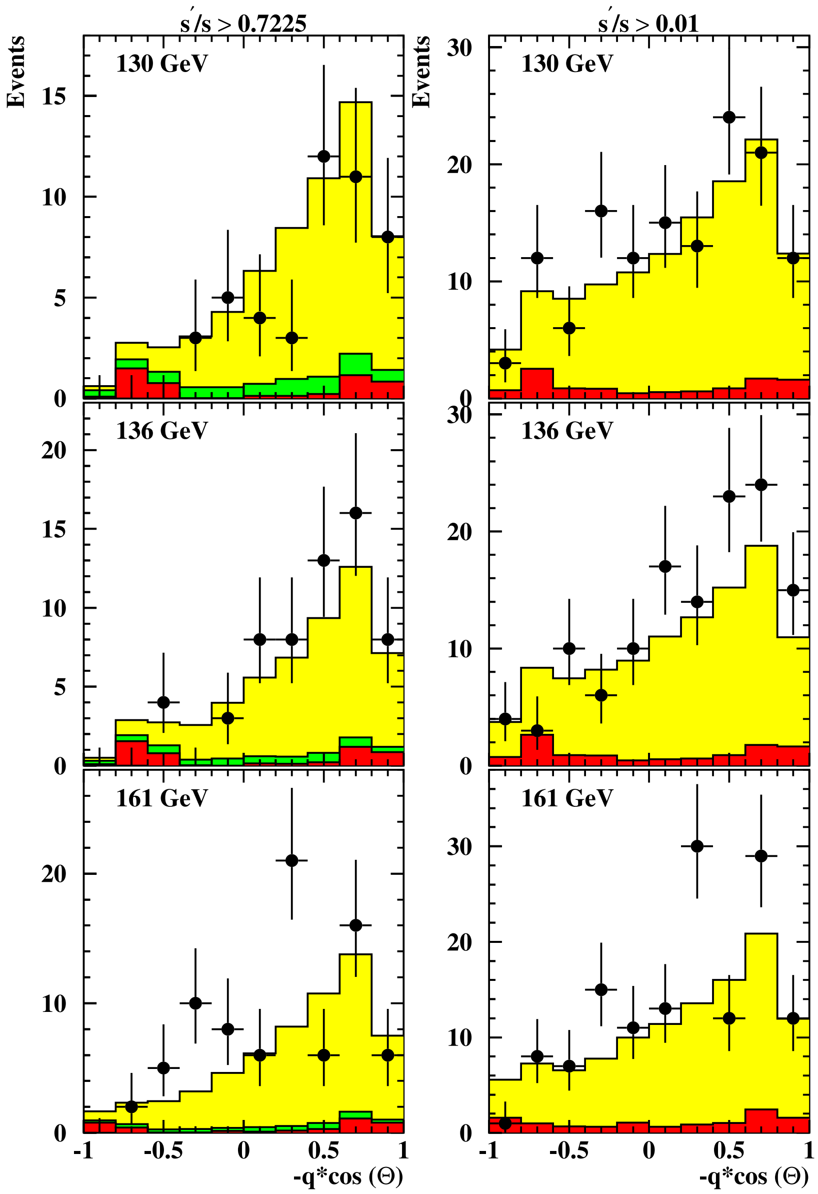

Figure 6.8: The combined negative and positive particle $-q * \cos\theta$ distributions obtained for the $\mathrm{s}'/\mathrm{s} > 0.7225$ and $\mathrm{s}'/\mathrm{s} > 0.01$ τ pair events at 130, 136 and 161 GeV.

The points represent the data, the error bars show the Poissonian statistical error and the histograms are the Monte Carlo prediction scaled to the integrated data luminosity. The very light grey histogram is the τ pair Monte Carlo prediction and the dark grey histogram is the predicted background contribution. The medium grey histogram is the expected contribution from feedthrough events for $\mathrm{s}'/\mathrm{s} > 0.7225$.

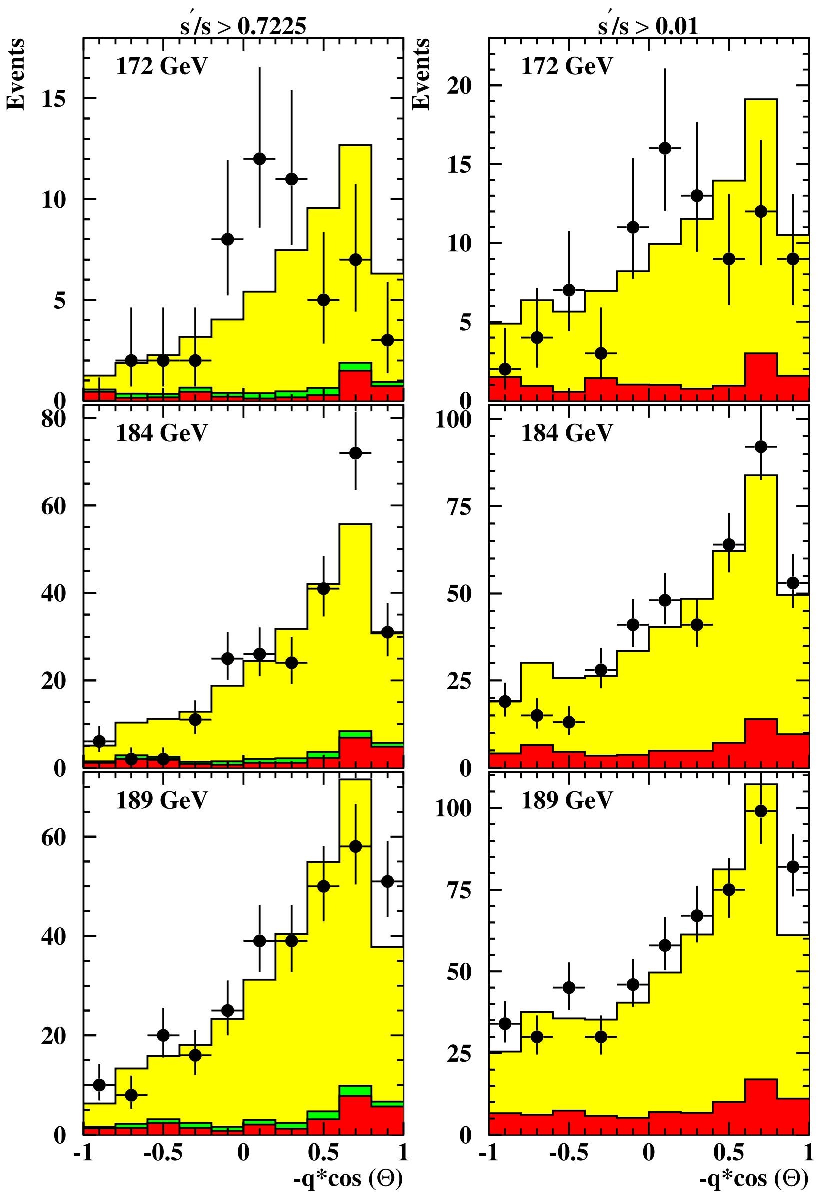

Figure 6.9: The combined negative and positive particle $-q * \cos\theta$ distributions obtained for the $\mathrm{s}'/\mathrm{s} > 0.7225$ and $\mathrm{s}'/\mathrm{s} > 0.01$ τ pair events at 172, 184 and 189 GeV. The symbols and shadings are the same as used in figure 6.8.

the number of events in the bin (figures 6.11(c) and (d)). The distribution of the correction in each bin is similar between the two samples, but the size of the correction is bigger for the non-radiative sample than for the inclusive sample. The background corrections are then made by subtracting the Monte Carlo prediction for the number of events passing the selections arising from other physics processes (medium grey histogram in figures 6.11(e) and (f)). In the case of the non-radiative selection, the Monte Carlo prediction for the number of feedthrough events (dark grey histogram in figure 6.11(f)) is also subtracted. Finally the distributions are corrected for the efficiency in each $\cos\theta$ bin and the corrected $\cos\theta$ distributions are shown in figures 6.11(g) and (h).

The main background in the large $|\cos\theta|$ regions for both the $\mathrm{s}'/\mathrm{s} > 0.7225$ and $\mathrm{s}'/\mathrm{s} > 0.01$ selections arise from the two-photon processes which tend to be close to the beam pipe. The forward region also has an additional contribution from the Bhabha events. The background in the central $\cos\theta$ region consist mainly of μ pair and $l^+l^-l^+l^-$ events.

The $-q * \cos\theta$ distributions for the negative and positive τ's are used to obtain the forward/backward asymmetries for the inclusive and non-radiative τ pair events using the same procedure as described in the previous chapter. The scaling factors, obtained using the ZFITTER predictions for the Standard Model asymmetries, which are applied to the measured asymmetry to correct it from the measured range of $|\cos\theta| < 0.9$ to the full solid angle are shown in table 5.5 of the previous chapter.

The systematic error on the asymmetry is determined by comparing the measured asymmetries when different methods are used to obtain the $\cos\theta$ of the lepton. The Monte Carlo is assumed to model the data well and is used to overcome the statistical limitation which would be encountered using the data for this study. In the τ pair analysis the different methods for obtaining the $\cos\theta$ use only the vector momentum or only the vector sum of the ECAL energy deposits to determine the $\cos\theta$.

The measured and ZFITTER predicted asymmetries are given in table 6.4 and shown in figure 6.12. Due to the low statistics the error on these measurements

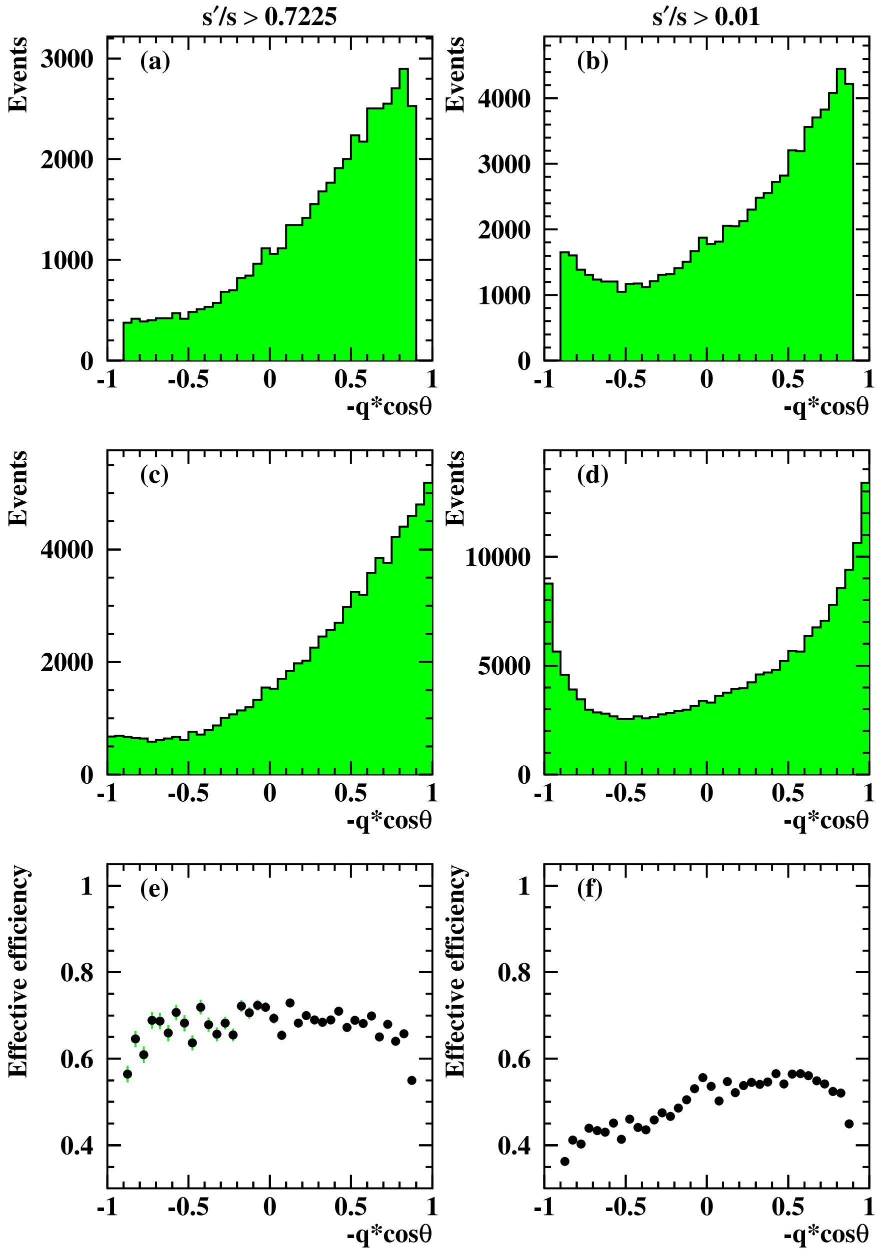

Figure 6.10: Distributions used in the determination of the efficiency for each $\cos\theta$ bin used in the calculation of the asymmetry for the τ pair analysis for $\mathrm{s}'/\mathrm{s} > 0.01$ and $\mathrm{s}'/\mathrm{s} > 0.7225$ events at 184 GeV.

(a) and (b) The $-q * \cos\theta$ distributions of the selected Monte Carlo events.

(c) and (d) The generated $-q * \cos\theta$ distribution of all Monte Carlo events.

(e) and (f) The resulting efficiencies for each $\cos\theta$ bin, here the error bars are statistical.

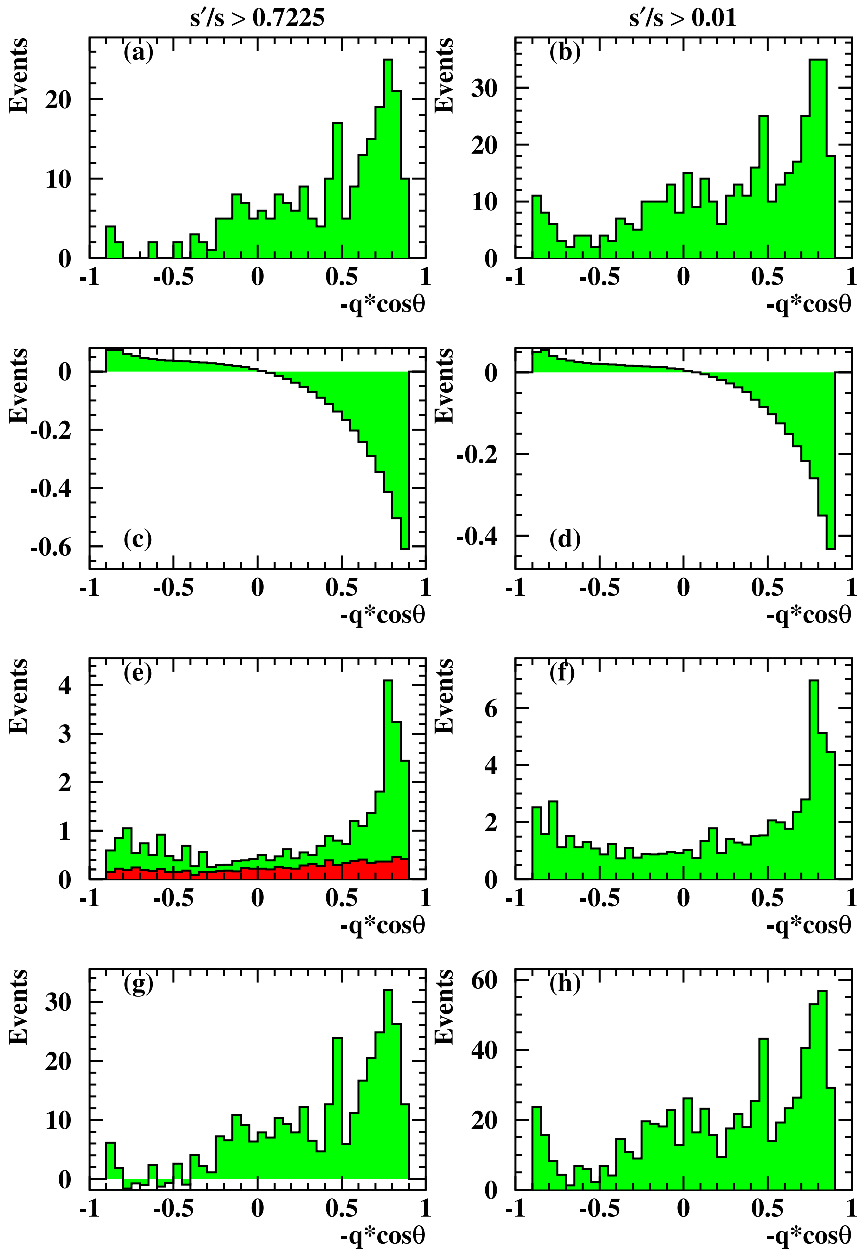

Figure 6.11: Distributions used in the calculation of the asymmetry for the τ pair analysis for $\mathrm{s}'/\mathrm{s} > 0.01$ and $\mathrm{s}'/\mathrm{s} > 0.7225$ events at 184 GeV.

(a) and (b) The $-q * \cos\theta$ distributions of selected data events.

(c) and (d) The $-q * \cos\theta$ distributions of the interference correction.

(e) and (f) The predicted Monte Carlo $-q * \cos\theta$ distributions of background events (medium grey) and feed-through events for $\mathrm{s}'/\mathrm{s} > 0.7225$ (dark grey).

(g) and (h) The corrected $-q * \cos\theta$ distributions of data events.

are very large. However, the measurements are consistent with the Standard Model predictions, as are the preliminary and published measurements of all four LEP experiments [52, 53, 54].

	$\sqrt{s}$ GeV	Raw Data N_F	Raw Data N_B	Corrected Data N_F	Corrected Data N_B	A_{FB}	A_{FB}^{SM}
$s'/s > 0.01$	130.12	85	49	129.27	78.41	$0.25\ ^{+0.13}_{-0.26} \pm 0.00$	0.29
	136.07	93	33	146.98	50.28	$0.49\ ^{+0.12}_{-0.28} \pm 0.00$	0.29
	161.34	96	42	157.97	75.48	$0.35\ ^{+0.12}_{-0.25} \pm 0.00$	0.28
	172.08	59	27	93.88	46.51	$0.33\ ^{+0.16}_{-0.38} \pm 0.01$	0.28
	182.68	298	116	478.68	205.10	$0.39\ ^{+0.07}_{-0.12} \pm 0.01$	0.28
	188.66	395	187	653.47	354.29	$0.29\ ^{+0.06}_{-0.10} \pm 0.01$	0.28
$s'/s > 0.7225$	130.12	38	8	46.09	3.90	$0.89\ ^{+0.19}_{-0.70} \pm 0.05$	0.70
	136.07	53	7	69.45	4.02	$0.94\ ^{+0.13}_{-0.48} \pm 0.05$	0.68
	161.34	55	25	72.63	32.28	$0.41\ ^{+0.15}_{-0.38} \pm 0.05$	0.61
	172.08	38	14	47.60	17.25	$0.50\ ^{+0.19}_{-0.54} \pm 0.04$	0.59
	182.68	194	46	252.27	54.43	$0.68\ ^{+0.08}_{-0.17} \pm 0.04$	0.57
	188.66	247	79	327.71	102.70	$0.55\ ^{+0.08}_{-0.13} \pm 0.04$	0.57

Table 6.4: The measured asymmetries for τ pair events at each energy after correcting for the small effect from initial/final- state radiation interference. Shown are the $\sqrt{s}$ energy, the raw number of events and the number of events after correcting for background and efficiency in the forward and backward hemispheres, the measured asymmetry and the Standard Model prediction. The first error is statistical and the second systematic. The systematic error for the $s'/s > 0.01$ selections at 130, 136 and 161 GeV are smaller than 0.005.

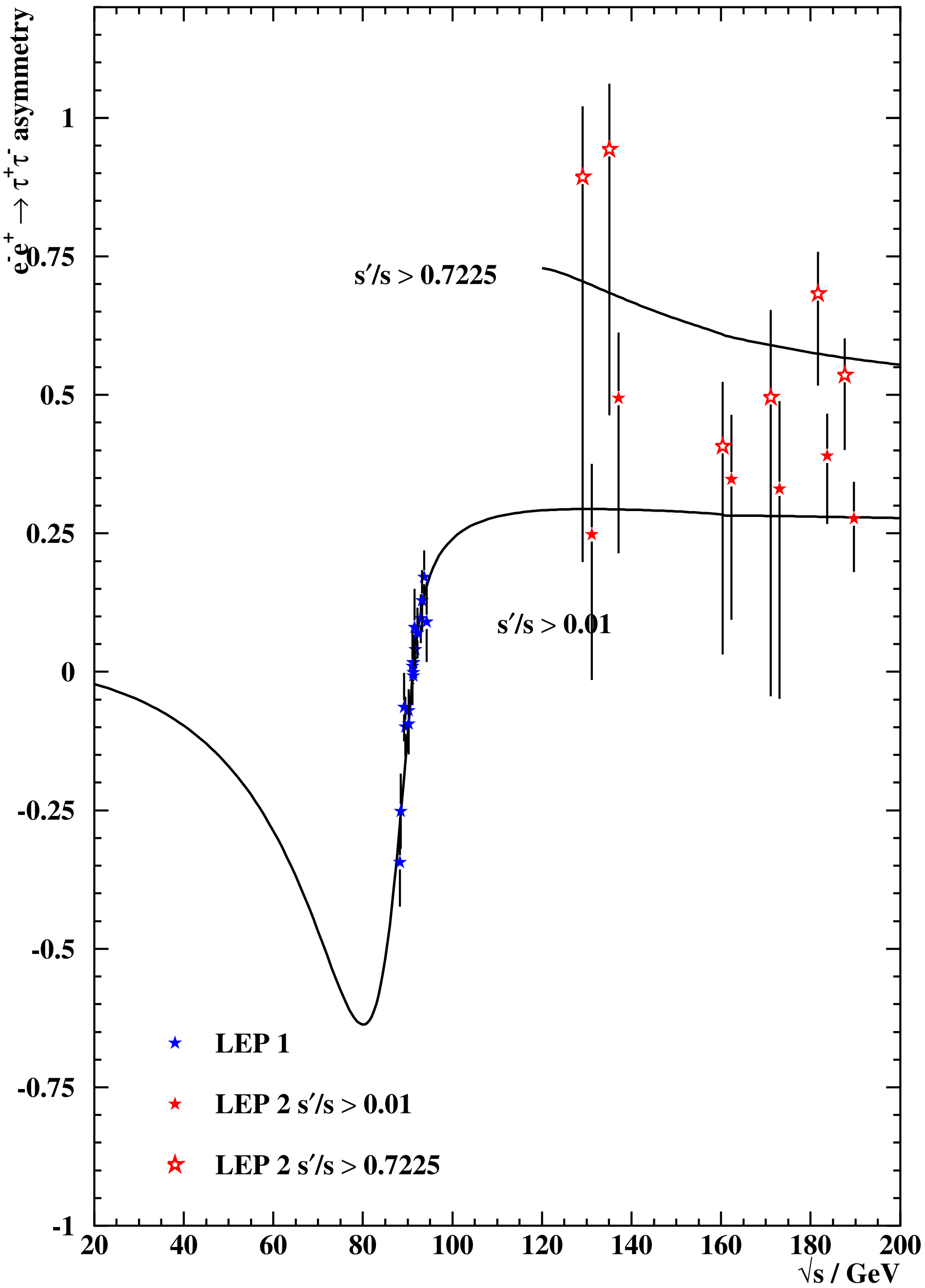

Figure 6.12: The measured asymmetry for $e^+e^- \rightarrow \tau^+\tau^-$ as a function of $\sqrt{s}$ showing the results taken at LEP1 [51] and the results obtained in the analyses for $\mathrm{s}'/\mathrm{s} > 0.7225$ and $\mathrm{s}'/\mathrm{s} > 0.01$ selections. The points at each energy have been separated for clarity. The solid lines are the ZFITTER prediction for the Standard Model asymmetry.

Chapter 7

Combining the Muon and Tau Pair Results

7.1 Lepton Pair Asymmetry

If lepton universality is assumed, which is reasonable given the consistency between the cross-section and asymmetry results given in the previous two chapters, the asymmetry measurements for μ and τ pairs can be combined giving an improvement in the error on the asymmetry measurement. The method used to combine the individual asymmetry measurements is shown in figure 7.1 for non-radiative selections using the 189 GeV data.

First the raw angular distribution for the μ pairs 7.1(a) is added to the raw angular distribution for the τ pairs 7.1(b) to give the raw angular distribution for the combined measurement 7.1(c). Next, the initial/final-state radiation correction for the μ pairs 7.1(d) is added to that for the τ pairs 7.1(e) to give the correction for the combined measurement 7.1(f). Likewise, the predicted backgrounds for the μ pairs 7.1(g) is added to that for the τ pairs 7.1(h) to give the background for the combined measurement 7.1(i). In these plots the medium grey histogram is the background from other physics processes and the dark grey is the feedthrough background. Then, the bin-by-bin efficiencies for the μ pairs 7.1(j) and τ pairs 7.1(k) are added, to give the effective efficiency used for the combined measurement 7.1(l).

Finally, the distributions for the combined measurement are treated in the same way as for the individual μ and τ pairs measurements by subtracting the small initial/final-state radiation correction 7.1(f) and background 7.1(i) from the raw distribution 7.1(c), which is then corrected for efficiency 7.1(l).

The corrected angular distribution which is obtained is then used to give an asymmetry with statistical error using the same method described previously.

The measured combined asymmetries, after the correction for initial/final-state radiation interference[1], are given along with the Standard Model prediction in table 7.1 and shown in figure 7.2.

The systematic error on the combined asymmetries is taken as the efficiency weighted sum of the individual systematic errors.

$$\left(\Delta A_{FB}^{combined}(sys)\right)^2 = \left(\frac{\epsilon_\mu}{\epsilon_\mu + \epsilon_\tau}\Delta A_{FB}^{\mu}(sys)\right)^2 + \left(\frac{\epsilon_\tau}{\epsilon_\mu + \epsilon_\tau}\Delta A_{FB}^{\tau}(sys)\right)^2 \tag{7.1}$$

To motivate this systematic error consider the case where $\epsilon_\mu \gg \epsilon_\tau$. Then, as required, equation 7.1 reduces to:

$$\Delta A_{FB}^{combined}(sys) = \Delta A_{FB}^{\mu}(sys) \tag{7.2}$$

The combined asymmetry is effectively an efficiency weighted average of the individual asymmetries.

$$A_{FB}^{combined} = \frac{\epsilon_\mu}{\epsilon_\mu + \epsilon_\tau}A_{FB}^{\mu} + \frac{\epsilon_\tau}{\epsilon_\mu + \epsilon_\tau}A_{FB}^{\tau} \tag{7.3}$$

Hence, as the μ pair efficiency is higher that that for the τ pairs the combined asymmetry is closer to the μ pair asymmetry, particularly for the $s'/s > 0.01$ measurement.

However, as the asymmetries are measured in a restricted angular range and corrected by a scaling factor, the combined asymmetry given in equation 7.3 is strictly

$$C_{0.95}A_{FB_{0.95}}^{combined} = \frac{\epsilon_\mu}{\epsilon_\mu + \epsilon_\tau}C_{0.95}A_{FB_{0.95}}^{\mu} + \frac{\epsilon_\tau}{\epsilon_\mu + \epsilon_\tau}C_{0.9}A_{FB_{0.9}}^{\tau} \tag{7.4}$$

where C_X is the scaling factor to correct the asymmetry A_{FB_X} measured in the angular range $|\cos\theta| < X$. So,

$$A_{FB_{0.95}}^{combined} = \frac{\epsilon_\mu}{\epsilon_\mu + \epsilon_\tau}A_{FB_{0.95}}^{\mu} + \frac{\epsilon_\tau}{\epsilon_\mu + \epsilon_\tau}\frac{C_{0.9}}{C_{0.95}}A_{FB_{0.9}}^{\tau} \tag{7.5}$$

where $\frac{C_{0.9}}{C_{0.95}} > 1$ from table 5.5. Because of this the combined measurement can be larger than the individual μ and τ pair measurements.

[1]The size of this small correction for the 172 GeV data is given in table 4.2.

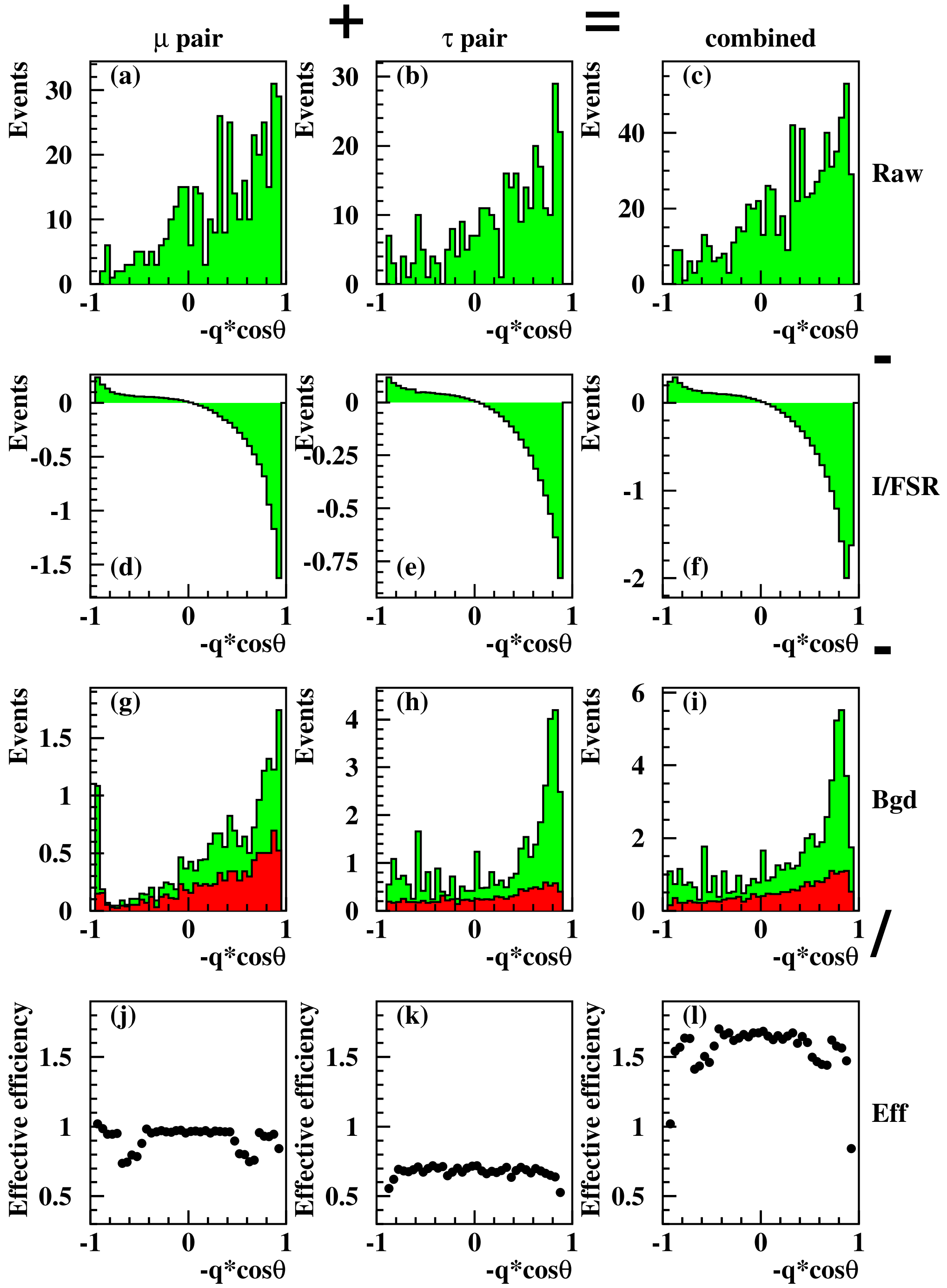

Figure 7.1: The process used to give the combined $e^+e^- \to \mu^+\mu^-$ and $e^+e^- \to \tau^+\tau^-$ angular distribution for the 189 GeV measurement.

	$\sqrt{s}$ GeV	A_{FB}	A_{FB}^{SM}
$s'/s > 0.01$	130.12	$0.27\ ^{+0.11}_{-0.30} \pm 0.01$	0.29
	136.07	$0.30\ ^{+0.07}_{-0.22} \pm 0.00$	0.29
	161.34	$0.23\ ^{+0.09}_{-0.23} \pm 0.00$	0.28
	172.08	$0.16\ ^{+0.11}_{-0.30} \pm 0.01$	0.28
	182.68	$0.31\ ^{+0.05}_{-0.09} \pm 0.01$	0.28
	188.66	$0.29\ ^{+0.04}_{-0.08} \pm 0.01$	0.28
$s'/s > 0.7225$	130.12	$0.56\ ^{+0.08}_{-0.16} \pm 0.02$	0.70
	136.07	$0.79\ ^{+0.08}_{-0.14} \pm 0.02$	0.68
	161.34	$0.48\ ^{+0.08}_{-0.16} \pm 0.02$	0.61
	172.08	$0.47\ ^{+0.10}_{-0.20} \pm 0.02$	0.59
	182.68	$0.60\ ^{+0.05}_{-0.07} \pm 0.02$	0.57
	188.66	$0.53\ ^{+0.04}_{-0.06} \pm 0.02$	0.57

Table 7.1: The combined μ and τ pair asymmetries at each energy after correcting for small effect due to initial/final- state radiation interference. The first error is statistical and the second systematic. The systematic error for the 136 GeV $s'/s > 0.01$ asymmetry is too small to the quoted precision.

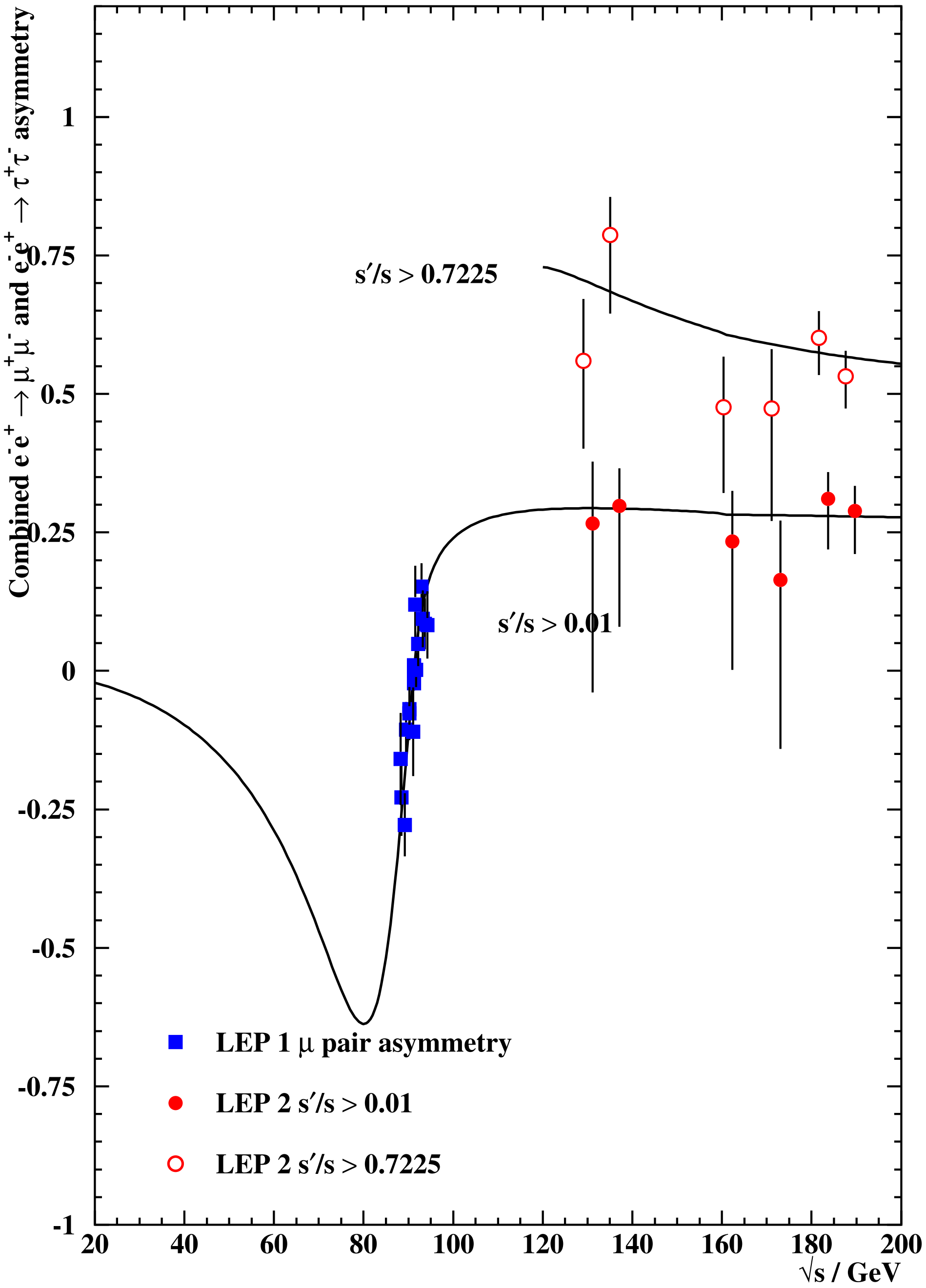

Figure 7.2: The combined $e^+e^- \rightarrow \mu^+\mu^-$ and $e^+e^- \rightarrow \tau^+\tau^-$ asymmetry as a function of $\sqrt{s}$ for $s'/s > 0.7225$ and $s'/s > 0.01$ selections. The dominant error is statistical. Also shown is the ZFITTER prediction for the Standard Model cross-section and the asymmetries of the μ pairs measured at LEP1 [51].

7.2 Running of α_{em}

At centre-of-mass energies above the Z^0 the amplitude of the s-channel photon exchange becomes comparable to, or in the case of lepton pair production larger than, that for Z exchange. This means that the LEP2 cross-section and asymmetry results allow the possibility of studying the photon propagator.

The running of α_{em} has been studied by measuring the value of α_{em} at the five LEP2 data taking energies[2]. This measurement was performed by varying α_{em} to minimise the χ^2 between the cross-section and asymmetry measurements and the full Standard Model predictions, including the photon and Z^0 exchange, for these quantities, calculated using ZFITTER. All other Standard Model parameters are fixed. A further fit which uses the measurements at all energies together was also performed, and the fitted value of α_{em} is scaled to the luminosity weighted centre-of-mass energy, for all data, of 177.59 GeV.

The cross-section for the μ and τ pair final states, $\sigma_{\mu^+\mu^-}$ and $\sigma_{\tau^+\tau^-}$ and the combined μ and τ asymmetry measurements, A^l_{FB}, given in this thesis are used in this fit. In addition the hadronic cross-sections, σ_{had}, given in [42, 43, 44]; and the ratio, R_b, of the $b\bar{b}$ cross-section to the hadronic cross-section[3]; the b and c quark asymmetries, A^b_{FB} and A^c_{FB} given in [56] are also used as inputs to the fits[4]. Only the non-radiative measurements are used so that the amplitude of the photon propagator is as large a fraction of the total exchange amplitude as possible. The correlations between the errors of these measurements at each energy point and between the energies were calculated and taken into account in the fits.

This is done by calculating an error correlation matrix using the method described below. If the error on two measurements, Δ_1 and Δ_2, are entirely independent the total error, Δ_T, is obviously $(\Delta_T)^2 = (\Delta_1)^2 + (\Delta_2)^2$. Likewise if the errors are entirely correlated the total error is $(\Delta_T)^2 = (\Delta_1 + \Delta_2)^2$. Both of these cases

[2] The 130 and 136 GeV data have been combined to increase the statistics

[3] $R_b = \frac{\sigma(b\bar{b})}{\sigma(q\bar{q})}$

[4] The R_b, A^b_{FB} and A^c_{FB} measurement are not yet available for the 189 GeV data and so are not included.

can be calculated using a correlation matrix:

$$(\Delta_T)^2 = \begin{pmatrix} \Delta_1 & \Delta_2 \end{pmatrix} \begin{pmatrix} C_{11} & C_{12} \\ C_{21} & C_{22} \end{pmatrix} \begin{pmatrix} \Delta_1 \\ \Delta_2 \end{pmatrix}$$

where C_{ij} is the fraction of correlated error between Δ_i and Δ_j, ie.

$$C_{ij} = \frac{\Delta_i^{correlated}}{\Delta_i} \frac{\Delta_j^{correlated}}{\Delta_j}$$

Clearly in the two cases mentioned above $C_{11} = 1$ and $C_{22} = 1$. In the case of completely independent errors $C_{12} = C_{21} = 0$, and in the case of entirely correlated errors $C_{12} = C_{21} = 1$.

For measurements at the same energy point, the correlations arise from the common uncertainty due to the statistical and systematic errors on the luminosity and from the initial-/final-state radiation interference correction. For the same measurement at different energies, the correlated errors are those from the systematic error on the luminosity, the initial-/final-state radiation correction, the uncertainties due to the efficiency and background corrections. Correlations in the errors between different measurements at different energies arise from the systematic error on the luminosity and the initial-/final-state radiation correction.

The results of the fit, along with the Standard Model prediction for the of α_{em} are given in table 7.2 and shown in figure 7.3. The results of the fits are all consistent with the Standard Model predictions and are all more than one standard deviation below the low energy limit α_{em}^{-1}(0 GeV)= $137.0359979 \pm 0.0000032$ [1]. The results of the combined fit is nearly 3 standard deviations below α_{em}^{-1}(0 GeV) demonstrating the running of α_{em} with energy.

7.3 Beam Energy Measurement

The uncertainty in the energies of the e^+e^- beams is one of the systematic errors on any measurement and ideally it should be as small as possible. At LEP2 this uncertainty is typically $< 0.04\%$ of the total energy. A possible method to improve this uncertainty is to use the information from the fermion-pair events which have radiatively returned to the Z^0 peak. The width and mass of the Z^0 peak are precisely

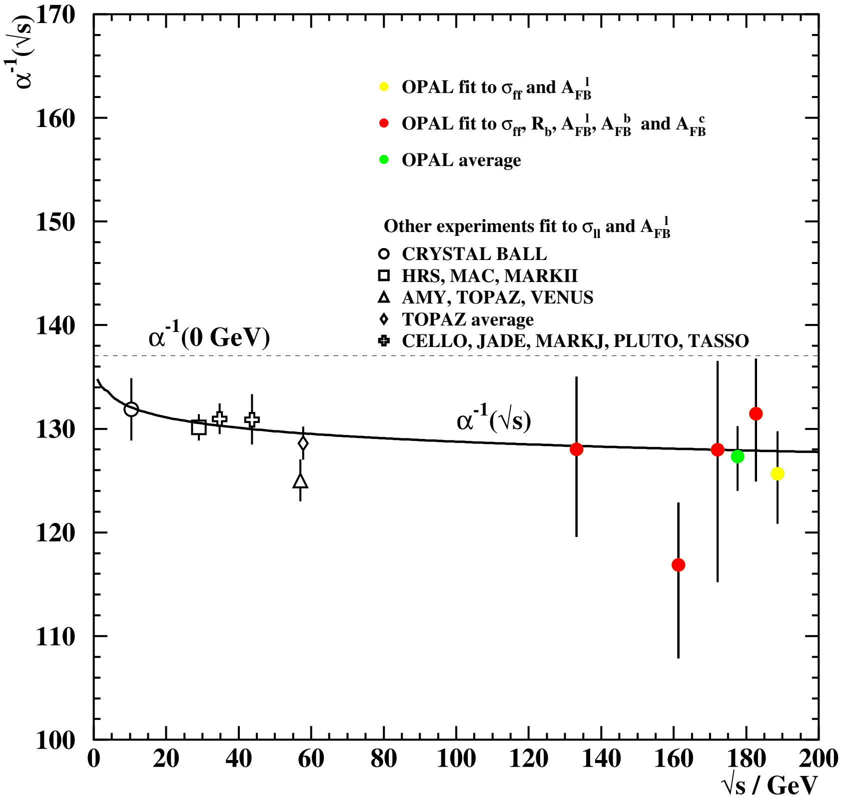

Figure 7.3: The results of the fit to α_{em} for all energies. The points represent the measurements, the solid line is the Standard Model Prediction and the dashed line is the value of $\alpha_{em}^{-1}(0)$.

The dark grey points are the results of the fits to σ_{had}, $\sigma_{\mu\mu}$, $\sigma_{\tau\tau}$, R_b, A_{FB}^l, A_{FB}^b and A_{FB}^c for 133, 161, 172 and 184 GeV. The very light grey point is the result of the fit at 189 GeV which only fits to σ_{had}, $\sigma_{\mu\mu}$, $\sigma_{\tau\tau}$ and A_{FB}^l, as the A_{FB}^b and A_{FB}^c results are unavailable at this energy. The medium grey point is the results of the combined fit to all energies. The open points are the measurement from other e^+e^- experiments as given in [43].

$\sqrt{s}$ (GeV)	Fit		Standard Model
	α_{em}^{-1}	$\chi^2/d.o.f$	α_{em}^{-1}
133.19	$128.2^{+8.5}_{-7.0}$	4.4/7	128.3
161.34	$116.9^{+9.0}_{-6.0}$	5.4/7	128.1
172.08	$128.0^{+12.7}_{-8.6}$	2.8/7	128.0
182.68	$131.5^{+6.5}_{-5.3}$	2.7/7	127.9
188.66	$125.7^{+4.9}_{-4.1}$	0.7/4	127.8
177.59	$127.3^{+3.3}_{-2.9}$	17.7/32	127.9

Table 7.2: The results to the fits to α_{em} showing the luminosity weighted centre-of-mass energy, the result of the fit, the χ^2 per degree of freedom and the Standard Model prediction for the value of α_{em}. The first 5 rows are the fits to the individual energies, the final row is the combined fit to all energies.

known from the LEP1 analyses [1]. By comparing the mass of the Z^0 to the mass of the radiative return peak in the LEP2 data, the actual $\sqrt{s}$ energy of the LEP2 data can be deduced, with the uncertainty on the measured mass becoming the uncertainty on the $\sqrt{s}$ energy.

The low statistics of the LEP2 data set, arising from the 160 pb^{-1} of data currently available, is too small to yield a very precise energy measurement using this method at the moment. However, it is hoped that the final data set will contain over 500 pb^{-1} of data, and by combining this method with equivalent analyses from the other LEP experiments and with a similar analysis using the multihadronic data, it will give another independent method of determining the beam energy, and so will allow a reduction in the overall error on the energies of the e^+e^- beams.

This section describes a preliminary investigation into the feasibility of determining the beam energy using the μ and τ pair events and gives an estimate of the expected size of the uncertainty on the beam energy which could be obtained at the end of the LEP2 running when combined with the similar analyses from the other LEP experiments.

7.3.1 Check of the measurement using Monte Carlo information

The validity of the measurement is tested using the 184 GeV μ pair Monte Carlo sample. Figure 7.4 shows the generated distribution of $\sqrt{s'}$ for events near the Z^0 peak in the region $79<\sqrt{s'}<103$ GeV. The points represent the number of Monte Carlo events in each $\sqrt{s'}$ bin. The solid line shows the result of a χ^2 fit of an asymmetric Breit-Wigner function, $F(\sqrt{s'})$, shown in equation 7.6, which is used to parameterise the shape of the Z^0 peak.

$$F(\sqrt{s'}) = \begin{cases} N\frac{2\sqrt{s'}}{s-s'}\frac{s'\Gamma_L^2}{(s'-M_Z^{*2})^2+s'\Gamma_L^2} & \text{if } \sqrt{s'} < M_z^* \\ N\frac{2\sqrt{s'}}{s-s'}\frac{s'\Gamma_R^2}{(s'-M_Z^{*2})^2+s'\Gamma_R^2} & \text{if } \sqrt{s'} > M_z^* \end{cases} \tag{7.6}$$

where

- N is a normalisation factor
- $\frac{2\sqrt{s'}}{s-s'}$ is a factor of the form $\frac{1}{E_\gamma}$ taking into account the probability of radiating a photon of energy E_γ.
- $\frac{s'}{(s'-M_Z^{*2})^2+s'\Gamma^2}$ is a relativistic Breit-Wigner formula which fits the data best when different widths are used on the two sides.
- $\Gamma_{L,R}$ ensure the function is continuous at $\sqrt{s'} = M_Z^*$.

The fitted range $84< \sqrt{s'} <98$ GeV is indicated by the dotted lines. As can be seen from figure 7.4 outside this region the function becomes progressively worse at describing the shape. Different widths were used on each side of the distribution as this was found to give the smallest χ^2 and to give a fitted value of the mass of the Z^0, M_Z^*, closer to the value of $M_Z = 91.187$ GeV used in the Monte Carlo generation.

In the fit N, M_Z^*, Γ_L and Γ_R are allowed to vary freely and s is set to the generated value (eg. $(184 \text{ GeV})^2$).

The fitted value of M_Z^* is 91.160 ± 0.015 GeV, where the error is statistical. This can be used to deduce the actual collision energy, $\sqrt{s^*}$, using

$$\frac{M_Z}{\sqrt{s}} = \frac{M_Z^*}{\sqrt{s^*}} \tag{7.7}$$

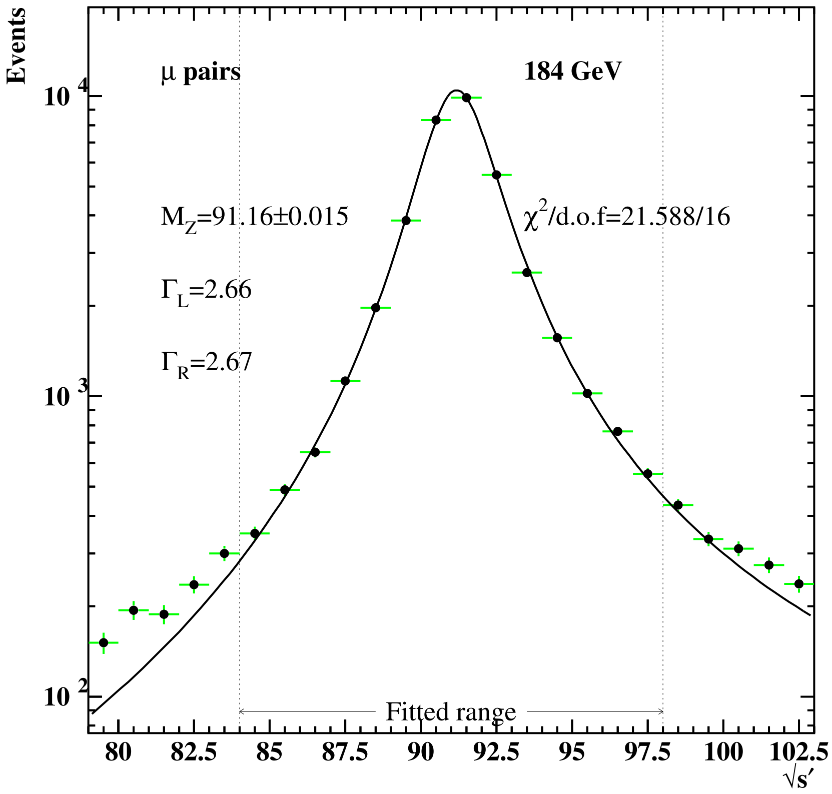

Figure 7.4: The generated $\sqrt{s'}$ distribution in the range $79<\sqrt{s'}<103$ GeV for all 184 GeV μ pair Monte Carlo events. The solid line is the result of the χ^2 fit of the Breit-Wigner function, the dotted line shows the fitted range. The fitted values of the free parameters M_z^*, Γ_L and Γ_R are shown together with the χ^2 per degree of freedom for the fit.

where $\sqrt{s}$ is the actual nominal collision energy. This procedure gives $\sqrt{s^*} = 183.95 \pm 0.03$ GeV, which is consistent with the generated value of 184 GeV.

Table 7.3 shows the fitted values of mass and collision energy for all μ and τ pair Monte Carlo samples. As these fits use the generated Monte Carlo $\sqrt{s'}$ distribution any deviation between the measured and generated collision energy is independent of the detector and measures the bias in the measurement. The KORALZ generator is used for both the μ and τ pair Monte Carlo samples at all energies. The poor χ^2 in the fits is due to the arbitrary function which has been used in the fit.

	$\sqrt{s}$ GeV	M_Z^* GeV	$\chi^2/d.o.f$	$\sqrt{s^*}$ GeV
$\mu^+\mu^-$	130	91.093 ± 0.035	20.5 / 16	129.87 ± 0.05
	136	91.023 ± 0.036	18.1 / 16	135.76 ± 0.05
	161	91.014 ± 0.020	38.4 / 16	160.69 ± 0.04
	171	91.041 ± 0.018	44.9 / 16	170.73 ± 0.03
	184	91.160 ± 0.015	21.6 / 16	183.95 ± 0.03
	189	91.160 ± 0.018	33.4 / 16	188.94 ± 0.04
$\tau^+\tau^-$	130	91.097 ± 0.034	28.8 / 16	129.87 ± 0.05
	136	91.085 ± 0.035	11.4 / 16	135.85 ± 0.05
	161	91.101 ± 0.017	35.4 / 16	160.85 ± 0.03
	171	91.085 ± 0.017	27.1 / 16	170.81 ± 0.03
	184	91.159 ± 0.016	21.9 / 16	183.94 ± 0.03
	189	91.151 ± 0.017	25.1 / 16	188.93 ± 0.04

Table 7.3: The measured value of $\sqrt{s^*}$ using generated $\sqrt{s'}$ from all events for all μ and τ pair Monte Carlo samples. Shown is the $\sqrt{s}$ used to generate the Monte Carlo, the fitted value of M_Z^*, the χ^2 per degree of freedom and the measured $\sqrt{s^*}$. The errors are statistical.

7.3.2 Correction due to reconstructed $\sqrt{s'}$ calculation and selection efficiency

The reasonable agreement between the generated and extracted $\sqrt{s}$ of the Monte Carlo samples demonstrated in the previous section indicates that this method of determining the beam energy from the data is feasible. However, corrections are also needed to allow for the detector effects in the calculation of the $\sqrt{s'}$ and the efficiency of the selection.

To determine the size of these corrections, the χ^2 fit is repeated using the reconstructed $\sqrt{s'}$ of the selected μ and τ pair events from the Monte Carlo samples. As before N, M_Z^*, Γ_L and Γ_R are allowed to vary. Figure 7.5(a) shows the distribution of the reconstructed $\sqrt{s'}$ for the selected events from the 184 GeV μ pair Monte Carlo sample, and figure 7.5(b) shows the distribution for the 184 GeV τ pair Monte Carlo sample. This distribution is broader, due to the effect of the reconstruction of the event and the calculation of the $\sqrt{s'}$, and has a peak at a slightly lower mass than the Z^0 mass. The dotted lines indicate the region over which the χ^2 fit is performed and the solid line is the result of the fit. The parameterisation gives a poorer fit to the reconstructed distribution than to the generated distribution, but is still able to produce a reasonable value for the mass. The fit to the τ data is better due to detector resolution effects.

The results of the fits to each energy for all μ and τ pair Monte Carlo samples at the detector level are given in table 7.4. The discrepancy between the generated and measured $\sqrt{s}$ at each energy are consistent with a statistical scatter about a single discrepancy caused by the event selection. Hence, the average discrepancies between the measured and actual $\sqrt{s}$ are used to correct the results of the data measurements. For the μ pairs this correction is $+0.15 \pm 0.03$ GeV. For the τ pairs the correction is -0.004 ± 0.075 GeV.

7.3.3 LEP beam energy measurement

By performing a χ^2 fit to the reconstructed $\sqrt{s'}$ distribution of the selected data events the LEP beam energy can now be determined. However, as the statistics are

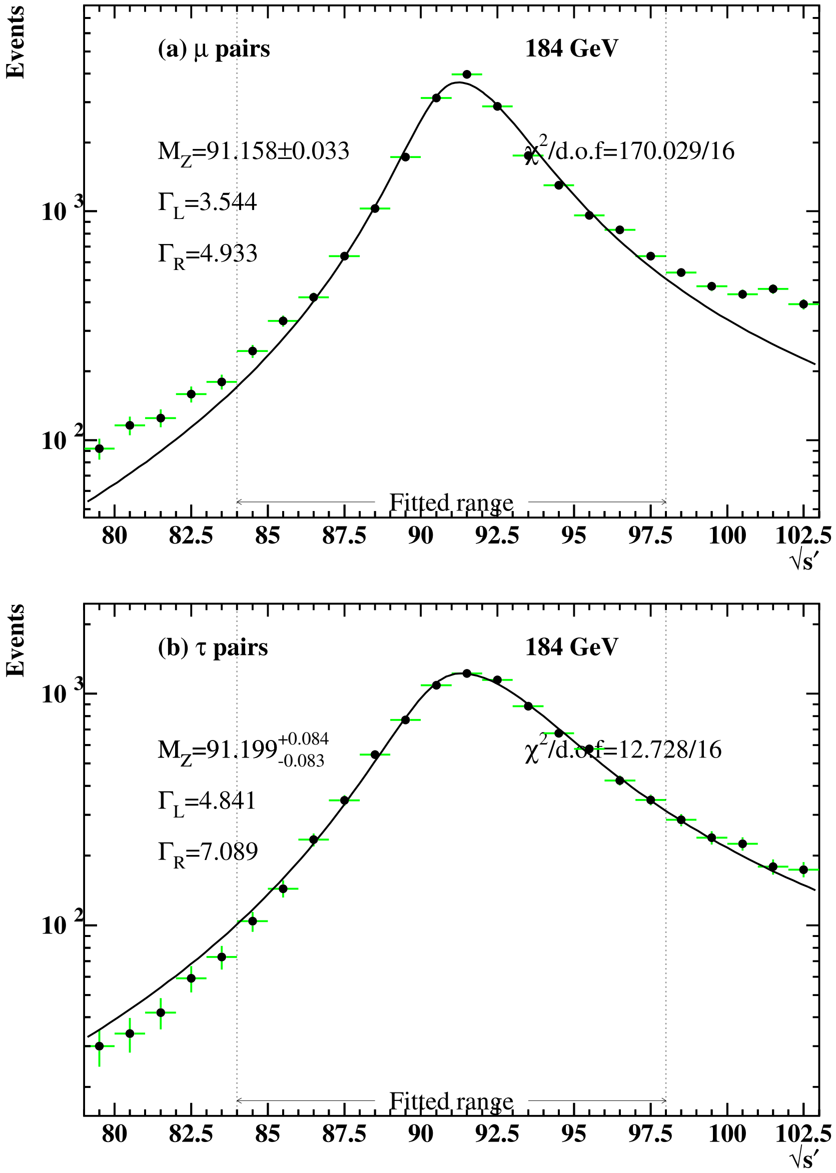

Figure 7.5: The reconstructed $\sqrt{s'}$ distribution in the range $79 < \sqrt{s'} < 103$ GeV for selected

a) 184 GeV μ pair Monte Carlo events.

b) 184 GeV τ pair Monte Carlo events.

The solid line is the result of the χ^2 fit of the Breit-Wigner function, the dotted line shows the fitted range. The fitted values of the free parameters M_z^*, Γ_L^2 and Γ_R^2 are shown together with the χ^2 per degree of freedom for the fit.

	$\sqrt{s}$ GeV	M_Z^* GeV	$\chi^2/d.o.f$	$\sqrt{s^*}$ GeV
$\mu^+\mu^-$	130	91.104 ± 0.062	41.1 / 16	129.88 ± 0.09
	136	91.075 ± 0.067	39.3 / 16	135.83 ± 0.10
	161	91.081 ± 0.037	143.5 / 16	160.81 ± 0.07
	171	91.103 ± 0.033	153.6 / 16	170.84 ± 0.06
	184	91.158 ± 0.033	170.0 / 16	183.94 ± 0.07
	189	91.097 ± 0.036	132.1 / 16	188.81 ± 0.07
$\tau^+\tau^-$	130	91.286 ± 0.133	16.1 / 16	130.14 ± 0.19
	136	91.256 ± 0.152	10.9 / 16	136.10 ± 0.23
	161	91.066 ± 0.075	4.6 / 16	160.79 ± 0.13
	171	91.209 ± 0.080	16.3 / 16	171.04 ± 0.15
	184	91.199 ± 0.084	12.7 / 16	184.02 ± 0.17
	189	91.244 ± 0.106	18.5 / 16	189.12 ± 0.22

Table 7.4: The measured value of $\sqrt{s^*}$ using the reconstructed $\sqrt{s'}$ from selected events in all μ and τ pair Monte Carlo samples. Shown is the $\sqrt{s}$ used to generate the Monte Carlo, the fitted value of M_Z^*, the χ^2 per degree of freedom and the measured $\sqrt{s^*}$. The errors are statistical.

very limited some extra assumptions must be made. First the $\sqrt{s'}$ distribution was corrected for the background from other physics processes by subtracting the Monte Carlo predicted number of background events in each $\sqrt{s'}$ bin. The Breit-Wigner function was then fitted to the data events for the range 84< $\sqrt{s'}$ <98 GeV. In these fits the Monte Carlo is assumed to model the data accurately, so the widths, Γ_L and Γ_R, are taken to be those obtained from the fit to the reconstructed $\sqrt{s'}$ of the selected Monte Carlo events at the equivalent energy. Only N and M_Z^*, which are independent of the Monte Carlo, are allowed to vary. Due to the low statistics in each $\sqrt{s'}$ bin the error on the number of events is calculated using Poissonian statistics.

Figures 7.6 and 7.7 show the reconstructed $\sqrt{s'}$ distributions for the selected μ and τ pair events in the region 79< $\sqrt{s'}$ <103 GeV for the data taken at each energy. In these plots the points are the number of data events which are selected in each $\sqrt{s'}$ bin and the error bars show the Poissonian error on this number. The solid line shows the shape of the Breit-Wigner function which was fitted to the data and the dotted line shows the region over which the fit was performed. Also given are the fitted Z^0 mass, M_Z^*, the χ^2 per degree of freedom for the fit and widths of the peak which are taken from the fit to the Monte Carlo.

As the selection efficiency of the radiative events is greater for μ pair events than τ pair events, the statistically dominated error is always smaller for the fit to the μ pair distribution.

The results of the fit together with the statistical error, the χ^2 per degree of freedom, the measured value of the nominal collision energy, $\sqrt{s^*}_{meas}$, and the corrected value, $\sqrt{s^*}_{corr}$ with the statistical and systematic error are given in table 7.5. The systematic error is determined by comparing the measured value of $\sqrt{s^*}_{meas}$, to those obtained when the fit is repeated for the $\sqrt{s'}$ ranges 80< $\sqrt{s'}$ <102 GeV and 81< $\sqrt{s'}$ <101 GeV.

The typical systematic error is around 100 MeV; however that determined for the fit to the 172 GeV τ pair events is significantly larger than this due to the small number of events selected for this fit. As such, this systematic error will be statistically limited and so is unrealistic. In all cases the statistical error dominates

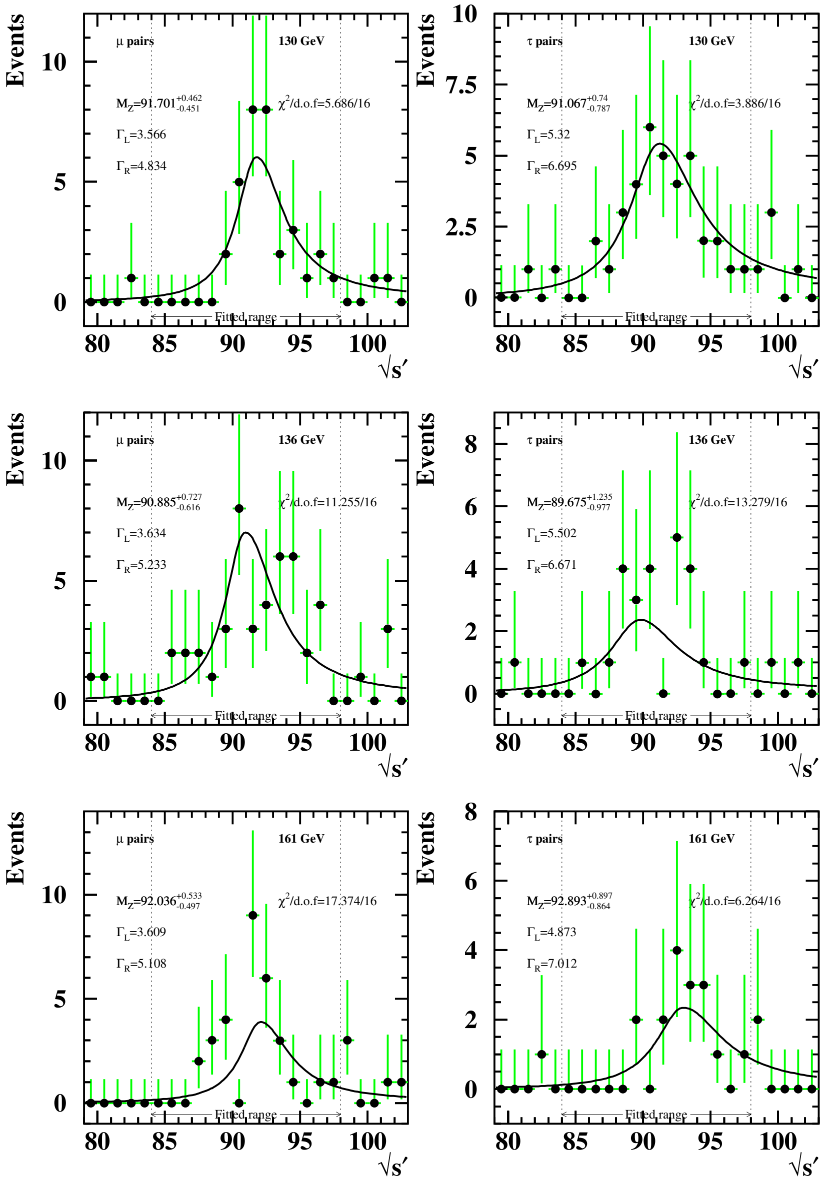

Figure 7.6: The reconstructed $\sqrt{s'}$ in the region $79 < \sqrt{s'} < 103$ GeV for selected μ and τ pair events using the 130, 136 and 161 GeV data. The solid line is the result of the χ^2 fit of a Breit-Wigner function to the region $84 < \sqrt{s'} < 98$ GeV, indicated by the dotted lines. The fitted values of the fit parameters M_z^*, Γ_L and Γ_R are shown together with the χ^2 per degree of freedom for the fit.

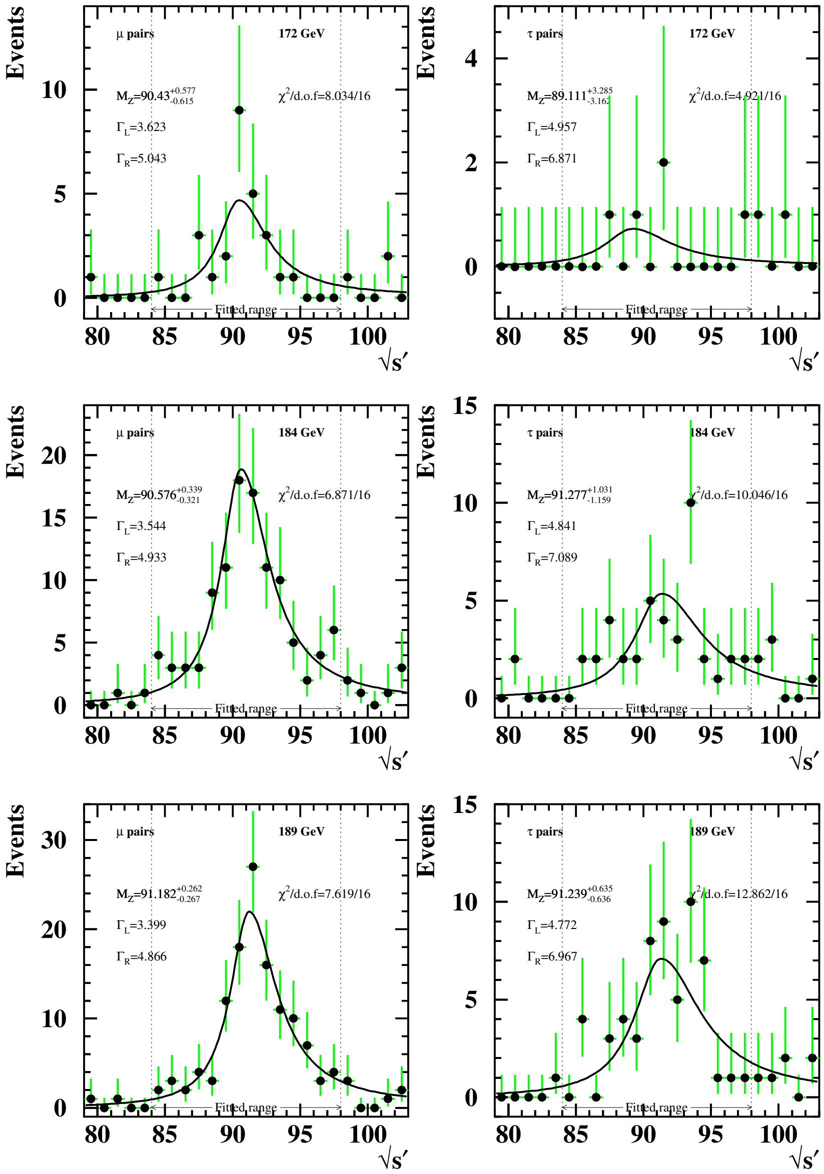

Figure 7.7: The reconstructed $\sqrt{s'}$ in the region $79 < \sqrt{s'} < 103$ GeV for selected μ and τ pair events using the 172, 184 and 189 GeV data. The solid line is the result of the χ^2 fit of a Breit-Wigner function to the region $84 < \sqrt{s'} < 98$ GeV, indicated by the dotted lines. The fitted values of the fit parameters M_z^*, Γ_L and Γ_R are shown together with the χ^2 per degree of freedom for the fit.

the total uncertainty.

	$\sqrt{s}$ GeV	M_Z^* GeV	$\chi^2/d.o.f$	$\sqrt{s^*}_{meas}$ GeV	$\sqrt{s^*}_{corr}$ GeV
$\mu^+\mu^-$	130.12	$91.701^{+0.462}_{-0.451}$	5.7 / 16	130.73	$130.88^{+0.66}_{-0.64} \pm 0.03$
	136.07	$90.885^{+0.727}_{-0.616}$	11.3 / 16	135.55	$135.70^{+1.08}_{-0.92} \pm 0.09$
	161.34	$92.036^{+0.533}_{-0.497}$	17.4 / 16	162.50	$162.64^{+0.94}_{-0.88} \pm 0.03$
	172.08	$90.430^{+0.577}_{-0.615}$	8.0 / 16	170.57	$170.72^{+1.09}_{-1.16} \pm 0.05$
	182.68	$90.576^{+0.339}_{-0.321}$	6.9 / 16	181.77	$181.92^{+0.68}_{-0.64} \pm 0.08$
	188.66	$91.182^{+0.262}_{-0.267}$	7.6 / 16	188.99	$189.14^{+0.54}_{-0.55} \pm 0.10$
$\tau^+\tau^-$	130.12	$91.067^{+0.740}_{-0.787}$	3.9 / 16	129.83	$129.79^{+1.05}_{-1.12} \pm 0.22$
	136.07	$89.675^{+1.235}_{-0.977}$	13.3 / 16	133.74	$133.71^{+1.84}_{-1.46} \pm 0.09$
	161.34	$92.893^{+0.897}_{-0.864}$	6.3 / 16	164.01	$163.98^{+1.58}_{-1.53} \pm 0.06$
	172.08	$89.111^{+3.285}_{-3.162}$	4.9 / 16	168.08	$168.05^{+6.20}_{-5.96} \pm 0.68$
	182.68	$91.277^{+1.031}_{-1.159}$	10.0 / 16	183.18	$183.15^{+2.07}_{-2.33} \pm 0.31$
	188.66	$91.239^{+0.635}_{-0.636}$	12.9 / 16	189.11	$189.07 \pm 1.32 \pm 0.08$

Table 7.5: The measured value of $\sqrt{s^*}$ using the reconstructed $\sqrt{s'}$ from selected data events for all μ and τ pairs. Shown is the $\sqrt{s}$ of the data, the fitted value of M_Z^*, the χ^2 per degree of freedom and the measured $\sqrt{s^*}$ and the corrected $\sqrt{s^*}$. The first errors are statistical and, where given, the second is the systematic error.

Assuming lepton universality, a weighted averaging of the μ and τ pair results is performed using the statistical error only. The resulting averages and statistical errors for each energy are given in table 7.6.

To estimate the likely statistical error that could be achieved with the full LEP2 data sets, consisting of an integrated data luminosity of 500 pb^{-1} per LEP experiment, the statistical error of ± 0.22 GeV from the 160 pb^{-1} currently recorded by the OPAL experiment is reduced by a factor of approximately 3.5 to ± 0.089 GeV. Hence at the end of the LEP2 data taking this analysis could provide a measurement of the LEP beam energy with a statistical error of approximately 45 MeV per beam and an estimated, systematic error of around 50 MeV per beam. A fuller study of the systematic errors may be able to reduce the size of this uncertainty.

$\sqrt{\mathrm{s}}$ GeV	$\sqrt{s^*}_{corr}$ GeV
130.12	130.58 ± 0.55
136.07	135.30 ± 0.82
161.34	163.01 ± 0.80
172.08	170.63 ± 1.14
182.68	182.02 ± 0.65
188.66	189.13 ± 0.51

Table 7.6: The weighted average of the measured $\sqrt{s^*}$ for the data from μ and τ pair events. The error is statistical.

7.4 Summary

Between November 1995 and July 1998, LEP delivered an integrated data luminosity of approximately 160 pb^{-1} at centre-of-mass collision energies between 130 and 189 GeV. The data have been studied to measure the μ and τ pair production cross-sections, angular distributions and asymmetries using the OPAL detector. The uncertainty on the asymmetry has been improved by assuming lepton universality and combining the individual μ and τ pair asymmetries. These measurements, along with similar measurements by the other three LEP experiments, are consistent with the Standard Model predictions.

The data have also been combined with measurements of the multihadron and $b\bar{b}$ production cross-sections and b and c quark asymmetries and fitted to the Standard Model prediction to measure the value of the electromagnetic coupling constant, α_{em}, at each energy. A combined fit to the measurements at all energies was also performed and the fitted value, $\alpha_{em}^{-1}(\sqrt{\mathrm{s}}=178\ \mathrm{GeV})=127.3^{+3.3}_{-2.9}$, was consistent with the Standard Model prediction. The value was nearly 3 standard deviations below the low energy limit, $\alpha_{em}^{-1}(\sqrt{\mathrm{s}}=0\ \mathrm{GeV})=137.0$, demonstrating the energy dependence of the electromagnetic coupling constant.

Finally, in a preliminary study, the $\sqrt{\mathrm{s}'}$ distributions of the selected μ and τ pair events, which had undergone a radiative return to the Z^0 peak, were fitted with an asymmetric Breit-Wigner function to measure the fitted mass of the Z^0, M_Z^*. This value was compared to the precisely known value for the actual mass to extract the actual centre-of-mass collision energy, $\sqrt{\mathrm{s}}$, and hence the LEP beam energy. This study showed that, if similar measurements for both reactions using the full LEP2 data set of each experiment are combined, the statistical error on the LEP beam energy could be reduced to approximately 45 MeV.

In conclusion, the measurements presented in this thesis, for the reactions $e^+e^- \to \mu^+\mu^-$ and $e^+e^- \to \tau^+\tau^-$ at centre-of-mass collision energies between 130 and 189 GeV, show no deviation from the Standard Model.

Appendix A

Matrices and Groups

A.1 Matrices

The transpose, $\widetilde{M}$, of an $m \times n$ matrix, M, is an $n \times m$ matrix with elements $(\widetilde{M})_{ji} = M_{ij}$. The complex conjugate, M^*, of an $m \times n$ matrix, M, is an $m \times n$ matrix with elements which are the complex conjugate of those in M.

A matrix is unitary if $M^\dagger = M^{-1}$, where $M^\dagger = \widetilde{M^*}$ and M^{-1} is the inverse of M.

A.2 Groups

A group, $\mathbf{G}$ is a set of elements, T_i, such that:

- The group is closed.
  This means there is an operation, called multiplication, which associates every pair of elements of the group with another element in the group. So, if T_1 and T_2 are elements of $\mathbf{G}$, then $T_3 = T_1 T_2$ is also an element of $\mathbf{G}$.

- The group is associative.
  This means $(T_1 T_2) T_3 = T_1 (T_2 T_3)$ where the multiplication is brackets is evaluated first.

- The group has an identity element, E, such that $ET = TE = T$.

- Every element has an inverse, T^{-1}, such that $T^{-1}T = TT^{-1} = E$.

The group $\mathrm{U}(N)$, for $N \geq 1$, is the set of $N \times N$ unitary matrices, $\mathbf{u}$, with matrix multiplication and the group multiplication operation.

The group $\mathrm{SU}(N)$, for $N \geq 2$ is the subset of the matrices, $\mathbf{u}$, for which $|\mathbf{u}| = 1$.

Bibliography

[1] *Review of Particle Physics*,
R.M. Barnett et al., Phys. Rev. **D54** (1996) 1

[2] *Evidence for oscillation of atmospheric neutrinos*
The Super-Kamiokande Collab. Phys. Rev. Lett. **81** (1998) 1562

[3] *Lower Bound for the Standard Model Higgs boson mass from combining the results from the four LEP experiments*
ALEPH, DELPHI, L3 and OPAL Collabs. CERN-PPE/**98-046**

[4] *A Combination of Preliminary Electroweak Measurements and Constraints on the Standard Model*
LEP Electroweak Working Group CERN-PPE/**97-154**
Submitted to the 1997 summer conferences.

[5] *A Combination of Preliminary Electroweak Measurements and Constraints on the Standard Model*,
4 LEP experiments : ALEPH, DELPHI, L3 and OPAL, CERN-PPE/**96-183**

[6] *Search for Unstable Heavy and Excited Leptons in* e^+e^- *Collisions at* $\sqrt{\mathrm{s}}$ = *170-172 GeV*
OPAL Collab.,Accepted by Z. Phys. C.

[7] *The design, construction and commissioning of the CERN Large Electron Positron collider*,
S. Myers and E. Picasso, Contemp. Phys. **31** (1990) 387

[8] *ALEPH : a detector for electron-positron annihilations at LEP*,
ALEPH Collab.,Nucl. Instrum. Methods **A294** (1990) 127

[9] *The DELPHI detector at LEP*,
DELPHI Collab.,Nucl. Instrum. Methods **A303** (1991) 233

[10] *The construction of the L3 experiment*,
L3 Collab.,Nucl. Instrum. Methods **A289** (1990) 35

[11] *The OPAL detector at LEP*,
OPAL Collab.,Nucl. Instrum. Methods **A305** (1991) 275

[12] P.P. Allport et al., Nucl. Instrum. Methods **A326** (1994) 476

[13] J.R. Carter et al., Nucl. Instrum. Methods **A286** (1990) 99
J.M. Roney et al., Nucl. Instrum. Methods **A279** (1989) 236

[14] R.D. Heuer and A. Wagner, Nucl. Instrum. Methods **A265** (1988) 11
H.M. Fischer et al., Nucl. Instrum. Methods **A252** (1986) 492

[15] H. Mes et al., Nucl. Instrum. Methods **A265** (1988) 445

[16] A. Ji-Gang et al., Nucl. Instrum. Methods **A267** (1988) 386

[17] C. Beard et al., Nucl. Instrum. Methods **A286** (1990) 117

[18] R.M. Brown et al., IEEE Trans. Nucl. Sci **30** (1983) 479
M. Akrawy et al., Nucl. Instrum. Methods **A290** (1990) 76

[19] A.H. Ball et al., IEEE Trans. Nucl. Sci **37** (1990)
G. Artusi et al., Nucl. Instrum. Methods **A279** (1989) 523

[20] G. Bella et al., Nucl. Instrum. Methods **A252** (1986) 503
G. Mikenberg et al., Nucl. Instrum. Methods **A265** (1988) 223

[21] J. Allison et al., Nucl. Instrum. Methods **A236** (1985) 284

[22] G.T.J. Arnison et al., Nucl. Instrum. Methods **A294** (1990) 431

[23] K. Ahmet et al., Nucl. Instrum. Methods **A305** (1991) 275

[24] D.C. Imrie et al., Nucl. Instrum. Methods **A238** (1989) 515

[25] B.E. Anderson et al., IEEE Trans. Nucl. Sci **41** (1994) 845

[26] M. Arignon et al., Nucl. Instrum. Methods **A313** (1992) 103

[27] M. Arignon et al., Nucl. Instrum. Methods **A333** (1993) 330

[28] J. Baines et al., Nucl. Instrum. Methods **A325** (1993) 271

[29] D. Charlton et al., Nucl. Instrum. Methods **A325** (1993) 129

[30] *'ROPE User Guide (version 4.09)'*,
C. Hawkes et al., OPAL Offline Note OFFL-0487 (1995).

[31] *'A GROPE Primer (latest revisions for GR202)'*,
D. Ward and J. Banks, OPAL Offline Note (1995)

[32] J. Allison et al., Nucl. Instrum. Methods **A317** (1992) 47

[33] J. Allison et al., Nucl. Instrum. Methods **A294** (1990) 431

[34] S. Jadach, B.F.L. Ward and Z. Wąs, Comput. Phys. Commun.**79** (1994) 503

[35] J. Fujimoto et al., Comput. Phys. Commun.**100** (1997) 128

[36] J. Hilgart, R.Kleiss, and F. Le Diberder, Comput. Phys. Commun.**75** (1993) 191

[37] ALEPH Collab.,Z. Phys. **C71** (1996) 179.

[38] D. Bardin et al., CERN-TH-6443-92 Phys. Lett. **B255** (1991) 290 Nucl. Phys. **B351** (1991) 1 Z. Phys. **C44** (1989) 493.

[39] F. Halzen and A.D. Martin,
Quarks and Leptons: An Introductory Course in Modern Particle Physics,
John Wiley and Sons, 1984.

[40] *Measurement of Cross-sections and Asymmetries in* e^+e^- *Collisions at 130-140 GeV Centre-of-mass Energy*
OPAL Collab., CERN-PPE/**96-025**, Phys. Lett. **B376** (1996) 232

[41] *Production of Fermion-pair Events in e^+e^- Collisions at 161 GeV Centre-of-mass Energy*
OPAL Collab., CERN-PPE/**96-156**, Phys. Lett. **B391** (1997) 221

[42] *Tests of the Standard Model and Constraints on New Physics from Measurements of Fermion-pair Production at 130-172 GeV at LEP*
OPAL Collab., CERN-PPE/**97-101**, European Physical Journal **C2** (1998) 411

[43] *Tests of the Standard Model and Constraints on New Physics from Measurements of Fermion-pair Production at 183 GeV at LEP*
OPAL Collab., CERN-PPE/**98-108**, Accepted by European Physical Journal C

[44] *Standard Model Measurement in e^+e^- Collisions at $\sqrt{s}$=189 GeV*
OPAL Collab., OPAL Physics Note PN-**360**, Submitted ICHEP conference

[45] T. Sjöstrand, Comput. Phys. Commun.**82** (1994) 74

[46] S. Jadach, W. Placzek, and B.F.L. Ward, University of Tennessee preprint, UTHEP-95-1001.

[47] G. Marchesini et al., Comput. Phys. Commun.**67** (1992) 465

[48] R. Engel and J. Ranft, Phys. Rev. **D54** (1996) 4244

[49] J.A.M. Vermaseren, Nucl. Phys. **B229** (1983) 347

[50] F.A. Berends, R. Pittau and R. Kleiss, Comput. Phys. Commun.**85** (1995) 437

[51] OPAL Collab., Z. Phys. **C61** (1994) 19.
OPAL Collab., Z. Phys. **C58** (1993) 219.
OPAL Collab., Z. Phys. **C52** (1991) 175.

[52] *Measurement of fermion pair production in e^+e^- annihilation and interpretation in terms of new physics phenomena*
ALEPH Collab., Submitted to EPS-HEP97 Cinference
Study of Fermion pair Production in e^+e^- Collisions at 130-183 GeV

ALEPH Collab., Submitted to winter conferences 1998

[53] *Measurement and Interpretation of Fermion-Pair Production at LEP energies from 130 to 172 GeV*
DELPHI Collab., Submitted to 1998 ICHEP conference
Results on Fermion-Pair Production at LEP energies up to 183 GeV
DELPHI Collab., Submitted to 1998 ICHEP conference
Results on Fermion-Pair Production at LEP running near 189 GeV
DELPHI Collab., Submitted to 1998 ICHEP conference

[54] L3 Collab., Phys. Lett. **B370** (1996) 195
L3 Collab., Phys. Lett. **B407** (1997) 361
Preliminary Results from the L3 Experiment at $\sqrt{\mathrm{s}}$*=183 GeV* L3 Collab., Submitted to 1997 EPS-HEP conference
Preliminary Cross Section Measurements from the L3 Experiment at $\sqrt{s} = 189$ *GeV*
L3 Collab., Submitted to 1998 ICHEP conference

[55] OPAL Collab., Phys. Lett. **B389** (1996) 416
OPAL Collab., European Physical Journal **C1** (1998) 425
Measurement of W^+W^- *production cross-section and W-boson branching fractions as* $\sqrt{\mathrm{s}}$*=183 GeV*
Submitted to 1998 ICHEP conference

[56] *Measurements of* R_b*,* A^b_{FB} *and* A^c_{FB} *in* e^+e^- *Collisions at 130-183 GeV with the OPAL Detector at LEP*
OPAL Collab., OPAL Physics Note PN-**348**, Submitted to 1998 ICHEP conference